DOT/FAA/AR-02/102

Office of Aviation Research
Washington, D.C. 20591

Assessment of a Crack Tip Element-Based Approach for Predicting Delamination Growth in Interlayer-Toughened Composite Skin-Stringer Panels

December 2002

Final Report

U.S. Department of Transportation
Federal Aviation Administration

20030319 017

NOTICE

1. Report No. DOT/FAA/AR-02/102	2. Government Accession No.	3. Recipient's Catalog No.
4. Title and Subtitle ASSESSMENT OF A CRACK TIP ELEMENT-BASED APPROACH FOR PREDICTING DELAMINATION GROWTH IN INTERLAYER-TOUGHENED COMPOSITE SKIN-STRINGER PANELS		5. Report Date December 2002
		6. Performing Organization Code
7. Author(s) L.M. Rao and B.D. Davidson		8. Performing Organization Report No.
9. Performing Organization Name and Address Department of Mechanical, Aerospace and Manufacturing Engineering Syracuse University Syracuse, New York 13244		10. Work Unit No. (TRAIS)
		11. Contract or Grant No.
12. Sponsoring Agency Name and Address U.S. Department of Transportation Federal Aviation Administration Office of Aviation Research Washington, DC 20591		13. Type of Report and Period Covered Final Report
		14. Sponsoring Agency Code AIR-120

15. Supplementary Notes

16. Abstract

A crack tip element approach to predict delamination growth is reviewed and then used to predict delamination growth in two stiffened-skin geometries that are typical of aircraft configurations. Predictions by this approach are then compared with experimental results. Test specimens were fabricated from T800H/3900-2, which is a graphite/epoxy material system toughened by a thermoplastic interlayer. Experiments were then performed, and predictions were compared to the observed results. Predictions that incorporated previously generated toughness data gave poor correlation to experiments. It was found that the fracture behavior of those specimens used to determine the toughness versus mode mix data was significantly different than that observed in the stiffened-skin elements. Specifically, the thermoplastic interlayer was relatively thin and dispersed in the interply regions of the skin-stringer elements, and delamination advance occurred through the low toughness base matrix and/or through the base resin/thermoplastic interlayer interface. Through scanning electron microscope observations, two distinct reasons were found to be the cause of lack of thermoplastic layer in the stiffened-skin specimens. The first of these is that the noncritical end of the delamination (i.e., away from the crack tip) terminated at a free surface that was reasonably close to the crack tip. This provided a path through which, during manufacture of the specimens, the toughening material could flow out of the inter-ply region. The second contributing factor was the relative angle of the plies bounding the delamination as compared to the direction of delamination advance. The fibers in these bounding plies compress the thermoplastic interlayer into a sinusoidal grid whose peaks and valleys are not aligned with the direction of crack growth.

17. Key Words Delamination, Fracture, Graphite/epoxy, Mixed-mode, Crack tip element, finite element	18. Distribution Statement This document is available to the public through the National Technical Information Service (NTIS) Springfield, Virginia 22161.		
19. Security Classif. (of this report) Unclassified	20. Security Classif. (of this page) Unclassified	21. No. of Pages 102	22. Price

Form DOT F1700.7 (8-72)   Reproduction of completed page authorized

1/8/2003

TABLE OF CONTENTS

LIST OF FIGURES

LIST OF TABLES

EXECUTIVE SUMMARY

This report is a self-standing addendum to the previously published FAA reports, "A Predictive Methodology for Delamination Growth in Laminated Composites Part I: Theoretical Development and Preliminary Experimental Results, DOT/FAA/AR-97/87, and Part II: Analysis, Applications, Accuracy Assessment and Recommendations, DOT/FAA/AR-01/56. The objective of this addendum is to validate the developed methodology for a material system as used in a complex structural detail that is different than what was investigated and reported in the previous report. This material system contains an interlayer to improve material toughness. As the materials are quite different the mechanism of delamination growth may be quite different from the material system investigated previously. For completeness, a short review of the crack tip element (CTE) methodology used is included.

In this report, the CTE approach is used to predict delamination growth in two different T800H/3900-2 skin-stringer geometries that are typical to aircraft applications. Initially, ERR predictions obtained using CTE analyses were used with experimentally determined toughness data and the nonclassical definition of mode mix to obtain delamination growth predictions. The implementation of the CTE approach required a minor modification to the manner in which it had previously been used, i.e., a different finite element meshing technique was adopted. A substudy is presented to validate this modification, and predictions for the two geometries are obtained from this mesh. Next, the details of the manufacturing and testing of the chosen geometries is described. Experimental results are compared to the predictions. Predictions that incorporated previously generated toughness data gave poor correlation to experiments. It was found that the fracture behavior of those specimens used to determine the toughness versus mode mix data was significantly different than that observed in the stiffened-skin elements. Specifically, the thermoplastic interlayer was relatively thin and dispersed in the interply regions of the skin-stringer elements, and delamination advance occurred through the low toughness base matrix and/or through the base resin/thermoplastic interlayer interface. These results, and those from previous studies, are used to draw conclusions about the applicability of the CTE approach and an overall ERR-based approach for predicting delamination growth in various materials. Recommendations are made for future work as well as for application of the CTE approach to present-day structures.

1. INTRODUCTION.

Delamination is considered to be a critical failure mode in laminated composite structures. Therefore, an accurate method to predict delamination growth is of considerable practical importance. The conventional approach for predicting delamination growth is to compare the analytically or numerically determined strain energy release rate, G, at the appropriate mode mix, to the critical strain energy release rate, G_c, also referred to as the fracture toughness [1-3]. Here, the term mode mix is used to denote the contributions of the mode I (opening mode), mode II (shearing mode), and mode III (tearing mode) loading conditions to the total energy release rate (ERR).

For most practical applications, the time-intensive nature of the conventional approach becomes a primary limitation. It typically requires highly refined two-dimensional (2D) or three-dimensional (3D) finite element (FE) models to determine the ERR, and considerable engineering as well as computational effort is required to develop the models and obtain the solutions [1]. For this reason, this conventional FE modeling approach has been used for predicting delamination growth in laminated composites primarily in research applications. In industry, a structure's resistance to delamination growth is typically assessed through testing. Though it produces delamination-resistant structures, this approach is expensive and typically results in over-designed and, therefore, heavy structural parts.

In order to overcome the problem described above, an alternate delamination growth prediction methodology has been developed. The method uses plate theory and a computationally efficient 2D [1 and 4] or 3D [5 and 6] crack tip element (CTE) analysis, which dramatically reduces the modeling and computational efforts needed to determine energy release rate and mode mixity. Another significant advantage of the CTE analyses is that they allow mode mix to be defined in a nonclassical sense. That is, the conventional approach is based upon classical linear elastic fracture mechanics (LEFM) and assumes that a singular zone exists at the crack tip. Recently however, it has been shown that the classical approach does not provide accurate predictions of delamination growth for several laminated graphite/epoxy composites [3 and 7-11]. In contrast, a CTE approach using a nonclassical definition of mode mix provided excellent predictive capability for all polymeric matrix composites examined, including graphite-reinforced epoxies, graphite-reinforced toughened epoxies, graphite-reinforced epoxies with a toughened thermoplastic interlayer, and graphite-reinforced thermoplastics [3, 7, and 11-14]. Thus, two fundamental advantages for using the CTE approach over the conventional approach have been established. First, the CTE analysis provides increased modeling and computational efficiency. Second, the CTE approach allows both classical and nonclassical definitions of mode mix to be adopted. To distinguish these two advantages, the term CTE analysis is used to refer to the case where the CTE is used to determine energy release rate. For example, one may compare a 2D or 3D CTE analysis to a 2D or 3D FE analysis to verify that the CTE produces accurate predictions for ERR and classically defined mode mixity. The term CTE approach is used to denote when the CTE analysis is applied, along with appropriate experimentally determined toughness, to predict delamination growth. As will be shown subsequently, the CTE approach may be used in either a classical or nonclassical sense.

In previous works, several studies have been conducted to verify the accuracy of the CTE analysis. The CTE analysis has been applied to various 2D [1, 4, 7, 11, and 15-19] and 3D

[6, 12, and 20] structural problems, and the predicted ERR and classically defined mode mix were compared to predictions obtained using the conventional FE approach. This was essential to verify the basic mechanics of the CTE formulation. Initially, simple geometries were chosen, such as primarily flat plate geometries containing a delamination to verify 3D for mutation. Later, more complex hat-stiffened geometries were examined, and a good correlation between classical CTE and FE predictions was obtained [12].

In order to assess its predictive accuracy, the CTE approach was used, along with a nonclassical definition of mode mix, to predict delamination growth in a variety of materials, layups, and loadings. This involved extensive testing of flat test coupons comprised of unidirectional and multidirectional layups with mid-plane or offset delaminations. The predictions were then compared to experimental results and excellent correlation was obtained [11, 13, and 14]. A study was also conducted to show that the CTE approach is an accurate and effective method for predicting delamination growth in more complex aircraft structural geometries. For this purpose, the skin-stringer delamination problem was chosen because it is a typical structural problem faced by industry and it represents a fairly complex problem for verifying the CTE approach. Predictions by the CTE approach were compared to delamination growth data for skin-stringer specimens comprised of C12K/R6376 graphite/epoxy and excellent correlation was obtained [12]. As a final step in the verification process, a similar comparative study between theory and experimental is described herein. This study used a very different and significantly tougher next generation material system, T800H/3900-2. This material contains high strength T800H carbon fibers embedded in a base epoxy matrix with thermoplastic particulate interlayer toughening. The material attains its high toughness primarily due to the tough thermoplastic amorphous polyamide interlayer that is present between all plies. Conversely, the C12K/R6376 material is a relatively standard current generation graphite/epoxy that has a thermoplastic-toughened epoxy matrix that does not contain an interlayer. Therefore, verification of the CTE approach for the T800 material would establish its applicability for a wide range of material systems.

In this report, the CTE approach is used to predict delamination growth in two different T800H/3900-2 skin-stringer geometries that are typical to aircraft applications. Initially, ERR predictions obtained using CTE analyses were used with experimentally determined toughness data and the nonclassical definition of mode mix to obtain delamination growth predictions. The implementation of the CTE approach required a minor modification to the manner in which it had previously been used [12], i.e., a different finite element meshing technique was adopted. A substudy is presented to validate this modification, and predictions for the two geometries are obtained from this mesh. Next, the details of the manufacturing and testing of the chosen geometries is described. Experimental results are compared to the predictions and, initially, it is found that poor comparisons were obtained. This is followed by a detailed investigation to determine the reasons for the apparent discrepancies. It was found that different fracture behavior occurred in this material than in others that have been studied. A more representative fracture toughness model was therefore used to obtain revised predictions. The comparison between these revised predictions and the experimental results were found to be quite good. These results, and those from previous studies, are used to draw conclusions about the applicability of the CTE approach and an overall ERR-based approach for predicting delamination growth in various materials. Recommendations are made for future work as well as for application of the CTE approach to present-day structures.

2. APPROACHES FOR ERR DETERMINATION IN LAMINATED COMPOSITES.

2.1 OVERVIEW.

This section describes several different methods used to determine the energy release rate for a delaminated structural geometry that is subjected to arbitrary loading. The most commonly used methods use a classical analysis that is based on linear elastic fracture mechanics (LEFM). This section first reviews LEFM and briefly explains how the ERR is obtained using finite element (FE) analysis. Because this study focuses on skin-stringer geometries, the existing literature is next reviewed with emphasis on studies where this type of geometry was analyzed using the FE method. The CTE, which is the focus of this work, will be reviewed briefly. This is followed by a review of previous work where the CTE was used to predict ERR on various 2D and 3D structural problems. The predicted ERR were compared to those obtained using conventional FEA. This is done to establish that the CTE analysis is both computationally efficient and accurate for predicting ERR in complex structural problems. Further details of the CTE analysis and CTE approach for delamination growth predictions are presented in section 3.

2.2 LINEAR ELASTIC FRACTURE MECHANICS/SINGULAR FIELD APPROACH.

The conventional approach used to predict crack growth is based upon classical linear elastic fracture mechanics (LEFM). This solution is applicable if a so-called "singular field" or "zone of K-dominance" exists. In other words, there exists a near-tip region, outside the damage zone, where stress field equations are expressed through the mode I, II, and III stress intensity factors [21]. For these equations to apply, the size of the singular field must be large compared to the size of the damage zone. This issue is discussed further in section 2.3.

The most commonly used method for determining classically defined ERR components is the FE method coupled with the virtual crack closure technique (VCCT) [22]. The VCCT uses the nodal forces ahead of the delamination front and the displacements behind the delamination front to determine the ERR components. The VCCT is most commonly used for laminated composites for delamination between plies at the same orientation because it directly yields classical LEFM-based ERR components; that is, there is no need to first obtain the stress-intensity factors. Moreover, the VCCT may be used with any continuum element. Therefore, it lends itself well to the complex meshing techniques that composites often require. For delamination between plies at different orientations, a linear elastic analysis that models individual plies as equivalent homogenous layers will predict that an oscillatory stress singularity exists at the delamination front. This oscillatory field causes the ERR components to depend on the length of crack closure, and the mode mix to depend on the degree of mesh refinement in the vicinity of the crack tip [1, 23, and 24]. This behavior significantly complicates the implementation of any predictive methodology. A variety of methods have been proposed to eliminate the oscillatory portion of the singularity, such as the resin interlayer method [19, 23, and 24], the $\beta=0$ approach [1, 19, and 23], and the finite crack extension approach [25-27]. All of these methods may be used with the VCCT. However, further discussion of these methods and the oscillatory singularity is beyond the scope of this report. Instead, the reader is referred to references 3 and 12, where reviews of these approaches and evaluations of their accuracies are presented.

The VCCT has been commonly used to determine ERR in both simple and complex delaminated geometries that are subjected to various loadings. A typical structural configuration faced by industry is the skin-stringer delamination problem (also commonly referred to as skin-stringer debonding). In most cases, the delamination is assumed to occur between the skin and stringer, and the 2D FE analyses are used to obtain the ERR [28-30]. Recently, skin-stringer problems have also been analyzed using three-dimensional FE analyses [31-33], which allows the contribution from all three modes of fracture to the ERR to be identified. However, extensive effort is required to develop highly refined 3D models of the entire structure, and only a sub-region of the stiffened structure was therefore modeled in most cases. In addition, these 3D models required considerable computational time, and developing and modifying them required a great deal of human effort. This illustrates one of the primary limitations of the FE-based VCCT and, perhaps for this reason, this method has not been widely used by industry.

2.3 CRACK TIP ELEMENT ANALYSIS.

The CTE analysis provides a mostly analytical approach to determine ERR and mode mix using plate theory-based near-tip forces and moments. These near-tip quantities are typically obtained from a global FE analysis of the undamaged structure. The CTE analysis greatly reduces the modeling and computational efforts compared to conventional FE analysis. Another significant advantage of the CTE analysis is that the mode mix can be suitably chosen based upon the material under consideration. For example, for materials that exhibit a small damage zone, the LEFM assumptions are applicable and one may choose to use the classical definition. In this case, mode mix is defined in such a way that it allows the partitioning of the total ERR into mode I, II, and III components based upon classical, LEFM assumptions. This will be referred to as the crack tip element/singular field (CTE/SF) approach. For delamination between plies at different orientations, the CTE/SF can use the resin interlayer, $\beta=0$ or finite crack extension approach. The assumptions from any of these methods can be used with the CTE analysis to obtain the corresponding definition of mode mix. The CTE/SF can also be used to obtain the complex stress intensity factor that characterizes the oscillatory zone; this has been shown to yield essentially the same results as more conventional methods [1, 5, and 16].

Section 1 stated that the SF approach of mode decomposition did not provide accurate predictions for delamination growth in many laminated composites [3 and 7-11]. This is because for most laminated composites, the damage zone may be relatively large compared to the characteristic dimension of the problem, which is typically on the order of a single ply to several ply thicknesses. When the damage zone is larger than this characteristic dimension (which also scales the size of the singular field), the assumption of the classical theory breaks down. In such a case, the ERR is still applicable for making delamination growth predictions in laminated structures, but the conventional definition of mode mix, based on classically defined stress-intensity factors and/or ERR components, is no longer appropriate. In cases where the classical method does not work, the CTE analysis may be used to obtain alternate definitions of mode mix: i.e., partitioning of total ERR into nonclassical mode I, II, and III components.

One particular choice of mode decomposition, originally developed in reference 7, has been referred to as the crack tip element/nonsingular field (CTE/NSF) approach. That is, the ERR components are not based on classical LEFM or singular field assumptions. In reference 7, the CTE/NSF approach was found to provide highly accurate predictions for delamination growth in

a toughened graphite/epoxy system, and subsequent studies have established that this approach is well suited for all fibrous polymeric matrix composite systems.

The following sections review the 2D and 3D CTE analyses. For each case, the formulation is slightly different. Since this work utilizes only the 3D CTE analysis, in what follows, only a brief review of the 2D CTE analysis is given. Subsequently, emphasis is placed on the 3D analysis.

2.3.1 Two-Dimensional Crack Tip Element.

Previously, a considerable amount of work was done using the 2D CTE analysis in order to establish the basic mechanics of the CTE formulation. This was accomplished by comparing ERR predictions obtained from CTE/SF analyses and the conventional FE-based analyses.

The governing equations and all other details needed to apply the 2D CTE analysis are given in reference 1. The accuracy of this analysis has been verified against FE-based analyses for a wide variety of problems. The CTE predictions for ERR and mode mix were compared to the FE predictions for problems where the delaminations were bounded by plies at the same orientation [1 and 4] and for cases where the delaminations were between plies at different orientations [1, 5, and 16]. The 2D CTE analysis was applied and compared to FE results for the instability-related delamination growth problem [15]. The problem of free-edge delamination [16-19 and 23] was also investigated using 2D CTE and the results compared to FE predictions. In all cases, excellent correlation was obtained between the CTE/SF and FE predictions for ERR and classically defined mode mix.

The above studies clearly show that the formulation of the 2D CTE is correct. They also indicate that the CTE provides a highly efficient method for predicting ERR as compared to the FE-based method. It may be noted again that for most laminated composites, the CTE/SF and FE-based approaches of total ERR decomposition are not very accurate for predicting delamination growth. However, the above comparative studies indicated that the 2D CTE analysis may be used to accurately obtain total ERR as well as to partition it into classically defined components. One may also choose to use the CTE along with the NSF-based definition of mode mix for delamination growth predictions. Of course, the 2D CTE method can only be used for plane stress or plane strain problems where a mode III ERR component is not present. For other cases, the 3D CTE may be used. The next section gives a brief overview of the 3D CTE.

2.3.2 Three-Dimensional Crack Tip Element.

This section reviews the verification of the 3D CTE analysis. As was done for the case of 2D CTE, the accuracy of this formulation was assessed by comparing the ERR and mode mix predictions to those obtained from the FE method for several types of 3D problems. A number of flat plate geometries subjected to various loadings were solved using 3D CTE and the FE method. This was done for cases where the delaminations were bounded by plies at the same orientation [5, 6, 12, and 20] and for cases where the delaminations were bounded by plies at different orientations [12 and 20]. For delaminations between plies at the same orientation, ERR components were determined by the crack tip element using the classical definition and were compared to the results from the 3D finite element analysis and the VCCT. For the cases where

delaminations were between plies at different orientation, it was mentioned earlier that the classical analysis predicts an oscillatory singularity at the delamination front, and classical ERR components cannot be defined. Hence, in references 12 and 20, CTE predictions for ERR components were obtained by incorporating the assumptions of the finite crack extension (FCE) approach into the mode mix definition. Note, the FCE approach provides a means to ignore the oscillatory nature of the singularity at the delamination front. The CTE-based ERR components were compared to results by 3D FE analyses and VCCT, which also used the FCE approach, and good correlation was obtained. The accuracy of the 3D CTE was also assessed for typical skin-stringer configurations by comparing the 3D CTE/SF-based ERR predictions to the 3D FE results [12]. These comparisons showed good correlation and indicated that the CTE analysis is quite accurate for total ERR and singular field-based mode mix, even for complex geometries. The results from the study on the skin-stringer configurations will be reviewed in section 4. The above comparisons clearly indicate that the crack tip element may be used to accurately determine ERR components in practical problems of delamination where these components are defined using classical approach for predicting delamination growth. These works also established that the CTE analysis considerably reduces development and computational efforts as compared to a 3D FE approach. The CTE analysis may be used with the CTE/NSF approach, which provides better predictive accuracy than the SF-based approach for those materials where a singular zone does not exist. As such, the CTE provides an accurate, efficient, and versatile technique for predicting delamination growth in a wide variety of materials and structures.

3. THREE-DIMENSIONAL CRACK TIP ELEMENT METHODOLOGY.

3.1 BACKGROUND.

This section presents the equations needed to apply the 3D CTE analyses and a general description of the CTE approach for predicting delamination growth. The 3D CTE equations presented here were directly taken from reference 12. The 3D crack tip element accounts for all variations in ERR that occur along a delamination front with the exception of the "classical edge effect," and associated edge dimpling, that occurs at a free edge. However, it has been shown that this effect is quite small and does not significantly affect the accuracy of the 3D CTE predictions [5, 12, and 20].

Figure 3-1 shows the generic geometry and loading of the 3D CTE. Figure 3-1 can also be seen as a general representation of the geometry and loading near the delamination tip of a typical structural detail. The region directly above and below the crack will be referred to as leg 1 and leg 2, respectively, and the uncracked region will be referred to as region u. All superscripts on the loading labels in figure 3-1 refer to these designations. Although it is not shown in the figure for clarity, it is possible that a twisting moment, $M_6{}^u$, exists in the uncracked region to enforce global equilibrium. The origin of the x,z coordinate system shown in the figure 3-1 is at the crack tip at the mid-plane of the uncracked region.
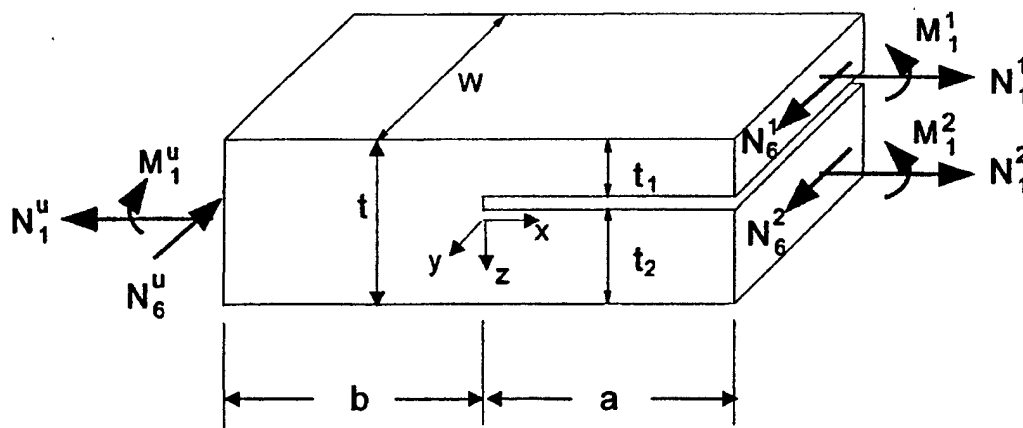
FIGURE 3-1. THREE-DIMENSIONAL CRACK TIP ELEMENT AND REMOTE LOADING

In figure 3-1, it is assumed that the plate dimensions, a, b, and W, are large compared to the thicknesses of t_1, t_2, or t. The applied loading may be considered to be the loading shown in the figure, or it may be found from some intermediate analysis, but in either case it is assumed to be remote from the crack tip. A double-plate (plate theory FE model) is used to determine the loading close to the crack tip for the 3D CTE analysis. Figure 3-1 is modeled as two separate plates: plate 1 is the top portion of the geometry above the crack plane and plate 2 is for the portion below. Both plates are modeled using standard shear-deformable plate elements. Because the elements are defined such that their nodes lie along their mid-plane, the upper plate model (plate 1) is physically located along the plane defined by the mid-plane of the upper

cracked region. Similarly, the lower plate model (plate 2) is located along the mid-plane of the lower cracked region. The two plate models consist of precisely the same mesh. In the uncracked region, nodes occupying the same (x,y) locations were constrained by equations that enforced displacement compatibility between the (fictitious) top surface of the lower plate model and the (fictitious) bottom surface of the upper plate model. This is enforced through multipoint constraint equations. For a pair of nodes at the same (x,y) location, these equations are given by:

$$u_1 - \frac{t_1}{2}\theta_1 = u_2 + \frac{t_2}{2}\theta_2$$

$$v_1 - \frac{t_1}{2}\phi_1 = v_2 + \frac{t_2}{2}\phi_2 \tag{3-1}$$

$$w_1 = w_2$$

where:

u_1, v_1 and w_1 are the displacements in the x, y, and z directions, respectively, of the mid-plane of the top plate (plate 1);

u_2, v_2 and w_2 are the displacements in the x, y, and z directions, respectively, of the mid-plane of the bottom plate (plate 2);

θ_1 and θ_2 are the x direction slopes (rotations about y) of the mid-planes of plate 1 and plate 2, respectively; and

ϕ_1 and ϕ_2 are the y direction slopes (rotations about x) of the mid-planes of plate 1 and plate 2, respectively.

Equation 3-1 enforces displacement compatibility along the plane of the crack, in the uncracked region, in accordance with classical plate theory. However, in the present formulation, first-order shear deformable plate elements are used in the finite element model. In first-order theory, the slope of the mid-plane is due to the combined effect of bending and shear, whereas in classical plate theory only the former contribution is included [34]. Thus, equation 3-1, when used with shear deformable elements, does not exactly enforce displacement compatibility. There are three primary reasons why this approach was adopted.

1.   The most commercially available FE packages do not allow the shear strain to be included in the constraint equations. This would be necessary to precisely enforce displacement compatibility when using the first-order shear deformable plate theory equations.

2.   The present approach has been evaluated against an alternative approach, where classical plate theory elements were used in the uncracked region. In this way, displacement compatibility was strictly enforced along the crack plane. However, the use of equation 3-1 with the shear deformable plate elements gave better results for ERRs than this alternative approach for a wide variety of problems that were studied.

3.   A large number of problems have also been solved using first-order shear deformable plate elements where the nodes were offset with respect to the mid-plane of the element [5].

In this approach, plate 1 is modeled using elements with nodes along their lower surface, and plate 2 is modeled using elements with nodes along their upper surface. Displacement compatibility is enforced in the uncracked region by simply constraining collocated nodes to have the same displacements. For all problems studied to date, no difference was observed between these results and those using conventional shear deformable plate elements [5]. Because only a limited number of commercially available FE codes have plate elements with offset nodes, the method will be presented using conventional elements. However, if one desires, it is not difficult to modify the above constraint equations and use the method with elements with offset nodes. This approach will precisely enforce displacement compatibility at the crack plane. When this is done, it is important that all forces and moments used in the CTE analysis be defined with respect to the mid-plane of plates 1, 2, and the uncracked region. These values are typically output at the elements' nodes, in which case one must use static equilibrium considerations to obtain the equivalent system at the various mid-planes. Other than this caveat (and the different constraints), the method is unchanged. For all problems studied to date, the transverse shear correction factors, k_x and k_y [34], have been taken as 5/6.

3.2 TOTAL ERR DETERMINATION.

The total ERR is obtained directly from the double-plate finite element model by a plate theory-based crack closure procedure. It involves subjecting the plate theory finite element model to a specified remote loading to obtain the plate theory forces, $\{N_1, N_2, N_6\}$, and moments, $\{M_1, M_2, M_6\}$. This is one-half of one element away from the crack tip in both the cracked and uncracked regions at all y locations along the delamination front. That is, at a given value of y, the values of $\{N_1, N_2, N_6\}$ and $\{M_1, M_2, M_6\}$ can be obtained at the centroidal location of each of the four elements adjacent to the crack tip. The four elements are located in the cracked and uncracked region of plates 1 and 2. The plate theory-based crack closure process yields at each y location corresponding to the centroids of the four elements adjacent to the crack tip [6].

$$G = \frac{1}{2} \sum_{j=1}^{2} \left(\Delta N_i \Delta \varepsilon_i^o + \Delta M_i \Delta \kappa_i \right)_j, \qquad i = 1,2,6 \qquad (3\text{-}2)$$

Both i and j are summed in the above equation. Also, ε_i^o and κ_i ($i = 1,2,6$) refer to the classical laminated plate theory (CLPT) mid-plane strain and curvature, respectively; $j = 1,2$ corresponds to the quantities for plates 1 and 2, respectively, and standard nomenclature is used for N_i, M_i, ε_i^o and κ_i [34]. In equation 3-2, ΔN_i, ΔM_i, $\Delta \varepsilon_i^o$, and $\Delta \kappa_i$ are obtained from the forces and moments (N_i and M_i) obtained from the four elements adjacent to the crack tip as described below.

At any location of y, the plate theory forces, $\{N_1, N_2, N_6\}$ and moments $\{M_1, M_2, M_6\}$ are obtained in plate 1 (the upper plate) in the cracked and uncracked region, and in plate 2 (the lower plate) in the cracked and uncracked region. These values are then used with the standard

laminated plate theory equations to obtain the strains and curvatures in each of the cracked regions using

$$\begin{Bmatrix} \varepsilon^o \\ \kappa \end{Bmatrix}_c^p = \begin{bmatrix} \alpha & \beta \\ \beta^T & \delta \end{bmatrix}^p \begin{Bmatrix} N \\ M \end{Bmatrix}_c^p \qquad (3\text{-}3)$$

In equation 3-3, p takes on the values 1 or 2 for plates 1 or 2, respectively, while subscript c denotes that these values are within the cracked region. The (α-β-δ) matrix that appears in equation 3-3 is the standard (6 x 6) matrix of classical laminated plate theory [34]. For the uncracked region, the forces and moments are found from the values taken from the FE output for plates 1 and 2, in the uncracked region, using the following equations of static equilibrium:

$$\{N\}_u = \{N\}_u^1 + \{N\}_u^2 \qquad (3\text{-}4)$$

$$\{M\}_u = \{M\}_u^1 + \{M\}_u^2 + \frac{t_1}{2}\{N\}_u^2 - \frac{t_2}{2}\{N\}_u^1 \qquad (3\text{-}5)$$

In the above, the subscript u denotes that these values are for the uncracked region, and the superscripts 1 and 2 denote that these values were taken from the plate elements, within the uncracked region, belonging to plates 1 or 2, respectively. The forces and moments computed in equations 3-4 and 3-5 are then used to obtain the mid-plane strains and curvatures in the uncracked region. Following CLPT, this yields

$$\begin{Bmatrix} \varepsilon^o \\ \kappa \end{Bmatrix}_u = \begin{bmatrix} \alpha & \beta \\ \beta^T & \delta \end{bmatrix}_u \begin{Bmatrix} N \\ M \end{Bmatrix}_u \qquad (3\text{-}6)$$

The mid-plane strains for the portions of the uncracked region that comprise plates 1 and 2 can be found from the results of equation 3-6 as

$$\{\varepsilon^o\}_u^1 = \{\varepsilon^o\}_u - \frac{t_2}{2}\{\kappa\}_u \qquad (3\text{-}7)$$

$$\{\varepsilon^o\}_u^2 = \{\varepsilon^o\}_u + \frac{t_1}{2}\{\kappa\}_u \qquad (3\text{-}8)$$

The curvature of the mid-planes of plates 1 and 2 in the uncracked region are equal to the curvature computed in equation 3-6. Finally, the quantities used in equation 3-2 can now be calculated from the results of equations 3-3 through 3-8 as

$$\begin{Bmatrix} \Delta\varepsilon^o \\ \Delta\kappa \end{Bmatrix}^p = \begin{Bmatrix} \varepsilon^o \\ \kappa \end{Bmatrix}_u^p - \begin{Bmatrix} \varepsilon^o \\ \kappa \end{Bmatrix}_c^p \qquad (3\text{-}9)$$

$$\begin{Bmatrix} \Delta N \\ \Delta M \end{Bmatrix}^p = \begin{bmatrix} A & B \\ B & D \end{bmatrix}^p \begin{Bmatrix} \Delta\varepsilon^o \\ \Delta\kappa \end{Bmatrix}^p \qquad (3\text{-}10)$$

As before, the superscript p in the above equations takes on the values 1 or 2 for plates 1 and 2, respectively. The $[A\text{-}B\text{-}D]$ matrix of equation 3-10 is the value for plate 1 or 2 following standard CLPT notation.

3.3 MODE DECOMPOSITION.

At each location along the delamination front where the total ERR was obtained (i.e., each y location), the mode I and mode II components, G_I and G_{II}, respectively, are obtained using [6 and 20]

$$G_I = \frac{1}{2}\left[-\sqrt{c_{11}}N'_c \sin\Omega + \sqrt{c_{22}}M'_c \cos(\Omega + \Gamma')\right]^2 \qquad (3\text{-}11)$$

$$G_{II} = \frac{1}{2}\left[\sqrt{c_{11}}N'_c \cos\Omega + \sqrt{c_{22}}M'_c \sin(\Omega + \Gamma')\right]^2 \qquad (3\text{-}12)$$

where

$$\sin\Gamma' = \frac{c'_{12}}{\sqrt{c_{11}c_{22}}} \qquad (3\text{-}13)$$

The mode III component is then obtained as

$$G_{III} = G - G_I - G_{II} \qquad (3\text{-}14)$$

Where G is obtained using equation 3-2.

In equations 3-11 and 3-12, N'_c and M'_c are the 3D concentrated crack tip force and moment, respectively. The quantities c_{11}, c_{22}, and c'_{12} are functions of the material properties and layup of the plate. Expressions for these parameters are presented below. This is followed by a discussion of the choice of the mode mix parameter, Ω. This parameter may be suitably chosen to yield classical or nonclassical mode decompositions.

The 3D concentrated crack tip force and moment, N'_c and M'_c, are found by enforcing the condition that $\varepsilon_2^0 = \kappa_2 = \kappa_6 = 0$ in the cracked and uncracked near-tip regions. They are given by [6]

$$N'_c = -N_1^1 + \tilde{N}_1$$
$$M'_c = M_1^1 + N'_c \frac{t_1}{2} - \tilde{M}_1 \qquad (3\text{-}15)$$

where N^1_1 and M^1_1 are obtained from the cracked region of plate 1, and $\tilde{N}_1$ and $\tilde{M}_1$ are the internal force and moment resultants, respectively, in the portion of plate 1 that is in the uncracked region of the element. These latter quantities are given by [6 and 20]

$$\widetilde{N}_1 = R_{11}^1 \left(\varepsilon_1^o - \kappa_1 t_2 / 2 \right)^u + R_{12}^1 \left(\varepsilon_6^o \right)^u + R_{13}^1 \left(\kappa_1 \right)^u$$

(3-16)

$$\widetilde{M}_1 = R_{31}^1 \left(\varepsilon_1^o - \kappa_1 t_2 / 2 \right)^u + R_{32}^1 \left(\varepsilon_6^o \right)^u + R_{33}^1 \left(\kappa_1 \right)^u$$

In the above, $(\varepsilon_1^o)^u$, $(\varepsilon_6^o)^u$, and $(\kappa_1)^u$ are the mid-plane strains and curvature in the uncracked plate under conditions where $\varepsilon_2^o = \kappa_2 = \kappa_6 = 0$ [6]. They are given as

$$\begin{Bmatrix} \varepsilon_1^o \\ \varepsilon_6^o \\ \kappa_1 \end{Bmatrix}^u = r^u \begin{Bmatrix} N_1 \\ N_6 \\ M_1 \end{Bmatrix}^u$$

(3-17)

where N_1^u, N_6^u, and M_1^u are the plate theory forces and moment in the uncracked region, and are given by global equilibrium as (cf. figure 3-1):

$$\begin{Bmatrix} N_1 \\ N_6 \\ M_1 \end{Bmatrix}^u = \begin{Bmatrix} N_1^1 + N_1^2 \\ N_6^1 + N_6^2 \\ M_1^1 + M_1^2 + N_1^2 t_1 / 2 - N_1^1 t_2 / 2 \end{Bmatrix}^c$$

(3-18)

In equation 3-16, all R_{ij}^1 terms are the elements of the reduced stiffness matrix R^1, where the superscript 1 refers to plate 1. The reduced stiffness matrix is given as [6]

$$R = \begin{bmatrix} A_{11} & A_{16} & B_{11} \\ A_{16} & A_{66} & B_{16} \\ B_{11} & B_{16} & D_{11} \end{bmatrix}$$

(3-19)

where A_{ij}, B_{ij} and D_{ij} are the elements of the standard (6 x 6) stiffness matrix of classical laminate plate theory. In equation 3-17, r^u is the inverse of the reduced stiffness matrix for the uncracked region.

The coefficients c_{11}, c'_{12} and c_{22} in equations 3-11 through 3-13 are given by [6 and 20]

$$c_{11} = r_{11}^1 + r_{11}^2 + r_{13}^1 t_1 - r_{13}^2 t_2 + r_{33}^1 t_1^2 / 4 + r_{33}^2 t_2^2 / 4$$

$$c'_{12} = -r_{13}^1 - r_{13}^2 - r_{33}^1 t_1 / 2 + r_{33}^2 t_2 / 2$$

(3-20)

$$c_{22} = r_{33}^1 + r_{33}^2$$

In the above, the superscripts on the r_{ij} refer to plate 1 or 2. For those cases where $A^i{}_{16} = B^i{}_{16} = 0$, $i = 1, 2, u$, it is readily shown that c_{11}, c'_{12}, and c_{22} reduce to c_1, c_{12}, and c_2 of the plane strain 2D crack tip element [1].

To obtain mode mix by the CTE equations, the plate theory force and moment resultants are obtained at the centroids of the elements adjacent to the crack tip, and in the cracked region, in plates 1 and 2 as functions of y. These force and moment distributions are used to obtain the N'_c and M'_c distributions, and equations 3-11, 3-12, and 3-14 are used to obtain the individual ERR components across the width of the plate.

3.3.1 Classical, Singular Field-Based Approach.

As classical laminated plate theory (CLPT) was used to derive the crack tip element equations, the effectiveness of the 3D CTE approach to capture the exact, singular field solution depends upon the contribution of transverse shear strain (γ_{xz} and γ_{yz}) to the total strain energy. For most practical problems of delamination, the slenderness (length-to-thickness) ratio is typically quite large, and as a result, the importance of transverse shear deformation decreases in comparison to classical bending deformations [34]. In these cases, the CTE analysis results will coincide with the exact, singular field-based results when delamination growth is between plies at same orientation and the singular field-based value of Ω, referred to hereafter as Ω_{SF}, is used. Ω_{SF} is obtained using a single 2D, plane strain FE analysis of the laminate following the same procedure described in reference 1. The singular field-based value of Ω is independent of the loading and depends only upon the local material properties and layup at the delamination front [1].

For cases where the delamination is between plies at different orientations, the classical approach predicts an oscillatory singularity at the delamination front, and consequently, classical ERR components cannot be defined. In such cases, the resin interlayer method, $\beta = 0$ approach or FCE approach, can be used. Any of these definitions of mode mix can be obtained by the CTE analysis by using the appropriate assumptions in the 2D, plane strain FE analysis that is used to obtain Ω.

For the special case where the delamination is present at the mid-plane of a symmetric laminate, $\Omega_{SF} = 0$. For all other cases, the singular field-based 3D CTE requires only a single 2D continuum analysis of the crack tip region to obtain Ω_{SF}, and all other determinations of ERR and mode mix are performed using relatively simple plate models. This results in a computationally efficient technique that produces essentially the same results as 3D finite element analyses.

3.3.2 Nonclassical, Nonsingular Field Approach.

Recently, the singular field-based methods of defining mode mix have been shown to provide poor predictive capability for most laminated composites [3 and 7-11]. To establish this, experimental studies were conducted, where specimens with various geometries and a pre-implanted delamination were subjected to a variety of loadings. It was shown that test specimens for which singular field-based methods predicted the same mode mix did not display the same

toughness, i.e., the classical approach demonstrated poor predictive capability. Therefore, an alternate methodology is required to accurately predict delamination growth in many material systems.

The alternate nonclassical approach uses CTE analysis along with an expression for Ω that is dependant only on thickness ratio. This expression for Ω was obtained experimentally for the C12K/R6376 material system [7], and subsequently, it was found to be valid for all materials and layups [12]. The nonclassical approach is not based on the singular field assumptions, and hence the term CTE/NSF, where NSF denotes nonsingular field, has been used in previous works [3, 7, 11, 16, and 20] to describe this approach. The quantities that are used to define the CTE/NSF mode mix are only dependent upon the loading conditions at the crack tip and are insensitive to the details of any near-tip damage. As such, the method is well suited for characterizing the dependence of toughness on remote loading for materials that exhibit large damage zones. The expression for Ω used in the CTE/NSF approach is given by:

$$\Omega = \begin{cases} -24 & \eta < -0.468 \\ 60.409\eta - 41.738\eta^3 & if \quad -0.468 < \eta < 0.468 \\ 24 & \eta > 0.468 \end{cases} \qquad (3-21)$$

where $\eta = \log_{10}(t_2/t_1)$ and Ω is given in degrees. It should be noted that the NSF expression for Ω depends only on the ratio of the thicknesses of the upper and lower cracked regions. Hence, the only difference between the singular field-based and NSF analyses is in the definition of Ω, except for the special case of a mid-plane symmetric laminate with a mid-plane delamination. For such a case, the nonclassical expression for Ω gives a value of zero and the same ERR predictions are obtained from the singular field-based and NSF approaches. For all cases examined to date, including several geometries comprised of four different material systems [3 and 11-14], the CTE/NSF mode decomposition has been shown to be a more accurate method for making delamination growth predictions compared to the classical approach.

3.4 CTE APPROACH FOR DELAMINATION GROWTH PREDICTIONS.

In this section, the overall CTE approach for predicting delamination growth is summarized. First, the structure of interest is modeled using a double-plate, plate theory FE model. The delaminated region is modeled by simply removing the constraint equations (3-1) from the affected nodes in the FE model. Appropriate boundary and loading conditions are then applied to the FE model, and the plate theory forces and moments within the elements near the vicinity of the crack tip at all locations along the delamination front are obtained from the FE output. These quantities are used to calculate the ERRs using equations 3-2, 3-11, 3-12, and 3-14.

The mode mix definition (SF or NSF) that is considered appropriate for the problem is used. The mode mix parameter, Ω, for the SF approach is obtained using a single 2D, plane strain FE analysis of the laminate. For the NSF approach, equation 3-21 is used to obtain Ω.

The next step in the process is to define mode mix. Many of the mixed-mode problems studied to date have focused on the combination of mode I-II loading only. For such a case, mode mix may be defined as the ratio of either the mode I or mode II ERR to the total ERR. As will be shown subsequently, a mode III ERR will also occur in many 3D geometries. Therefore, for a mixed-mode I-II-III problem two mode mixities must be specified in addition to total ERR in order to uniquely define all ERR components. However, the mode mix also has to be defined in such a way that it is well suited for predicting delamination growth, and this definition also depends upon the availability of experimental toughness data. To date, toughness versus mode mix curves have only been developed for mixed-mode I-II loadings and there is not, at present, any established way of developing a mixed-mode I-II-III fracture interaction diagram (that is, a toughness versus mode mix surface [35]). It also appears unlikely that any methodology for this will be developed in the near future.

From a practical viewpoint, one is therefore forced to predict delamination growth in a mixed-mode I-II-III problem using toughness data obtained solely from mixed-mode I-II loadings. This can be achieved by combining G_{II} and G_{III} to give the component of ERR due to shear, G_S. The ratio of G_S/G may be then used in lieu of G_{II}/G to obtain the toughness from the mixed mode I-II toughness results (G_C versus G_{II}/G). This approach was used in the combined experimental-theoretical study of references 36 and 37. In the latter work, it was shown that the ratio of G_S/G may be used in lieu of G_{II}/G to determine toughness for mixed-mode II-III loadings of multidirectional end-notched flexure specimens. A similar conclusion on structural adhesives was reached in reference 38. The use of G_S/G in lieu of G_{II}/G was also adopted in reference 31, which is a theoretical (3D FE) study of skin-stringer delamination. This approach will also be adopted herein.

Once the mode mix has been defined, the appropriate fracture toughness curve is used (SF or NSF) and the fracture toughness corresponding to the mode mix of interest (i.e., that found for the structure of interest) is obtained. If a singular field-based approach is used to predict delamination growth, then the G_C versus G_{II}/G results used must be obtained (i.e., from fracture test data) using the SF definition of mode mix. When the CTE/NSF approach is used to make delamination growth predictions, then the G_C versus G_{II}/G results used must be obtained by reducing test data using the CTE/NSF approach. Additional details on this methodology are presented in reference 12. For the study described herein, the toughness versus mode mix results are taken from reference 12, and a NSF definition of mode mix is used.

Once G_C at each point along the delamination front is known, these values may be used to determine the globally applied load at which delamination advance at any given point will occur. Since G varies as the square of the applied load, and growth occurs when $G = G_C$, the predicted load for initiating delamination is obtained by scaling the applied load by the square root of G_C/G. This is done for each point along the delamination front, and the lowest predicted load is taken as the initiation value. The procedure for obtaining delamination growth predictions is discussed in more detail in section 5.6.2.

4. VERIFICATION OF THE CTE APPROACH USING C12K/R6376 SKIN-STRINGER GEOMETRIES.

4.1 OVERVIEW.

Previous publications [6 and 20] have shown that 3D CTE analysis are excellent comparison to 3D FE analysis (FEA) results for flat-plate problems that were subjected to various edge loadings. This was reviewed in section 2.3.2, and it was instrumental in establishing the accuracy of the 3D CTE analysis. This section presents a detailed review of previous publications that evaluated the accuracy and capability of the 3D CTE analysis when applied to skin-stringer geometries. ERR predictions for these geometries were obtained using a double-plate FE model and the 3D CTE, and the results were compared to those obtained by a 3D FEA of the same problem. These results are reviewed first. Next, previous experimental work is reviewed where skin-stringer geometries were used to assess the accuracy of the CTE approach for predicting delamination growth. The C12K/R6376 graphite/epoxy material system was used in the studies reviewed in this section. All results in this section are taken directly from reference 12.

4.2 SKIN-STRINGER GEOMETRIES.

The first assessment of the 3D CTE analysis involved an evaluation of energy release rates for delamination in a typical skin-stringer configuration that was subjected to bending loads. The stiffened-skin geometry considered is presented in figure 4-1. The geometry consists of a section of flat sheet that is 101.6 mm (4.0″) wide and 177.8 mm (7.0″) long. The sheet is reinforced by a hat-stiffener that is 38.1 mm (1.5″) wide at its base, 25.4 mm (1.0″) wide at its top, and 38.1mm (1.5″) in height. The stiffener's flanges are each 15.88 mm (0.625″) wide. The skin and stringer are bonded along these flanges and are assumed to be co-cured. That is, no bonding agent other than the material's resin system is used. The stringer is a little shorter than the skin, and it is assumed that a delamination exists along the final 9.53 mm (0.375″) of the length of the stringer. Figure 4-2 presents the loading on the skin-stringer geometry. Referring to this figure, the span is taken as 127 mm (5.0″) and the crack length is taken as 19.05 mm (0.75″). An applied load of 100N (22.48 lbf) acts at the mid-span point and is distributed evenly over the sheet section. This specific geometry was chosen to correspond to the experimental configuration used in section 5 of this report.
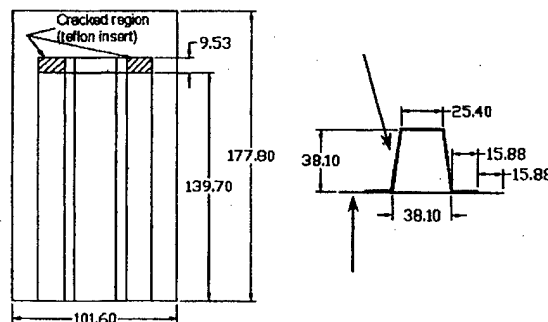
FIGURE 4-1. SKIN-STRINGER GEOMETRY CONSIDERED: BENDING LOADS
(All dimensions in mm)

To assess the accuracy of the 3D CTE formulation for this geometry, energy release rates and mode mixities were obtained for geometries comprised of various layups that were subjected to the loading of figure 4-2. One set of predictions was obtained using a double-plate FE model and the 3D CTE/SF analysis. The same problems were then solved using a 3D continuum FEA, and the results for the total ERR and its components were compared. Material properties corresponding to the Ciba-Geigy C12K/R6376 graphite/epoxy material system were used. The properties of this material are presented in table 4-1. All geometries considered contained six plies in each of the skin and stringer sections.
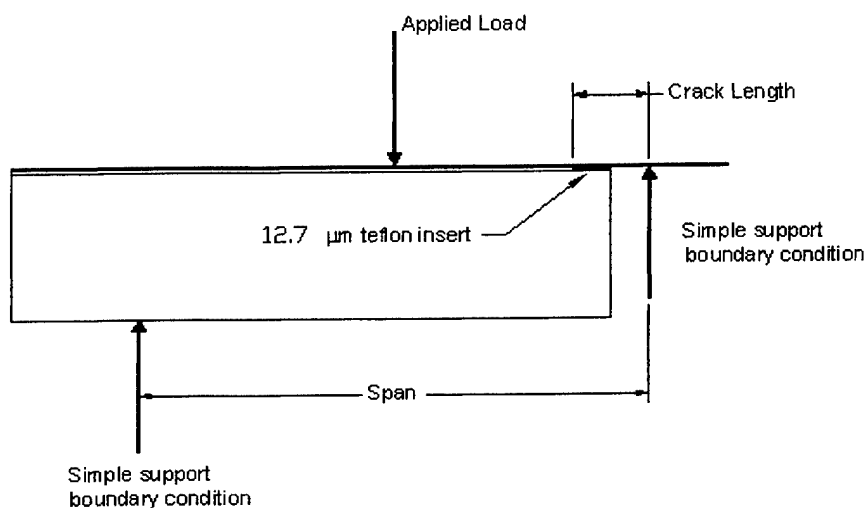
FIGURE 4-2. SKIN-STRINGER GEOMETRY SUBJECTED TO BENDING LOADS

TABLE 4-1. UNIDIRECTIONAL MATERIAL PROPERTIES OF C12K/R6376 GRAPHITE/EPOXY

$E_{11} = 146.86$ GPa	$E_{22} = 10.62$ GPa	$E_{33} = 10.62$ GPa
$G_{12} = 5.45$ GPa	$G_{13} = 5.45$ GPa	$G_{23} = 3.99$ GPa
$v_{12} = 0.33$	$v_{13} = 0.33$	$v_{23} = 0.33$
Single ply thickness: 0.1397 mm		

4.2.1 Finite Element Models.

All FE models were constructed and solved using Abaqus, licensed from Hibbitt, Karlsson, and Sorensen, Inc. As in the previous cases, 8-noded shear deformable elements were used for the plate theory finite element models, while 20-noded brick elements were used for the 3D continuum FE models. Two different plate models, with various levels of mesh refinement, were considered. There were slight differences in predictions for ERR in the edge regions between the two models; thus, the more refined model was used for all calculations. Figure 4-3 shows the isometric view of this model, while figure 4-4 presents the mesh for just the sheet portion of the plate theory model. The three-direction is consistent with the out-of-plane z direction in figure 3-1. The element length at the crack tip, in the direction of crack advance, is 0.0349 mm

(0.001375″), or 25% of a single ply thickness. All elements in this model have a width of 0.794 mm (0.03125″). The coordinate system shown in the figures is used to construct the FE model. The z = 0 plane corresponds to the plane of the crack, but the (x,y) origin does not correspond to the coordinate system used for the 3D CTE in figure 3-1. However, if one defines the hat-stiffener as plate 1 and the sheet region as plate 2, then all of the sign conventions for forces and moments for this model and the 3D CTE conventions (cf. figure 3-1) will coincide.
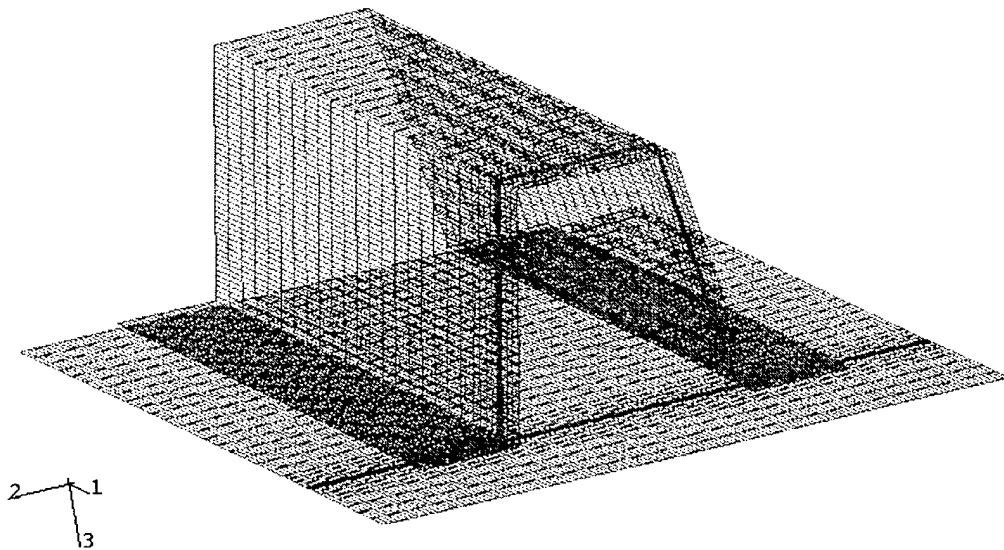
FIGURE 4-3. ISOMETRIC VIEW OF PLATE ELEMENT MODEL OF SKIN-STRINGER GEOMETRY
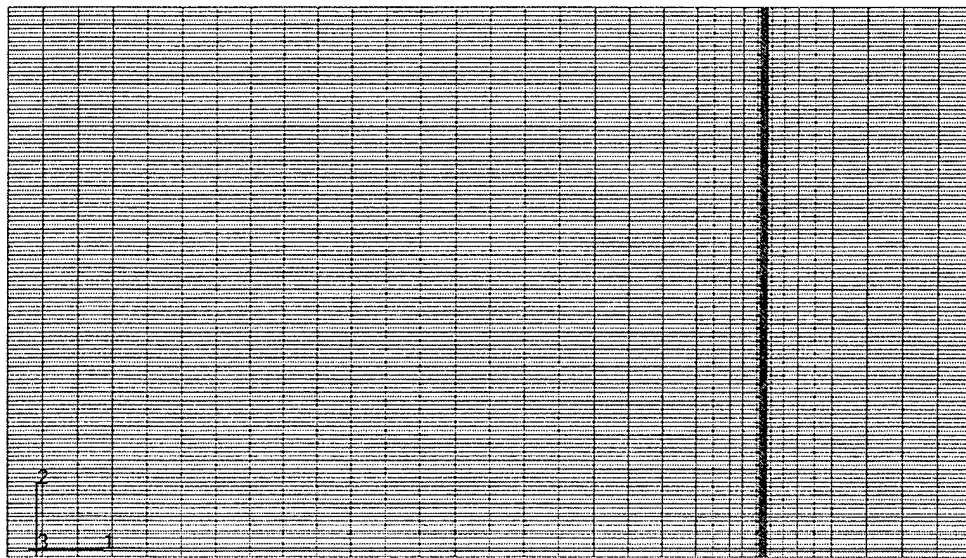
FIGURE 4-4. SHEET PORTION OF MESH OF PLATE ELEMENT MODEL OF SKIN-STRINGER GEOMETRY

As shown in figure 4-3, the location in space of the hat-stiffener portion of the model corresponds to the mid-plane of the physical hat-stiffener, while the location in space of the sheet portion of the model corresponds to the mid-plane of the physical sheet. Equation 3-1 was used between the nodes in the flange portions of the stiffener and the corresponding sheet locations to ensure that the bonded portions maintained compatible displacements. The plate element model was then globally loaded and constrained in accordance with figure 4-2, and the ERR and ERR components along the delamination fronts (i.e., along both flanges of the hat stiffener) were obtained using the 3D CTE equations and procedures described in sections 3.2 and 3.3.

Figure 4-5 shows the top view of the 3D FE model of the skin-stringer geometry, and figure 4-6 shows the front view. Because of the density of the mesh and scale used, individual elements are not visible in figure 4-6. Figure 4-7 shows a close-up of the corner region of this model. The mesh of the 3D FE model is similar to the plate element model, in that the elements at the crack tip are 0.0349 mm (0.001375″) long. However, due to the large computational requirements of the 3D model, the width of the elements are 1.588 mm (0.0625″), or twice the width of those used in the plate element model. Despite its reduced refinement with respect to elements across the specimen's width, the 3D FE model took over an order of magnitude longer to calculate than the plate theory model. Moreover, developing and debugging the 3D FE model was an extended and difficult process; whereas the same procedures for the plate theory model took only a few hours.
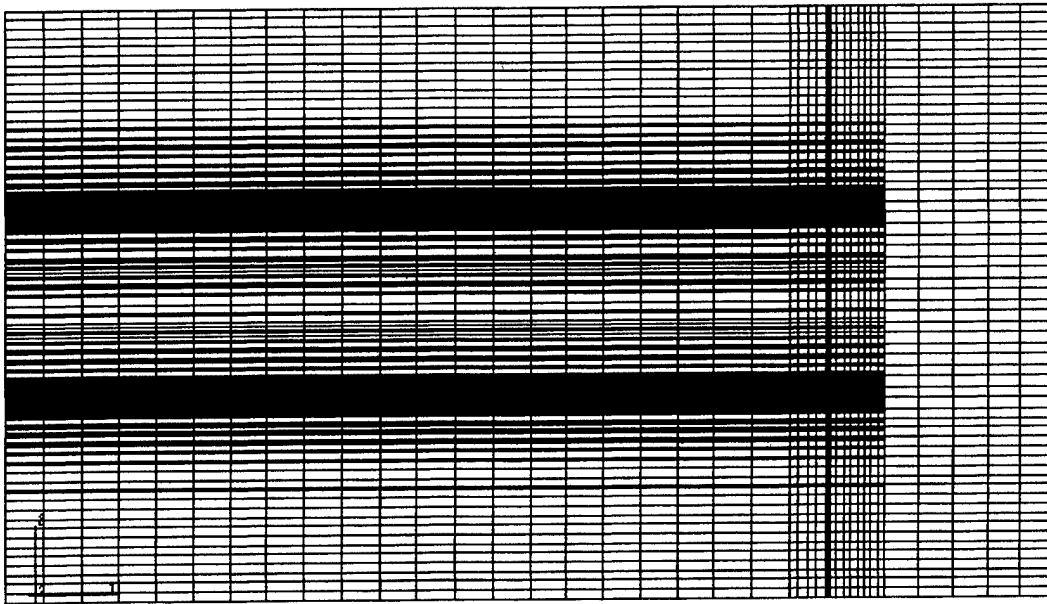
FIGURE 4-5. TOP VIEW OF 3D FE MODEL OF SKIN-STRINGER GEOMETRY
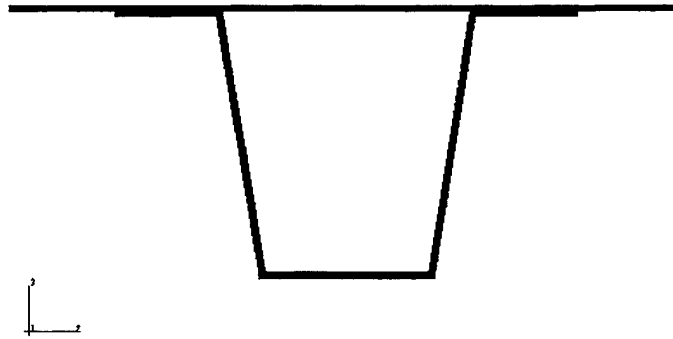
FIGURE 4-6. FRONT VIEW OF 3D FE MODEL OF SKIN-STRINGER SPECIMEN
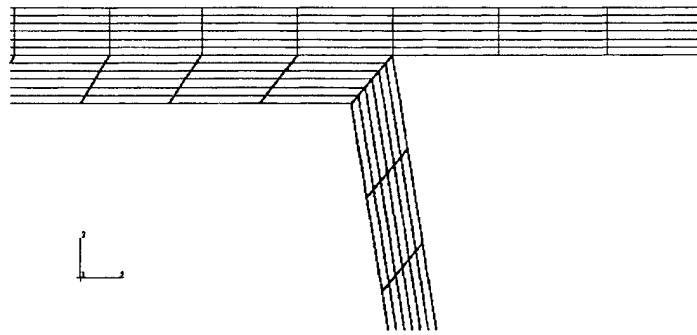
FIGURE 4-7. LOCALLY ENLARGED FRONT VIEW OF 3D FE MODEL OF SKIN-STRINGER SPECIMEN

4.2.2 Results.

Figures 4-8 through 4-11 present comparisons between the mode I, II, III and total ERRs, respectively, for a $[\mp 45/0]_s/d/[\mp 45/0]_s$ layup. That is, for the results of these figures, both the hat-stiffener and sheet regions are six plies thick and the delamination is between two -45° plies. The coordinate system used for this ply designation is that shown in figure 4-3, and conventional notation of a +θ ply being defined by a counter-clockwise rotation about the z axis is adopted. It may be noted that if the z axis were to point in the other direction, i.e., with positive z facing from the sheet towards the hat, this layup would be designated as $[\pm 45/0]_s/d/[\pm 45/0]_s$.

In figures 4-8 through 4-11, the normalized width location used for the horizontal axes is defined so the left edge of the model is at 0.0 and the right edge is at 1.0. It may be noted from the end view of the panel presented in figure 4-1 that the left stiffener flange begins at a distance of 15.88 mm (0.625″) from the edge of the panel; thus, the normalized location is 15.88/101.6 = 0.1563. The left delamination, therefore, spans normalized locations 0.1563 to 0.3125 (actual location is between 15.88 and 31.75 mm) and the right delamination spans normalized locations 0.6875 to 0.8438 (actual location is between 69.85 and 85.725 mm). The ERRs presented in the

figures are at the center of the element used for their calculation. As mentioned in section 3, because the delamination is at the mid-plane of a symmetric region, both Ω_{SF} and Ω_{NSF} are zero for this case. The ERRs in these figures were computed following the same procedures described in section 3.
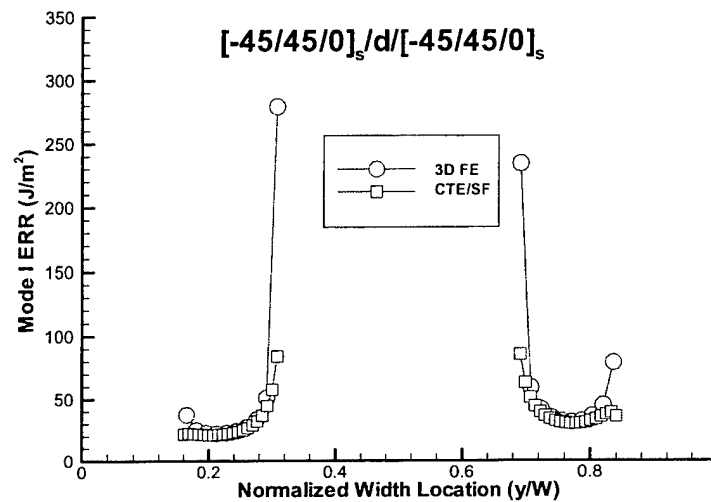
FIGURE 4-8. COMPARISON OF MODE I ERRs FOR A [∓45/0]$_s$/d/[∓45/0]$_s$
HAT-STIFFENED PANEL

FIGURE 4-9. COMPARISON OF MODE II ERRs FOR A [∓45/0]$_s$/d/[∓45/0]$_s$
HAT-STIFFENED PANEL

FIGURE 4-10. COMPARISON OF MODE III ERRs FOR A $[\mp45/0]_s/d/[\mp45/0]_s$
HAT-STIFFENED PANEL

FIGURE 4-11. COMPARISON OF TOTAL ERRs FOR A $[\mp45/0]_s/d/[\mp45/0]_s$
HAT-STIFFENED PANEL

It is observed that, across most of the delamination front, the CTE and the 3D FE results coincide quite closely. The two exceptions are the predictions for all ERR components at the inner corners of the hat regions and for G_{III} along the right delamination front. With respect to the former issue, the ERR at this location is strongly influenced by the vertical section of the hat-stiffener (cf. figure 4-7), and it is unlikely that any plate-based procedure that models mid-plane response would be able to capture this. In fact, there will be a large variation in ERRs predicted by different 3D FE models in this corner region; thus, predictions will be quite sensitive to the local details of the mesh. However, the difference between the CTE and 3D FE results are limited to approximately one element, i.e., a physical distance of approximately 0.8 mm (0.03"). Such a discrepancy would not significantly affect delamination growth predictions in practical situations. Indeed, due to the sensitivity of the predicted ERR on the mesh, it might be appropriate to ignore this value, regardless of whether the analysis were performed by 3D FE or the crack tip element analysis.

The other area of discrepancy between the two methods is the predicted value of G_{III} along the right delamination front. The difference, shown in figure 4-10, is actually the largest that has been observed for any of the practical hat-stiffened panel layups examined to date [39]. Although the CTE predictions for G_{III} are somewhat large, the predictions for G_{II} along this right delamination are somewhat low. Thus, the combination of $G_{II} + G_{III}$ for the CTE model is within a few percent of the 3D FE model. As described in section 3.4, when both mode II and mode III ERRs are present the practical method being adopted to predict delamination growth is to combine them into a G_S, or shear mode. Thus, it is the total quantity $G_{II} + G_{III}$ that is of most importance, and this is quite accurate by the CTE analysis. This is evidenced by the excellent correlation of 3D FE and CTE results for G_I and for total ERR presented in figures 4-8 and 4-11, respectively.

Figures 4-12 through 4-15 present comparisons between the mode I, II, III and total ERRs, respectively, for a $[0]_6/d/[0/\pm45]_s$ layup. That is, the layup is chosen such that, both the hat-stiffener and sheet regions are again six plies thick, but the hat-stiffener is comprised of all 0° plies and the sheet region has a $[0/\pm45]_s$ layup. The delamination is bounded by 0° plies. For this CTE/SF analysis, a 2D plane strain FE model was constructed to obtain $\Omega_{SF} = -1.81°$, with the hat stiffener modeled in the upper region (i.e., following the coordinate system definition of figure 4-3).

Figures 4-12 through 4-15 indicate outstanding correlation between the CTE and 3D FE predictions for all ERR components. Once again, the only exception is in the inner corner regions, which has little practical implication. The correlation evidenced in these figures is similar to what has been observed in various permutations of hat-stiffener and sheet regions comprised of 0°, 45°, -45°, and 90° plies of various materials [39].
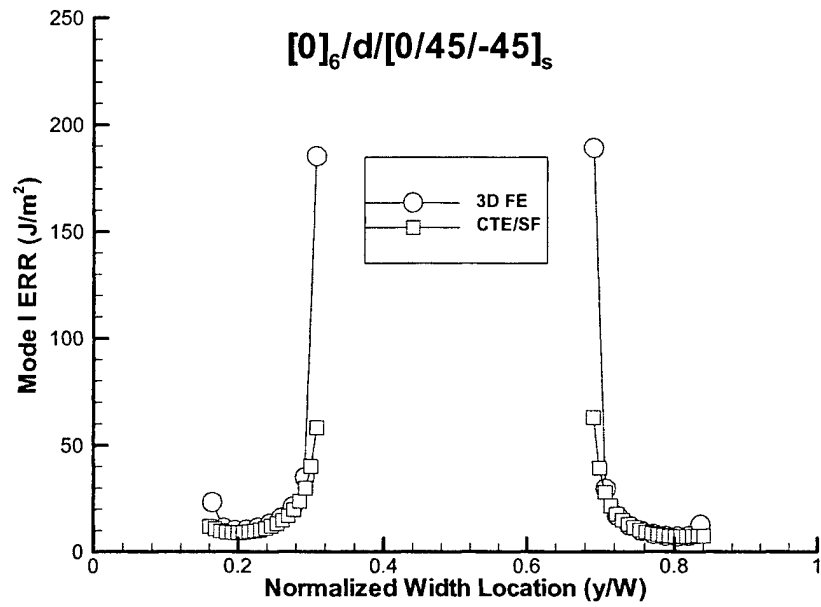
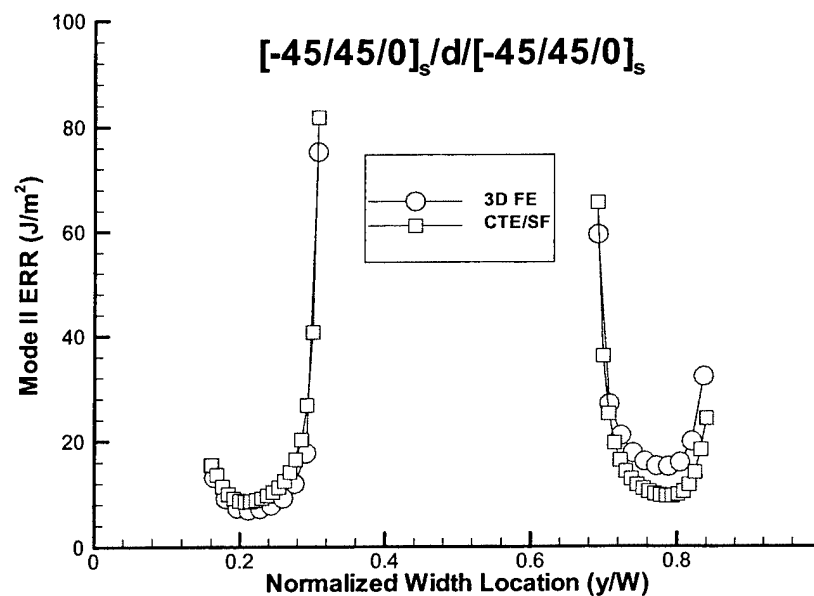FIGURE 4-12. COMPARISON OF MODE I ERRs FOR A $[0]_6/d/[0/\pm45]_s$
HAT-STIFFENED PANEL
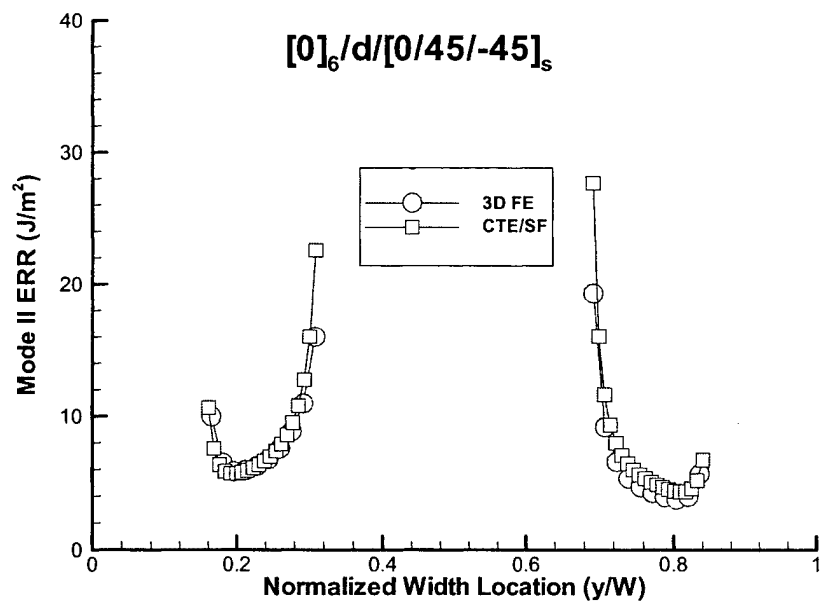
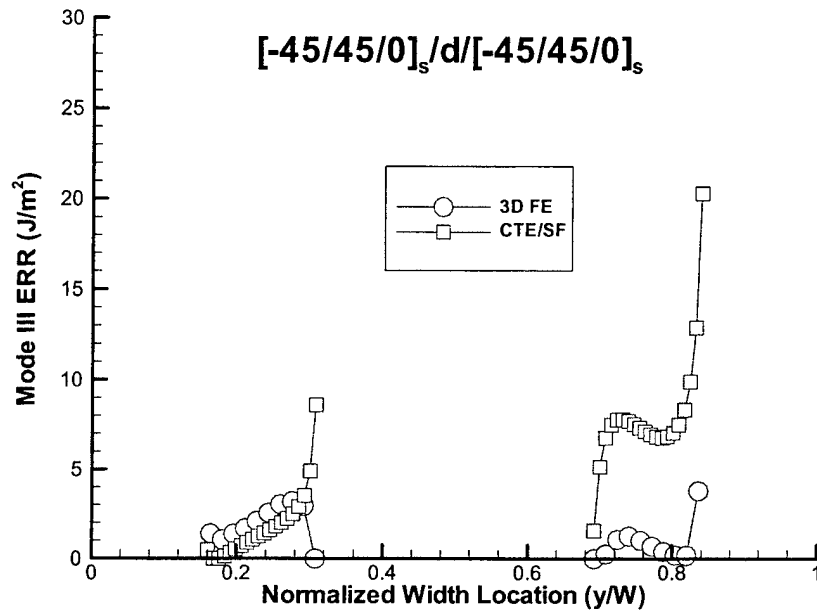FIGURE 4-13. COMPARISON OF MODE II ERRs FOR A $[0]_6/d/[0/\pm45]_s$
HAT-STIFFENED PANEL
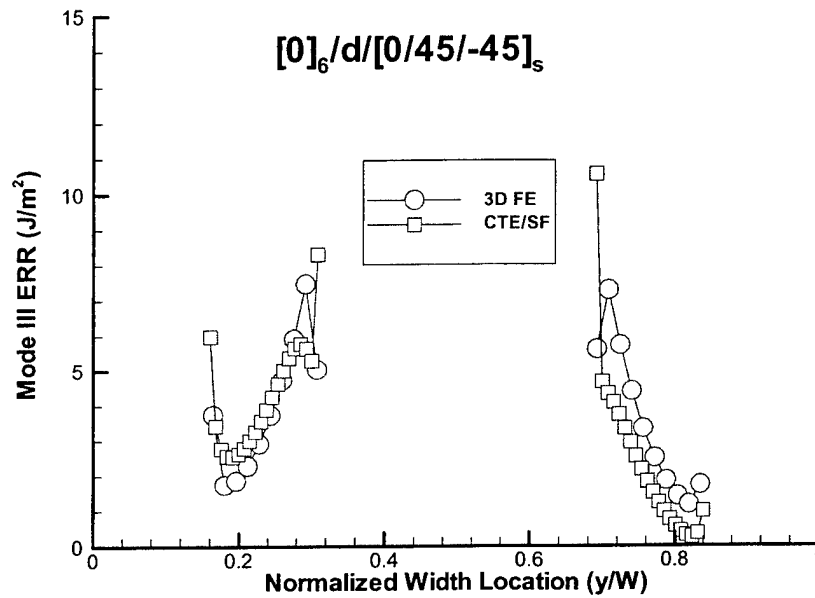
FIGURE 4-14. COMPARISON OF MODE III ERRs FOR A $[0]_6/d/[0/\pm45]_s$
HAT-STIFFENED PANEL

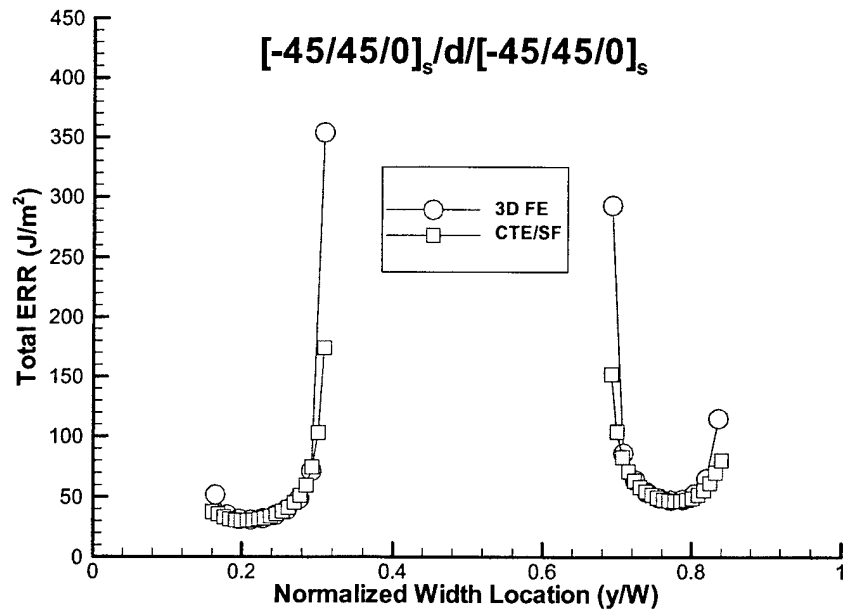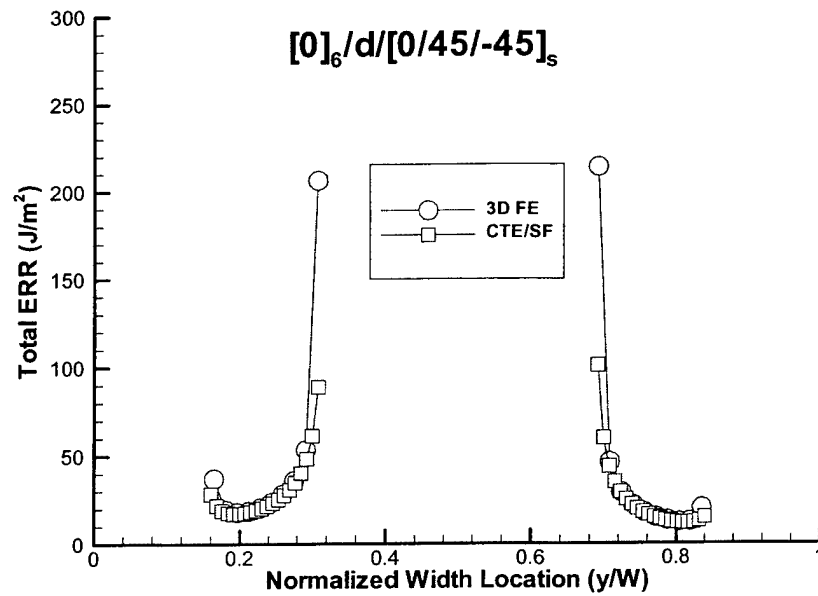FIGURE 4-15. COMPARISON OF TOTAL ERRs FOR A $[0]_6/d/[0/\pm45]_s$
HAT-STIFFENED PANEL

4.3 ASSESSMENT OF THE CTE ANALYSIS.

The above comparisons between FE and CTE predictions for ERR for the skin-stringer geometry show that the CTE analysis is quite accurate for total ERR and singular field-based mode mixity. These comparisons clearly indicate that the 3D CTE formulation is correct and provides an extremely efficient and accurate approach for those materials where a singular field exists. The predictive accuracy of the CTE approach is addressed in the following section.

4.4 EXPERIMENTAL WORK ON C12K/R6376 SKIN-STRINGER GEOMETRIES.

In a previous study, the CTE approach was used to predict delamination growth in two skin-stringer geometries that are typical to aircraft construction [12]. The test specimens were fabricated using the C12K/R6376 graphite/epoxy material system. A bending and a tension-loaded geometry were considered; these geometries and loadings are typical of those found in aircraft applications. For this study, the NSF definition of mode mix was used because it was shown to provide accurate predictions for delamination growth in several polymeric matrix composites. ERR predictions were first obtained for these geometries using the CTE analysis and the NSF definition of mode mix. These results were then used, along with the appropriate toughness versus mode mix data, to make delamination growth predictions. The specimens were then fabricated and tested, and the experimental results were compared to the predictions. Good comparison was obtained between the observed and predicted results [12], which led to the conclusion that the CTE-based approach is an accurate and effective method for predicting delamination growth in practical structural geometries.

5. APPLICATION OF THE CTE APPROACH TO T800H/3900-2 SKIN-STRINGER GEOMETRIES.

5.1 OVERVIEW.

The main emphasis of this study is to assess the predictive capability of the CTE approach for relatively complex composite structural geometries fabricated from an extremely tough next-generation material system. Hence, the CTE/NSF approach was used to predict delamination growth in bending and tension skin-stiffened geometries that are typical of those used in aircraft construction. The T800H/3900-2 graphite/epoxy material system was used, and the dependence of fracture toughness on CTE/NSF-based mode mix was obtained from previous experiments. This section discusses the fabrication and testing of the geometries and presents CTE predictions for delamination initiation for both geometries.

5.2 MATERIAL CONSIDERED.

T800H/3900-2 is an interlayer-toughened graphite/epoxy system. The material is manufactured in two stages [40]. High strength T800H fibers are first coated with a thermoset epoxy resin, and the resulting prepreg tape is then coated with a thermoplastic layer that is in particulate form. Thus, during normal layup and cure, the particulate interlayer melts and flows to form the toughened interface. This material is used extensively by the Boeing Aircraft Company for many structural components in the B777 passenger jet, including skins, stringers, and spars of the horizontal and vertical stabilizer torque boxes, as well as the fuselage floor beams [40].

Material properties for T800H/3900-2 were obtained at the Syracuse University Composite Materials Laboratory (SU-CML) using standard test methods [14]. These results are presented in table 5-1. For this material, the unidirectional flexural modulus, E_{1f}, was taken as the average result from a series of mixed mode bending test results [14]. The values of v_{12} and v_{13} were also measured for this material [14]. However, the value of v_{23} was assumed, based upon a previous study which showed that varying the value of v_{23} within certain physically reasonable bounds did not have any effect on the overall analysis results [41]. The table also gives the single-ply thickness, which was found by averaging the thickness measured from different regions of the manufactured skin-stringer specimens. All the specimens were manufactured from the same batch of material using the same procedure.

TABLE 5-1. UNIDIRECTIONAL MATERIAL PROPERTIES OF T800H/3900-2 GRAPHITE/EPOXY

$E_{11} = 154.72$ GPa	$E_{22} = 7.58$ GPa	$E_{33} = 7.58$ GPa
$G_{12} = 4.14$ GPa	$G_{13} = 4.14$ GPa	$G_{23} = 2.87$ GPa
$v_{12} = 0.32$	$v_{13} = 0.32$	$v_{23} = 0.32$
$E_{1f} = 143.41$ GPa	Single-ply thickness = 0.174 mm	

5.3 CTE/NSF-BASED FRACTURE TOUGHNESS CURVE FOR T800H/3900-2 MATERIAL.

Figure 5-1 presents the fracture toughness curve for T800H/3900-2 as defined by the CTE/NSF approach [12]. These fracture toughness results were obtained from tests of unidirectional

double cantilever beam (DCB), symmetric single-leg bending (SSLB), end-notched flexure (ENF), and mixed mode bending (MMB) specimens with mid-plane delaminations. As indicated in the figure, two different batches of material were used. The individual data points in the figure represent the mean toughness values obtained from several tests on a particular test configuration. The error bars for each data point represent the standard deviations. The standard deviation (SD) for the SSLB tests was computed from the pooled batch 1 and batch 2 data, therefore, the SD line is centered at the mean toughness of the pooled data. Similarly, the SD for mode II was calculated from the pooled ENF batch 1, ENF batch 2, and MMB batch 1 data, and the SD line is centered at the mean toughness of the pooled data.
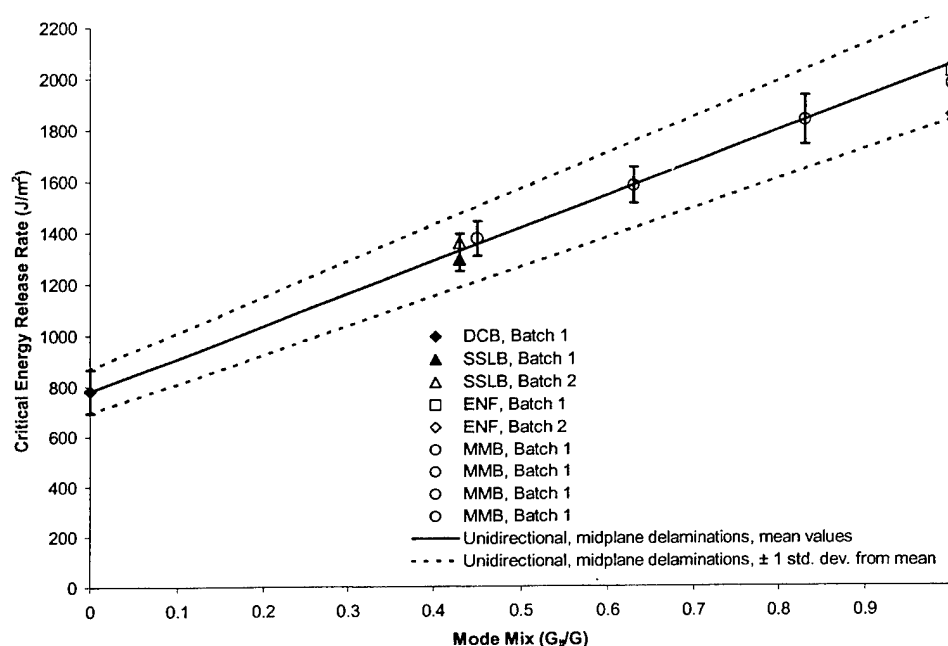
FIGURE 5-1. NSF BASIC FRACTURE TOUGHNESS CURVE FOR T800H/3900-2
GRAPHITE/EPOXY

In figure 5-1, the lower dotted line is constructed by connecting the bottoms of the SD lines of the mode I (DCB) and mode II (pooled ENF and MMB) toughness data. The upper dotted line connects the top of the SD lines of the mode I (DCB) data and the SSLB data and then projecting this line to $G_{II}/G = 1.0$. The solid line is then obtained as the mean line between the two dotted lines, and it is given by the nominal toughness expression in equation 5-1. Equation 5-1 also presents expressions that represent the dotted SD lines.

Nominal toughness (J/m^2) $G_C = 1265.96(G_{II}/G) + 781.74$

Nominal -1 Std. Dev. (J/m^2) $G_C = 1134.88(G_{II}/G) + 695.55$ (5-1)

Nominal $+1$ Std. Dev. (J/m^2) $G_C = 1397.06(G_{II}/G) + 867.94$

As may be observed from figure 5-1 and equation 5-1, for this material, linear expressions work quite well to completely describe the basic toughness data obtained from unidirectional specimens with mid-plane delaminations.

5.4 GEOMETRIES CONSIDERED.

For the tests performed in this report, two skin-stringer configurations were considered. Both of these were comprised of the same basic hat-stiffener cross-section as shown in figure 4-6. Both configurations were composed of six plies in the sheet region and six plies in the stiffener. Both used a [∓45/0]$_s$/d/[∓45/0]$_s$ layup according to the ply orientation definition given in section 4. It is pointed out that the ∓45 sequence is used, as opposed to ±45, simply due to the difference between coordinate systems used during manufacture and analysis. That is, when this part was manufactured (described in section 5.5), the sheet portion was fabricated first and the natural coordinate system to adopt was with the *z axis* facing upwards. In this coordinate system, the layup would be specified as [±45/0]$_s$/d/[±45/0]$_s$. However, for analysis purposes, the coordinate system of figure 4-3 was adopted, which has the z axis pointing downwards, which changes the orientation to the ∓45 sequence.

The first configuration considered was the bending geometry described in section 4.2 and shown in figures 4-1 and 4-2. A total of five specimens were tested, and all of them had a span length of 127 mm (5.0″) and a crack length of 19.0 mm (0.75″). The test fixture had two fixed lower support pins mounted at different vertical heights, so that the upper sheet portion of the specimen was initially horizontal. The upper loading pin was mounted on a bearing arrangement, which allowed for slight rotations about the x axis (axis parallel to the specimen's length) and therefore provided symmetric loading with relation to the width-centerline of the specimen. The loading pin was centered along the length between the two lower support pins.

The second skin-stringer configuration considered was loaded in tension. Figure 5-2 presents the geometry, and figure 5-3 presents the loading arrangement for this specimen. As seen from figure 5-2, the sheet region had a total length of 368.3 mm (14.5″). The hat-stiffener was 101.6 mm (4.0″) long with a 25.4 mm (1.0″) pre-implanted teflon delamination. A length of 76.2 mm (3.0″) on both ends of the sheet was provided for the grips. On the delamination side, there was a length of 76.2 mm (3.0″) between the end of the grip and the hat-stiffener; on the uncracked side, this dimension was 38.1 mm (1.5″). As shown in figure 5-2, each specimen had two 9.65-mm (0.38″) -diameter holes drilled in the center of the shaded regions. The end view of this geometry appeared identical to that shown in figure 4-1, i.e., the sheet was 101.6 mm (4.0″) wide and the hat-stiffener was 38.1 mm (1.5″) wide at its base, 35.4 mm (1.0″) wide at its top, and 38.1 mm (1.5″) tall. The stringer's flanges were each 15.88 mm (0.625″) wide. A total of five specimens were tested in the tension configuration.

Figure 5-3 shows the loading arrangement for the tension specimen. The specimen was placed vertically such that the shaded region in figure 5-2 was positioned within the upper or lower grip. Each grip was 102 mm high and 160 mm wide, with the center 120 mm width serrated. These serrations were oriented to grip or bite under tension loads. Each grip contained a centrally located hole that aligns with the hole drilled in the specimen. The grip also had two holes on either side separated by a 140 mm width, so that the specimen width can fit between them. Five bolts pass through the aligned holes to compress the specimen between the grips. Trial tests showed that it was necessary to have the center hole passing through the specimen in order to redistribute the clamping force to the center of the grip region and reduce the bowing that

occurred from tightening the outer clamping bolts. The grips are attached to "grip support plates," which are essentially a two-post, matched die set to ensure alignment of the loading fixture. The grip support plates are guided by cylindrical alignment rails that limit the loading to pure tensile or compressive loads. Each of the support plates attaches to the load frame; one support plate to the actuator and the other to the load cell.
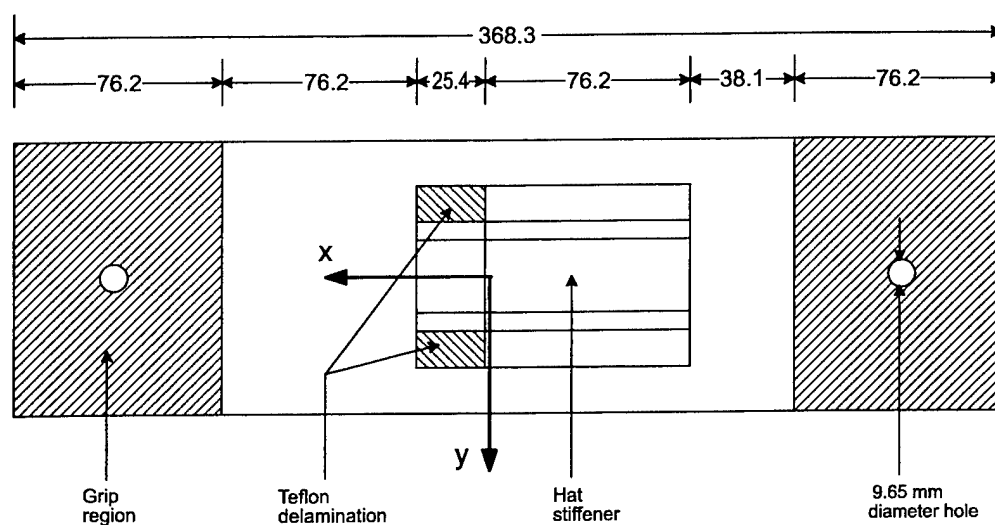
FIGURE 5-2. SKIN-STRINGER GEOMETRY FOR TENSION SPECIMEN
(All dimensions in mm)
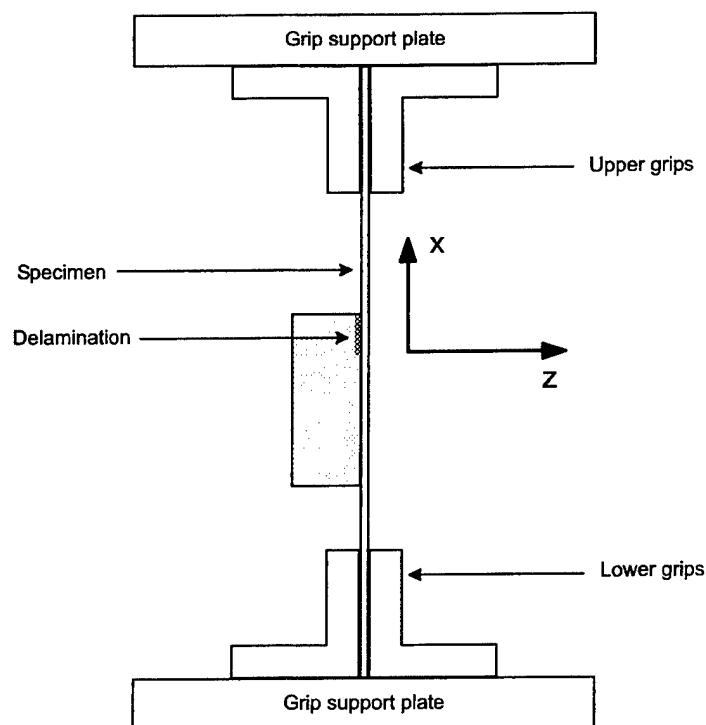
FIGURE 5-3. CONFIGURATION FOR TENSION LOADING

5.5 SPECIMEN FABRICATION.

All the skin-stringer specimens were manufactured using the T800H/3900-2 material. Figures 5-4 and 5-5 present the front view and top view, respectively, of the manufacturing procedure for a typical hat-stiffened panel. Two specimens of the same geometry were fabricated simultaneously using one continuous skin, which was later cut. First, all the plies were cut according to the desired dimensions. The first six plies that comprised the flat sheet portion were placed on a teflon-coated caul plate according to the desired ply orientations. Next, two aluminum mandrels, wrapped with teflon release film, were placed on top of the sheet so they were parallel to each other and separated by a sufficient distance to achieve the desired width of 101.6 mm (4") in each specimen. The mandrels were machined to have the desired inner dimensions of the hat-stiffeners. The pre-implanted delamination was created using a piece of teflon that was 13 μm thick. The teflon was cut in the shape of a rectangular strip that was long enough to cover the full width of the sheet and wide enough to create the delamination length (approximately 6 mm for the bending specimens and 25 mm for the tension specimens) in the hat-stiffened structure. This was then placed at the appropriate location to pass underneath the ends of the mandrels. The six plies that comprised the hat-stiffener were then laid over the sheet and mandrels. Each ply was laid up from the desired starting location on the sheet region (between the two mandrels) and conforming it to the sheet and mandrel. Since the plies were laid on top of each other and had to conform to the hat shape, it was not practical to cut the plies so that their outer edges would also end at the same exact location. Thus, each ply was cut slightly wider than the width needed for the exact hat-stiffener shape.
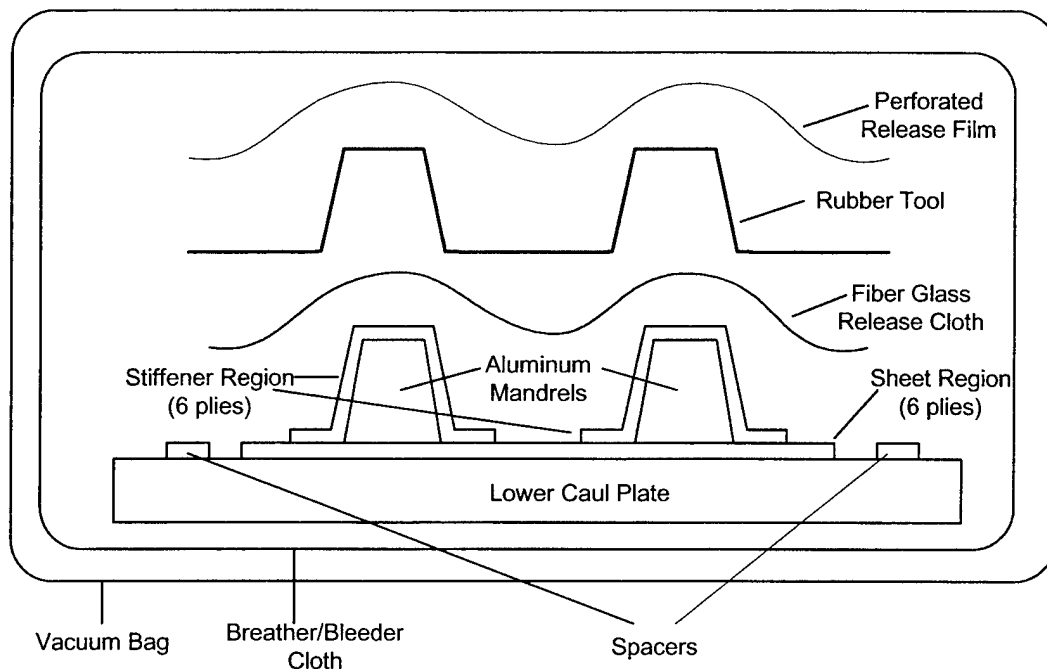
FIGURE 5-4. FRONT VIEW OF MANUFACTURING PROCEDURE FOR A HAT-STIFFENED PANEL
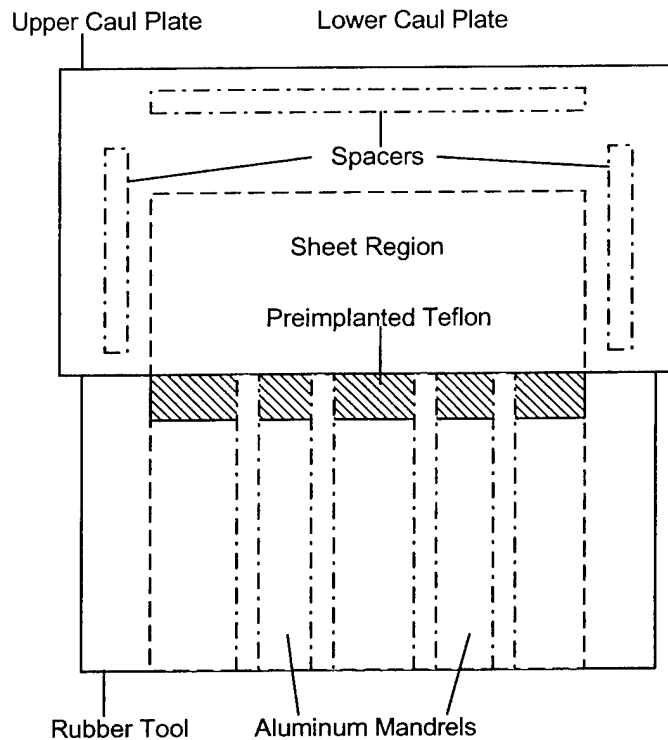
FIGURE 5-5. TOP VIEW OF MANUFACTURING PROCEDURE FOR A
HAT-STIFFENED PANEL

During layup, a 0.8-mm-thick piece of teflon (cutting guard) was temporarily placed on the sheet next to the outer edges of the mandrels. The outer edges of each ply that comprised the hat-stiffener were built up on this thick teflon piece. After two plies were laid up, a sharp razor was used to trim the extra width, thereby having the plies end at the precisely desired location. The cutting guard protects the sheet portion from being accidentally cut while trimming the hat-stiffener layers. This was repeated until all six plies of the hat-stiffener were laid down. Next, the cutting guard was removed and the hat-stiffener plies were pressed down to adhere to the sheet portion. The entire part was then covered with a layer of release cloth. A high-temperature rubber tool was placed on the hat-stiffener portion to conform to the shape of the mandrels. Upper aluminum caul plates covered the rest of the unstiffened sheet regions. Spacers 1.04 mm thick were placed beneath these upper caul plates, along the edges of the sheet region, to maintain uniform thickness in the cured sheet portion. The entire assembly was then covered with breather/bleeder cloth, vacuum bagged, and cured in an autoclave following the manufacturer's recommended cycle. After cure, the part was cut along the sheet region into two specimens, and all edges were trimmed to achieve the desired dimensions. Specimens were cut using a 2.5-mm-thick diamond blade rotating at 1400 rpm.

5.6 CTE MODELS AND PREDICTIONS.

In this section, an FE mesh is first developed for the CTE analyses of the skin-stringer specimens. This mesh uses triangular elements in the vicinity of the crack tip, rather than the

rectangular elements used in the CTE double-plate model presented in section 4. The modified mesh with triangular elements was required for the purpose of modeling a smooth advanced delamination front. To establish the accuracy of this meshing method, a comparative study using both meshes (rectangular and triangular) was conducted for the bending case. The ERR predictions obtained from both meshes were compared in order to establish that the modified mesh provided accurate predictions. Note that, as discussed in section 4, the mesh with rectangular elements was previously verified against 3D FE results. Once the accuracy of the triangular FE mesh was established, the ERR predictions for the bending specimen were used with the CTE/NSF approach to obtain delamination growth predictions. The triangular mesh was also used to obtain ERRs and delamination growth predictions for the tension specimen.

5.6.1 Mesh Refinement Studies for the Bending Specimen.

The CTE double-plate finite element model developed for the bending specimen was essentially similar to that described in section 4. The mesh shown in figure 4-4 used rectangular elements in both the sheet and hat region. This mesh was suitable for the case where the delamination front was initially straight (e.g., for a pre-implanted delamination), and this was easily defined as a straight line along the edges of the rectangular elements that define the transition between the cracked and uncracked regions. However, after the specimen is loaded, the delamination is expected to advance in a non-self-similar manner and the delamination front will be curved. This will be shown subsequently. In order to predict the shape of this growing delamination, it was necessary to modify the mesh according to the advanced crack front profile. To model the advanced front using the mesh of figure 4-4, the constraints would be removed from the affected nodes. Since rectangular elements were used, the interface of the advanced region would have a stair-step shape instead of a desired smooth curve, and this would significantly effect the quantitative accuracy of subsequent predictions.

To obtain a relatively smooth delamination front contour, a new mesh containing triangular elements was created. The new mesh was essentially the same as the mesh with rectangular elements, except that, for a certain distance ahead and behind the delamination front in the x direction, the rectangular elements were replaced by triangular elements. In the y direction, the modified region only spanned the width of the flanges. The position of all the nodes remained unchanged compared to the mesh using rectangular elements and the remaining area outside the modified region still consisted of rectangular elements. The modified mesh is shown in figure 5-6. Because the nodes location does not change, the mesh of figure 5-6 is readily used to model the straight delamination front using the method described above. The significant advantage of this mesh over the mesh of figure 4-4 is that it provides a smooth path for modeling increments of delamination growth. With reference to figure 5-6, the advanced region can be modeled by selecting the appropriate diagonal edges of the triangular elements along which the crack front is to be defined. This overcomes the difficulty associated with the stair-stepped nature of the crack front using the mesh of figure 4-4.

0 Direction of Crack

(a)

(b)

0 Inner Edge of
Hat Stiffener
Flange

Delamination
Front

(c)
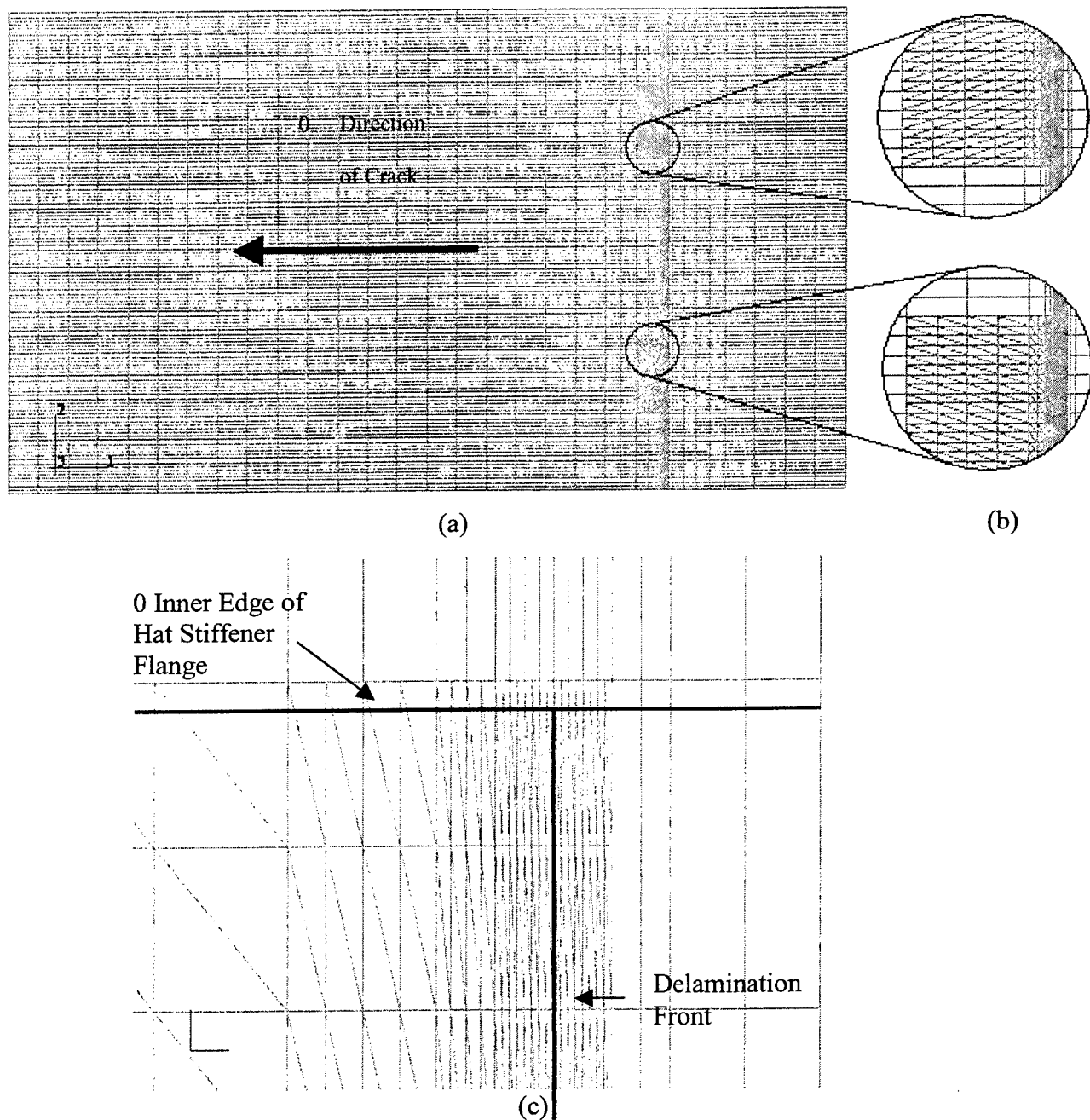
FIGURE 5-6. MODIFIED MESH OF DOUBLE PLATE MODEL USING TRIANGULAR
ELEMENTS: (a) FULL VIEW, (b) MAGNIFIED VIEW OF NEAR TIP REGION,
AND (c) ADDITIONAL MAGNIFICATION OF NEAR TIP REGION

As seen from figure 5-6, the region surrounding the initially straight delamination front of the
bending specimen was meshed with triangular elements. Three-noded elements were used. The
triangular element length at the crack tip, in the direction of crack advance, is 0.0174 mm. All
the triangular elements in this model have a width of 0.397 mm. Note that all the rectangular

5-8

elements had a width of 0.794 mm, i.e., each rectangular element in the region that was modified was replaced by four triangular elements.

The loading, shown in figure 4-2, was achieved by applying specified displacements to the FE model. That is, in the physical experiment, the loading pin forces a constant specified displacement across the width of the mid-span of the specimen. On the other hand, force controlled loading is achieved through a uniformly distributed load along the total width. But this will result in slightly different displacements across the width of the specimen due to the effect of anticlastic curvature and nonuniform flexural rigidity across the width. Thus, to define the location of the loading pin, a nominal vertical (z direction) displacement of 0.127 mm was imposed at all nodes. The vertical reaction forces (obtained from the output file) for the same nodes were summed together to determine the total applied load, which was found to be 51.6 N. Since the ERR varies with the square of the load, the current results can be used to determine the ERR distribution for any value of applied load. Another important point is that, since this is a bending problem, the unidirectional flexural modulus, E_{1f} (cf. table 5-1) was used for analysis. The Abaqus FE input file for the bending analysis is presented in appendix A.

To obtain ERRs from the model with triangular elements, one key issue was the way in which force and moment resultants were determined that belong to the four different regions described in section 3.2. Recall that when the crack tip element equations are applied, plate theory FE output from four different regions are required. These consist of the cracked and uncracked regions of plates 1 and 2. The plate theory in-plane force and moment resultants from each of these regions were used to obtain the ERR using the equations given in section 3. This method was developed and has historically been used for meshes with rectangular elements in the near-tip region. In the case of rectangular elements, the force and moment resultants are obtained at the centroids of the four elements at the crack tip. The resulting local ERR is defined at the common width coordinate defined by the centroids of these four elements.

Because of the nature of the mesh used for the triangular elements (cf. figure 5-6), crack closure cannot be performed with respect to the area of single element at the crack tip. Rather, crack closure must be performed with respect to a rectangular area that is comprised of two triangular elements. When determining the plate theory resultants for each of the four regions described above, one would also prefer to use as much information as possible from those triangular elements immediately adjacent to the delamination front.

To address the issues above, for the meshes that contained triangular elements near the delamination front, force and moment resultants in the required four regions were obtained at each node in the following way. Consider a node along the delamination front that belongs to plate 1. With reference to figure 5-6(c), there are three elements within the uncracked region of plate 1 that are attached to a particular node on the delamination front. The six resultants (three in-plane loads and three moments) from each of these elements were output at that node. For each component of these resultants, the three values (one from each element) were then averaged to obtain the average resultants at that node from the uncracked region of plate 1. For the same node, there are three different elements within the cracked region of plate 1 that are attached to the node. Using the same method, a set of average resultants from the cracked region of plate 1 was obtained at that node. A similar procedure was used for plate 2. The outcome of this

approach is that, for each node in plates 1 and 2 that is associated with a point along the delamination front, resultants are obtained from the cracked and uncracked regions of plates 1 and 2. This produces resultants from the four desired regions, similar to that done for the rectangular mesh, and the crack tip element equations of section 3 can be directly applied.

One could have equally obtained output at the centroidal locations of each of the two triangular elements that create a rectangular region ahead of the delamination front in plate 1 and averaged them to obtain values at the centroid of this rectangle. This would have defined the resultants for the uncracked region of plate 1. Similar procedures could have been used for the other three regions. In this approach, the output from the mesh with the triangular elements would have been fully analogous to that from the mesh with rectangular elements. However, because this method did not lend itself well for use with the curved delamination fronts, it was not evaluated. The drawback of the method that was adopted is that each element produces a set of nodal resultants using an interpolation/extrapolation scheme that is internal to the specific FE postprocessor and is often not apparent to the user. This is inherently based on the output at the elements' Gauss points, which is why different results are obtained for the cracked and uncracked regions of either plate. That is, the resultants obtained by the above method in the uncracked region of plate 1 are representative of some weighted average of all three elements used which are slightly ahead of the delamination front. Similarly, the resultants obtained for the cracked region of plate 1 are representative of some weighted average of all three elements used which are slightly behind the delamination front. However, the weighting of each element's Gauss point values to the nodal resultants may be difficult or even impossible to quantify for certain commercially available FE packages.

To address this new issue, two different methods were considered to go from the nodal point resultants in the four regions to local ERRs. In the first method, local ERRs were computed at each node along the delamination front (referred to as the nodal point method). In the second method, local ERRs were computed at each intermediate point along the delamination front, where an intermediate point is defined as a point midway between each node that defines the delamination front (referred to as the intermediate point method).

a.   Nodal Point Method

For this method, the local area of crack closure was given by a rectangular shape that extended over one element length from the crack tip in the direction of crack advance. In the width direction, for a nodal point that was not on the edge of the model, this local area of crack closure extended one-half of an element width on either side of that node. ERRs for these local areas were calculated directly from the four sets of resultants using the method described in section 3, and the ERR was assumed to be valid for the width location corresponding to the node considered. For an edge node, the local area of crack closure extended over one-half of an element width on one side of the node. Thus, the local area of crack closure for an edge node is offset from that node. The ERRs are obtained in the same manner as above, and are assumed to occur at the mid-location of the local area of crack closure, which is one-fourth of an element width away from the node.

The nodal point method was used to obtain the ERR results at all nodal y locations along the delamination front. These ERR results were then plotted, in width-normalized format, to obtain the ERR distributions across the delamination front. Since the y locations, where the ERR is defined for the nodal point method, are different from those where the predictions were made using rectangular elements, the ERR distributions could not be compared directly. Therefore, the local ERR results by each method were fit with smooth curves and these curve fits were compared visually. This approach indicated that each method of determining ERR distributions (i.e., rectangular elements versus triangular elements and the nodal point method) yielded essentially the same results.

b. Intermediate Point Method

The second method considered to go from the nodal point resultants in the four regions to local ERRs was the intermediate point method. Local ERRs were defined with respect to a different local area of crack closure. This definition was chosen so that a local area of crack closure would correspond to the rectangular area created by two triangular elements and, in the width direction, the local ERR would occur at the center of this rectangle. For this method, a set of midpoint resultants was first computed. For a region that is bounded by two internal nodes (i.e., neither of the bounding nodes are edge nodes), each bounding node contributes one-half of its resultant (the other one-half of a node's resultant is contributed to its other adjacent area). A node along the edge of a plate is assumed to contribute its total resultant to its single adjacent area. These midpoint resultants were then used to obtain local ERRs using the equations given in section 3. In this way, ERR predictions were obtained at all y locations along the delamination front using the mesh of figure 5-6 and were used to plot the ERR distribution. As will be shown subsequently, these results gave excellent comparison to the ERR distribution obtained using the rectangular mesh.

Since both methods gave essentially the same results and both provided good comparison to the predictions from the rectangular mesh (which, recall from section 4, agreed with those obtained by 3D FE results), the choice of which to use was somewhat arbitrary. The intermediate point method was chosen for all subsequent results based solely on ease-of-use. Recall that in the nodal point method, the local ERR for the edge node does not exactly act at that nodal location; hence, some special processing is needed to graph this result. Conversely, for the intermediate point method, the ERR is defined at the center of each rectangular shape and this makes it somewhat easier to use.

A comparison of ERR predictions, by models using the meshes shown in figures 4-4 and 5-6, for a bending specimen for straight delamination front are presented in figures 5-7 through 5-10. The normalized width location used in the figure is the same as that defined in section 4. As in figures 4-8 through 4-11, the region between $0.1563 \leq y/W \leq 0.3125$ comprises the left delamination (i.e., the pre-implanted teflon insert beneath the left flange of the hat-stiffener), and the region from $0.6875 \leq y/W \leq 0.8438$ comprises the right delamination. Both meshes predict the same ERR distribution for the straight delamination front; hence, the modified mesh shown in figure 5-6 will be used for obtaining the subsequent results. Another important observation that can be made about the ERR distributions are their nonsymmetric behavior across the left and

right delamination front. This is because of the effect of bending-twisting coupling and the local effect of the near surface plies. That is, the shape of the ERR distributions are strongly controlled by the additive effects of bending-twisting coupling and the local fiber path for load transfer. The effect of fiber load path may be better understood with reference to figure 5-6, where one looks at the sheet portion of the specimen. The direction of crack advance, as shown, is from right to left, i.e., in the negative x direction. The hat-stiffener is into the page, behind the sheet. Considering that the -45° plies are on the outside surfaces, the orientation of the ply bounding the delamination provides a better direct load path to the right delamination front, and the bending-twisting coupling effect causes the right side of the sheet region to try to attain greater opening deformation. These two combined effects provide a larger ERR along the right delamination front.
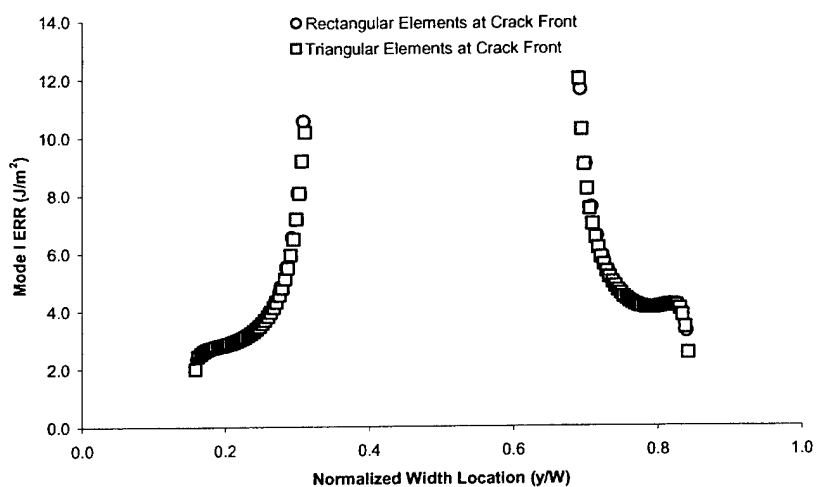
FIGURE 5-7. COMPARISON OF MODE I ERR PREDICTIONS FOR BENDING SPECIMEN
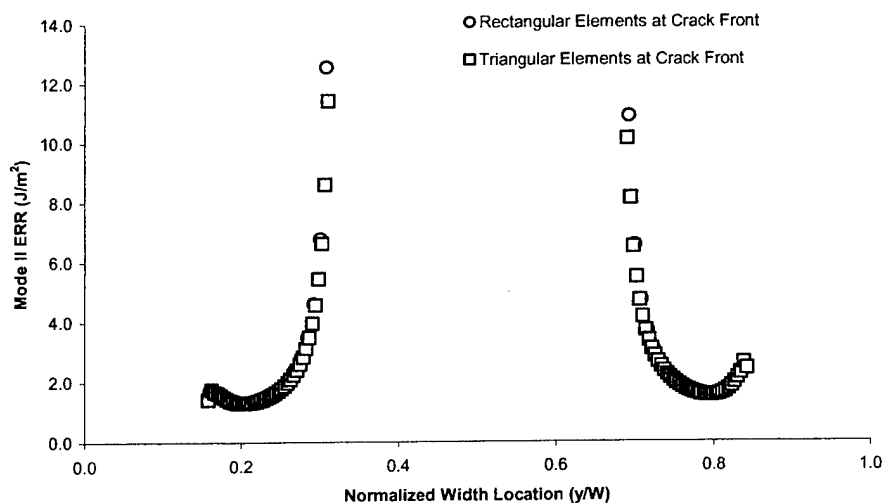
FIGURE 5-8. COMPARISON OF MODE II ERR PREDICTIONS FOR
BENDING SPECIMEN

5-12
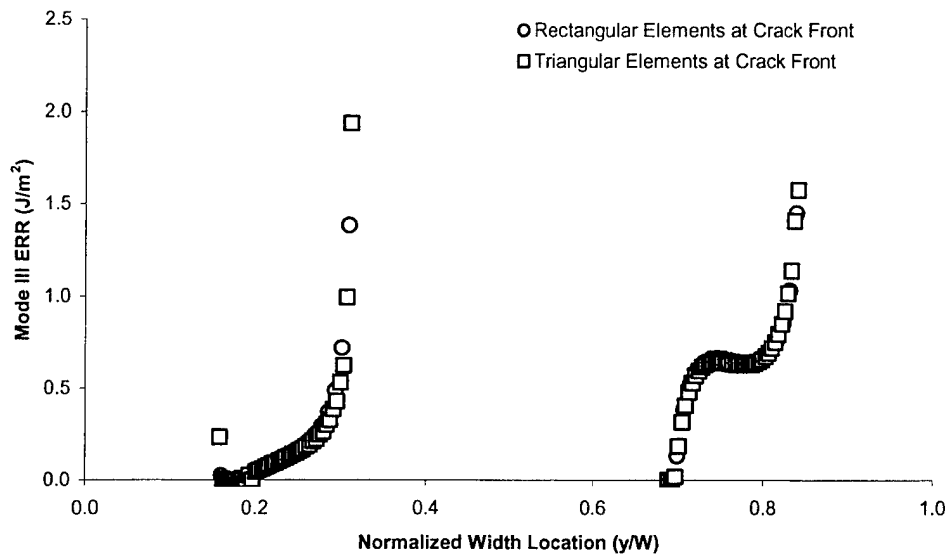
FIGURE 5-9. COMPARISON OF MODE III ERR PREDICTIONS FOR
BENDING SPECIMEN
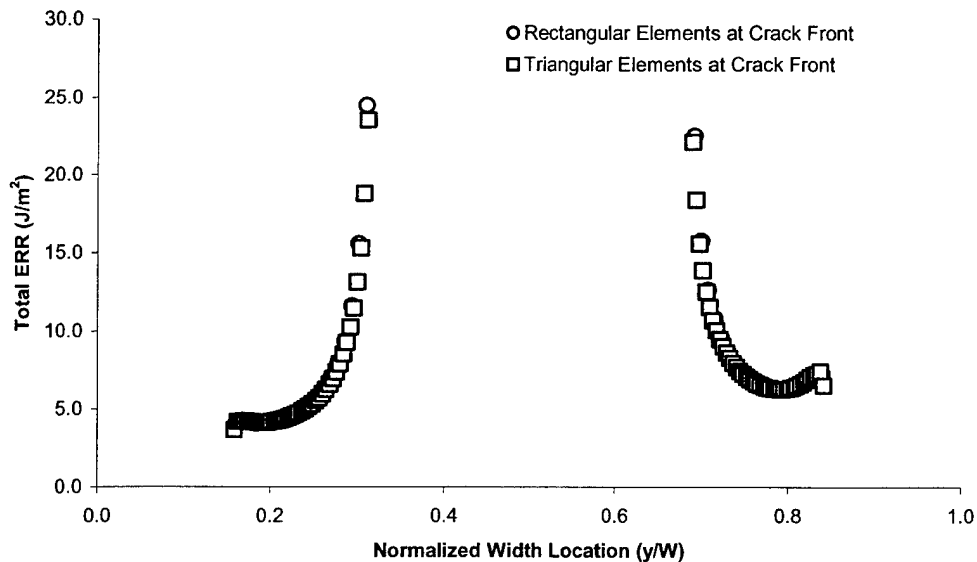
FIGURE 5-10. COMPARISON OF TOTAL ERR PREDICTIONS FOR
BENDING SPECIMEN

5.6.2 Delamination Growth Predictions for Bending Specimen.

This section presents and discusses the procedure for determining the delamination growth predictions for the bending specimens. The ERR predictions presented in the previous section were used to determine the mode mix at each y location, defined as the ratio of the combined mode II and III ERR to the total ERR. Figure 5-11 presents the ratio of the shear ERR, $G_S = G_{II}$

+ G_{III}, to the total ERR versus the normalized width location for the bending specimen. It can be seen from figure 5-11, along with the ERR predictions shown in figures 5-7 through 5-10, that this problem is primarily a mixed mode I-II problem. However, there are small amounts of mode III present, which was combined with G_{II} to give the shear ERR, G_S. For those locations where the mode III component was negative, the G_{III} component was set to zero.
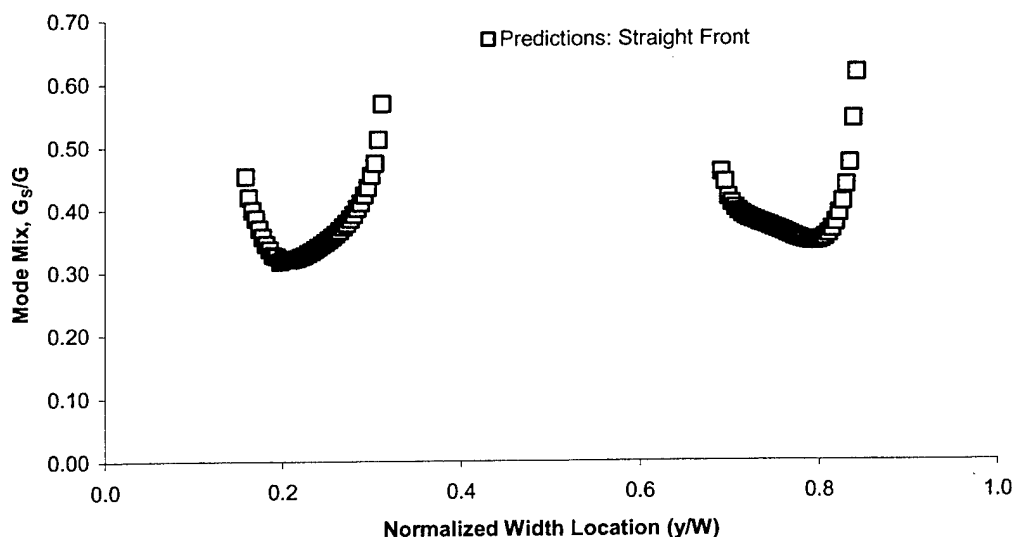
FIGURE 5-11. CTE PREDICTIONS FOR MODE MIX FOR BENDING SPECIMEN

After the mode mix is determined at all y locations along the crack front, the next step is to calculate the loads that will cause the delamination to advance. It is the load results that are essential for predicting the occurrence of delamination growth at any particular location along the crack front. The loads are obtained using the calculated mode mix values and the fracture toughness data for the T800H/3900-2 material presented in section 5.3. The G_S/G value was used instead of G_{II}/G in equation 5-1 to determine the fracture toughness, G_C, at any location along the width. The mean values of the NSF basic fracture toughness curve of figure 5-1, which is the same as the mean toughness expression in equation 5-1, was used for this step. For any location, G is taken from the total ERR distribution of figure 5-10. The value of G_C was obtained from equation 5-1, where the mode mix at any location was obtained from figure 5-11. Since the applied load scales with the square root of total ERR, the load that would initiate delamination at a certain location can be predicted by scaling the applied load of 51.6 N (from the FE results) by the square root of G_C/G at that same location. Figure 5-12 presents the results of the process: the predicted load that will initiate delamination at each location along an initially straight crack front.

Figure 5-12 can be used to make a variety of qualitative and quantitative predictions. First, it can be seen that the loads are low near the inner corners of the hat-stiffener, with the lowest value at the right delamination front. Therefore, delaminations will initially advance along the right delamination front. Further, at any load above the initiation load, the right delamination front (y/W > 0.5) should advance at more locations along the flange width than the left (y/W < 0.5).

Based on the same observation, the entire front of the right delamination should fully advance while the left front still has some undelaminated region. Quantitatively, the predicted loads for delamination initiation are expected to be reasonably accurate; however, accuracy will probably become worse as the delamination advances. The reason for this is that these predictions do not account for the effect of delamination advance on the ERR. That is, the predictions are based upon the initially straight crack front, but as the delamination grows, the delamination front profile is no longer straight. As a result, the ERR distribution changes. Delamination advance modeling and the predictions for advanced delamination fronts will be discussed in the next section. For a design that was supposed to be sized so that no delamination growth occurs, this analysis would be sufficient. Based upon the discussion of section 4.2.2, one might choose to disregard the predictions at the innermost elements. Assuming that there is no error in the ERR predictions, delamination should initiate at the inner corner of the right delamination front at the predicted load of 475 N. This prediction is taken from the square symbol at the third location from the innermost corners of the right front in figure 5-12. The square symbol at the third location from the innermost corner of the left front indicates delamination advance, at this point, will occur at 490 N. Considering the small difference between the predicted initiation load for the left and right fronts (~3%), one would not expect to see any statistical difference in the point of initiation that was observed in experiments, i.e., local effects created by natural variation in the material and/or specimen manufacturing will predominantly influence the initiation point.
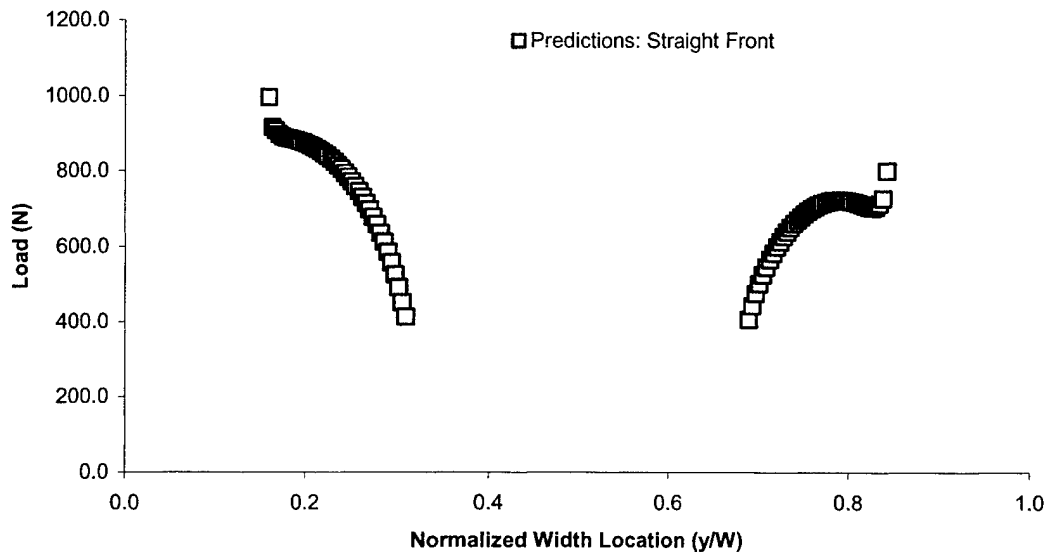
FIGURE 5-12. CTE PREDICTIONS FOR DELAMINATION ADVANCE LOAD FOR BENDING SPECIMEN

5.6.3 Tension Specimens.

The CTE double-plate model of the tension specimens was quite similar to the bending double-plate model in its essential features. However, when comparing figures 5-2 and 5-3 to figures 4-1 and 4-2, the tension model is seen to have a slightly different geometry and loading. The length of the hat-stiffener was only 101.6 mm (4.0"), of which 25.4 mm (1.0") length was

not bonded to the sheet region due to the pre-implanted teflon delamination. Similar to the bending model, the bond between the sheet and the stiffener flanges was modeled by applying the constraint equations (3-1) to all the models within the bonded region. Delaminations were modeled by simply not applying the constraints in the unbonded region. The length of the sheet portion of the tension model was 215.9 mm (8.5″). The 76.2 mm (3.0″) long grip region on either side is not considered in the tension model. The nodes at the end of the model, corresponding to the lower grip, were constrained against displacements in the x and z directions and against all rotations. The nodes at the other end, corresponding to the upper grip were constrained against the displacements in the z direction and against all rotations. In order to prevent rigid body motion, the center nodes at each grip end, i.e., at y = 0, were constrained against displacement in the y direction. The unidirectional tensile modulus, E_{11}, (cf. table 5-1) was used for this model. The model was loaded through force control, such that a total tension load of 34,473 N was uniformly distributed between the nodes at the upper grip end. As mentioned earlier, since the ERR varies with the square of the load, the current results can be used to determine the ERR distribution for any value of applied load. The value of 34,473 N was chosen simply to be in the general range of expected growth.

Initially, a linear analysis was performed and the deformed shape of the model was examined. With reference to figure 5-3 it was observed that the hat-stiffened region of the model displaced in the positive z direction when subjected to tensile load. Due to the high flexural rigidity of the stiffened portion of the panel, this portion would remain essentially straight whereas the unstiffened sheet region would undergo bending to give the deformed shape. This resulted in the physically inadmissible behavior of the positive x (+x) end of the hat-stiffener penetrating through the sheet region.

To prevent the above interpenetration problem, the nodes that define the +x end of the hat-stiffener flanges were constrained to undergo the same z direction displacements as the corresponding nodes (same (x,y) location) in the sheet region. The constraint equations were the same as the last line of equation 3-1. Subsequent linear runs showed that there was no longer any interpenetration, but positive opening displacements still occurred between the sheet and hat in the delaminated region. This behavior agrees with what would be physically expected, indicating that this modification realistically constrained the specimen. Subsequently, this will be referred to as the tension model with constrained interpenetration.

Figures 5-13 through 5-16 present the ERR predictions for the case of a straight delamination front for the tension specimen. It may be observed that the ERR distribution across the left and right delamination fronts are non-symmetric because of the effect of bending-twisting coupling and the fiber load path. Using the same procedure described in section 5.6.2, the ratio of G_S/G was calculated and was used along with equation 5.1 to determine the fracture toughness, G_C, at any location along the width. The predicted delamination load was then determined by scaling the applied load of 34,473 N by the square root of G_C/G at the desired locations. Figures 5-17 and 5-18 present the mode mix distribution and the predicted loads for delamination growth for the straight delamination front. The results of figure 5-17, along with figures 5-13 through 5-16 indicate that the tension-loaded configuration is predominantly a mode II problem with small amounts of G_I and G_{III} present in the regions near the edges of the flanges. The mode mix, G_S/G, for the tension case is very close to 1.0 for the entire width of both delamination fronts, which

resulted in significantly higher toughnesses used for these predictions as compared to the bending case. This is shown in figure 5-18, which shows that the predicted loads are two orders of magnitude than the loads for the bending case. In fact, the peak load values in figure 5-18 were found to be quite close to the predicted first ply failure load for the sheet.

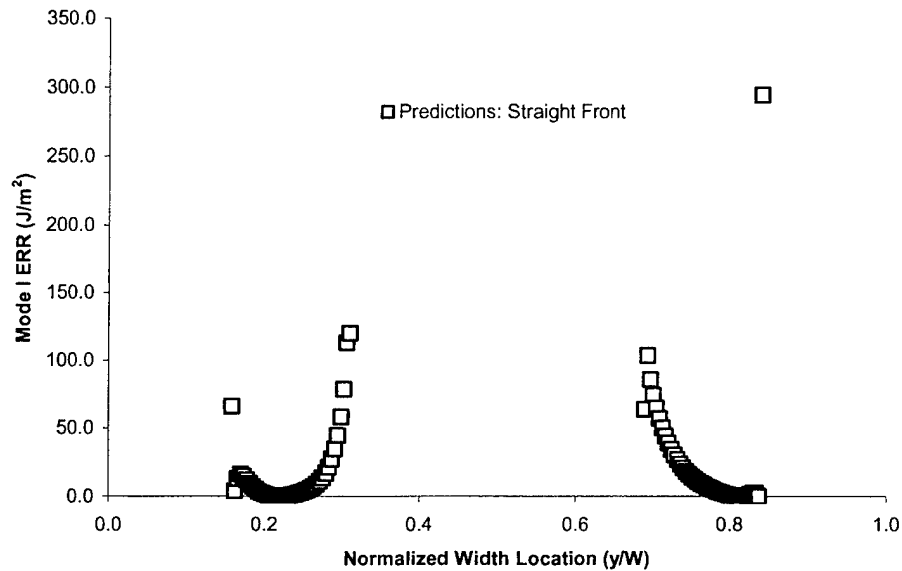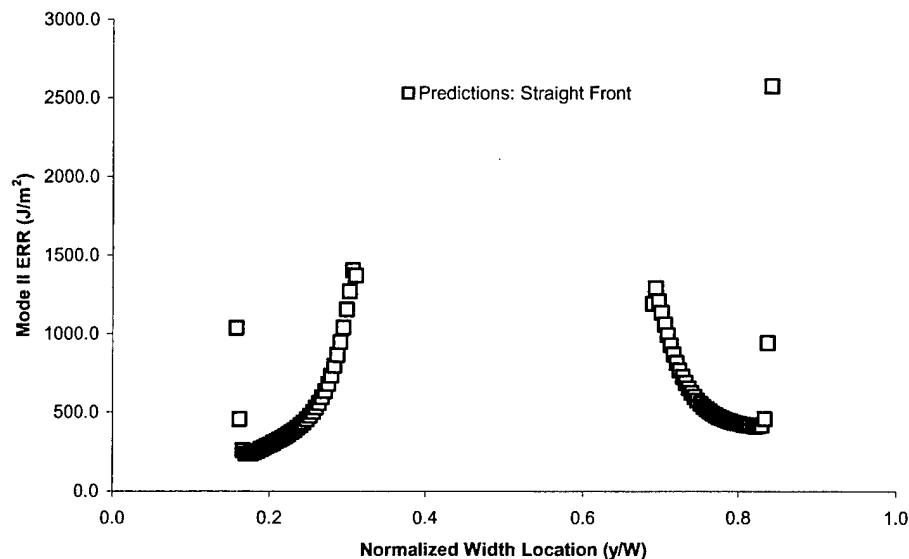FIGURE 5-13. CTE PREDICTIONS FOR MODE I ERR FOR TENSION SPECIMEN

FIGURE 5-14. CTE PREDICTIONS FOR MODE II ERR FOR TENSION SPECIMEN
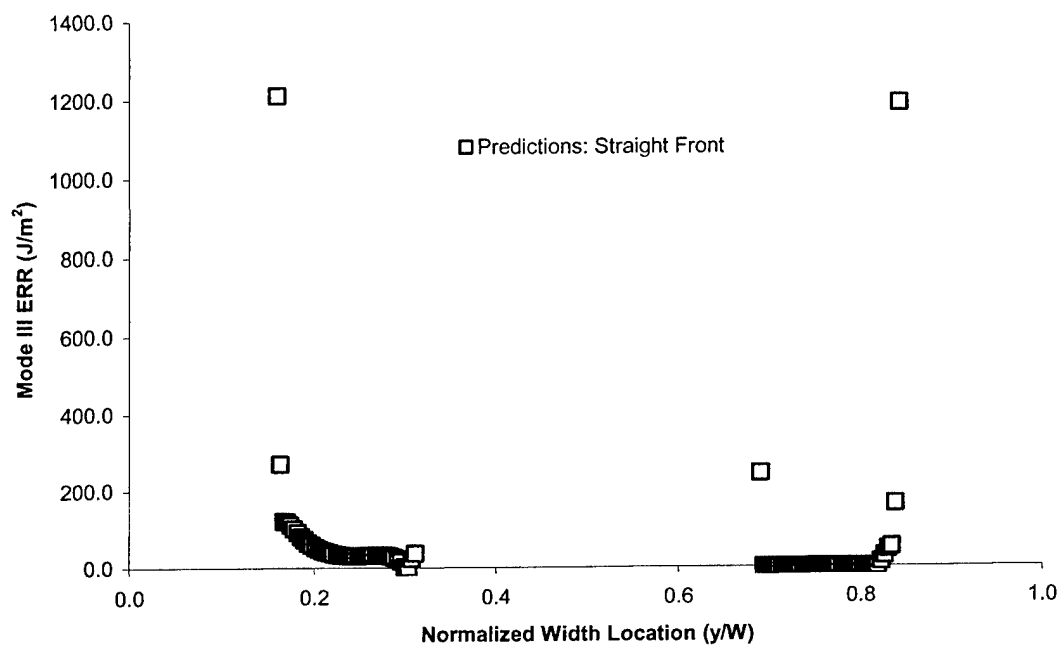
FIGURE 5-15. CTE PREDICTIONS FOR MODE III ERR FOR TENSION SPECIMEN
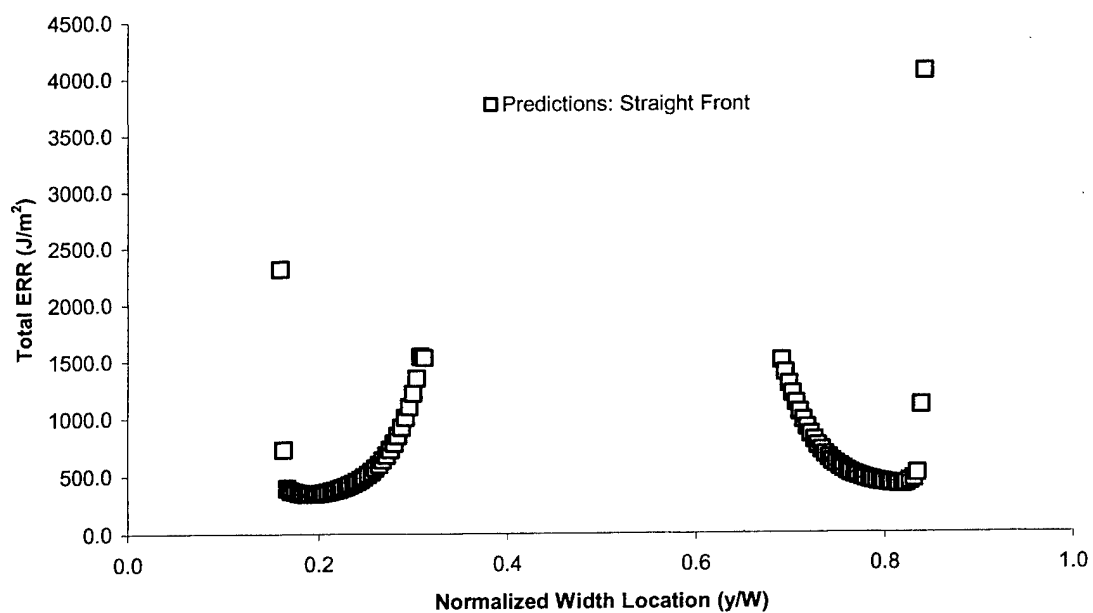

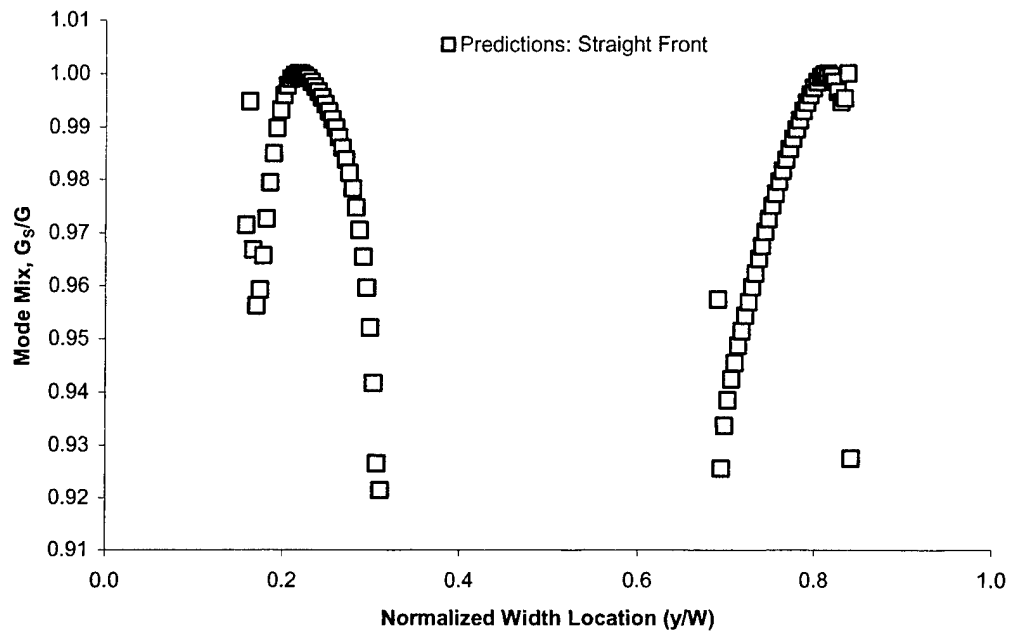FIGURE 5-16. CTE PREDICTIONS FOR TOTAL ERR FOR TENSION SPECIMEN

FIGURE 5-17. CTE PREDICTIONS FOR MODE MIX FOR TENSION SPECIMEN
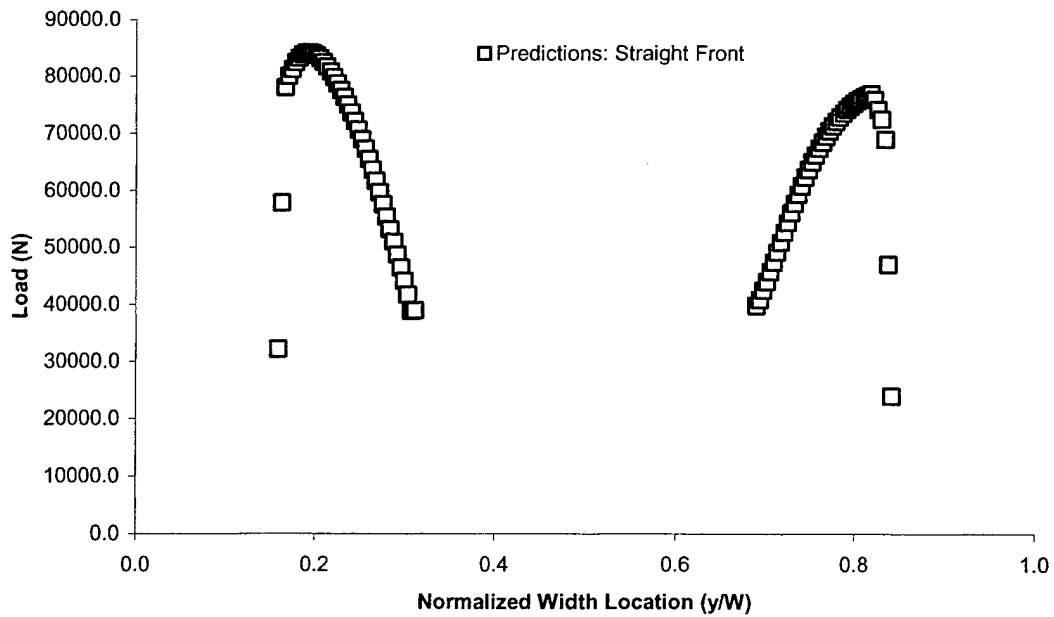
FIGURE 5-18. CTE PREDICTIONS FOR DELAMINATION ADVANCE LOAD FOR
TENSION SPECIMEN

Based on figure 5-18, several predictions can also be made for the tension case. Delamination is predicted to initiate near the inner corner of the left delamination front. At any load, more delamination growth will occur in the right front than in the left front. Furthermore, the right front should show full delamination growth before the left front. Similar to the bending case, the above predictions are expected to be accurate for delamination initiation; as the delamination front profile changes, the accuracy of the initial predictions will decrease. If there were no errors in the ERR predictions, then delamination growth should initiate at the inner corner of the left delamination front at the predicted load of 41,700 N. This can be obtained from the square symbol at the third location from the innermost corners of the left front in figure 5-18. However, the square symbol at the third location from the innermost corner of the right front indicates delamination advance, at this point, will occur at 42,450 N. Considering the small difference between the predicted initiation load for the left and right fronts (~2%), one would not expect to see any statistical difference in the point of initiation that was observed in experiments, i.e., local effects created by natural variation in the material and/or specimen manufacturing will predominantly influence the initiation point.

In addition to the linear analysis, it was necessary to investigate the effect of nonlinear behavior of the tension specimen on the ERR predictions. In the region contacting the stiffener, the centroid of the specimen is not aligned with the loading axis. The applied force therefore produces a moment about the centroidal axis, which results in deflection in the z direction (cf. figure 5-3). Due to the high flexural rigidity of the stiffened portion of the panel, this portion remains essentially straight and the unstiffened sheet region exhibits the majority of the bending behavior. The bending moment is nonlinearly related to the in-plane load; thus it depends on the magnitude of the load and the moment arm. However, the moment arm itself also depends on the magnitude of the load because sufficiently high loads will cause the centroid of the stiffened region to align itself with the loading axis. To study the effect of this behavior on the ERR predictions, a geometrically nonlinear analysis was conducted using the tension model with constrained interpenetration. The maximum load used for this analysis was 34,473 N. Although the linear analysis predicts delamination initiation at approximately 41,700 N, it will be shown that in most specimens that were tested, initiation took place at loads less than 34,473 N. Hence, the maximum load of 34,473 N and several intermediate loads are sufficient for investigating the effects of nonlinear behavior. The Abaqus FE input file for the nonlinear tension analysis is presented in appendix A.

The nonlinear tension CTE analysis was used to obtain ERR distributions at a number of intermediate loads, and these were compared to the linear analysis ERR distributions at the corresponding loads. Figure 5-19 presents the comparisons between the average mode I, II, III and total ERRs versus the square of the applied load for the left delamination front. Here, average ERR is used to denote the value for the full delamination width. This was done to determine whether the nonlinear analysis produced significantly different predictions for the total ERR and the individual components across the entire delamination front. The average ERR values were determined by multiplying each local ERR by its area of crack closure, summing these across the width, and then dividing by the total area. Since all areas of crack closure are identical, the average of any given ERR component can be taken from all locations along the left delamination front at a certain applied load. For instance, the average mode I ERR at any load was obtained by taking the average of the mode I ERR values at each element comprising the left

delamination front. Figure 5-20 presents the same results as figure 5-19 except for the right delamination front. Figures 5-19 and 5-20 indicate that the linear and nonlinear analysis results for average mode II and total ERR are fairly close. For example, the average total ERR for the left front from the nonlinear analysis was 8% higher than that obtained from the linear analysis (i.e., the slope of the nonlinear line in figure 5-19(d) is 8% greater than the slope of the linear line). For the right delamination front, the average total ERR from the nonlinear analysis was 4.6% higher than from the linear analysis. Although the differences in mode I and mode III ERRs between the linear and nonlinear analysis appear large in the figures, their magnitudes are small compared to the mode II and total ERRs, and they only contribute a small amount to the total ERR. The mode I, II, and III ERR components comprise approximately 2%, 96%, and 2% respectively, of the total ERR. Comparisons were also made between the ERR distributions from both analyses at each of the intermediate loads, and the results were very similar.
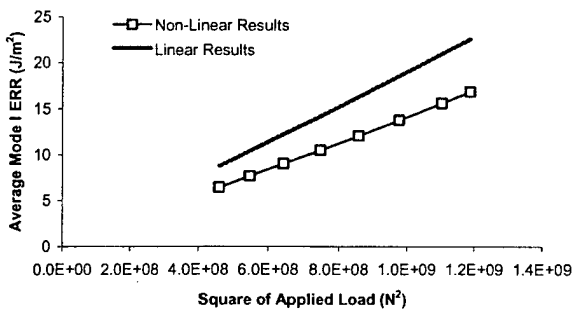
(a)
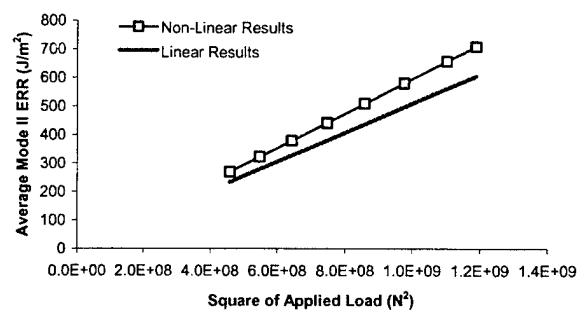
(b)
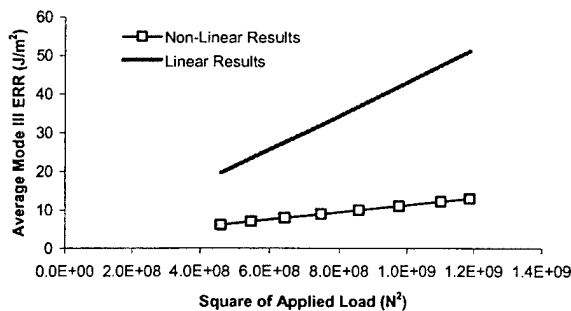
(c)
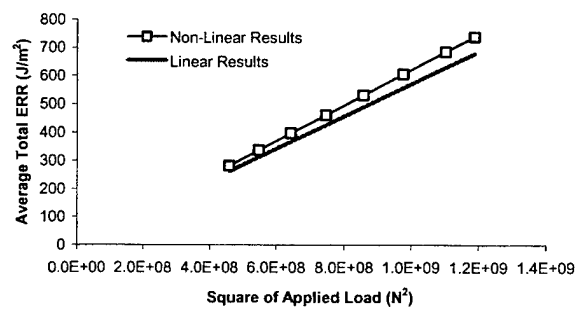
(d)

FIGURE 5-19. COMPARISON OF AVERAGE ERR PREDICTIONS FOR
LEFT DELAMINATION FRONT OF TENSION SPECIMEN: (a) G_I,
(b) G_{II}, (c) G_{III}, AND (d) TOTAL ERR
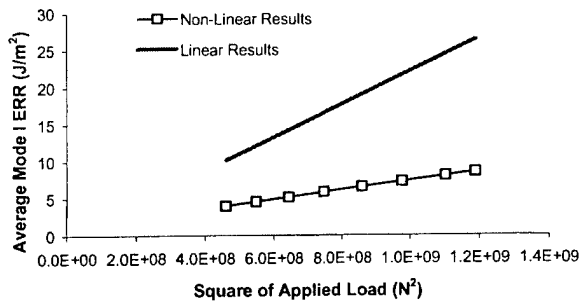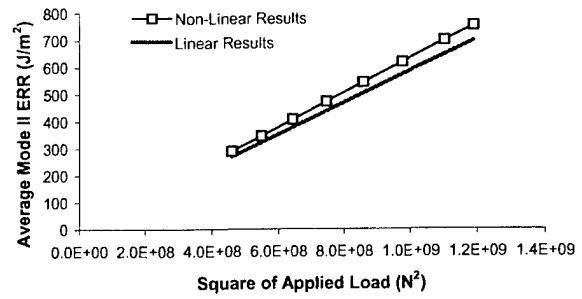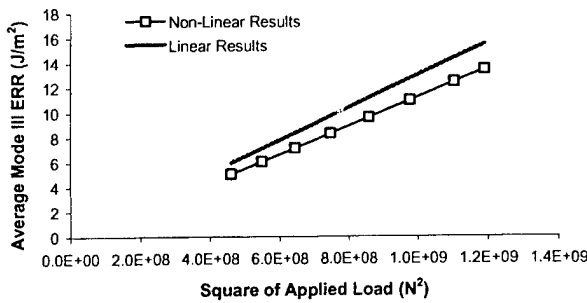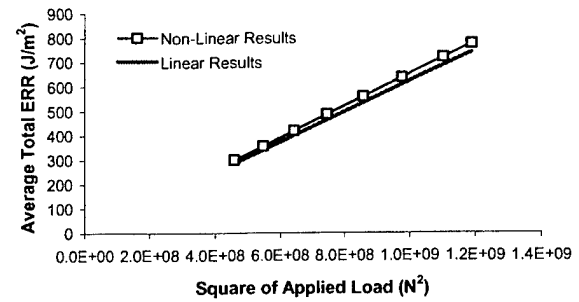
FIGURE 5-20. COMPARISON OF AVERAGE ERR PREDICTIONS FOR
RIGHT DELAMINATION FRONT OF TENSION SPECIMEN: (a) G_I,
(b) G_{II}, (c) G_{III}, AND (d) TOTAL ERR

Table 5-2 presents the predicted delamination loads obtained using the linear and nonlinear analysis for the straight delamination front. The mesh of figure 4-4 was used for these results; hence, the predictions are obtained at 20 locations corresponding to the 20 rectangular elements along each front. The load predictions for the nonlinear analysis were obtained by appropriately scaling the nonlinear ERR predictions at an applied load of 34,473 N. From table 5-2, it can be seen that the percentage difference between the predicted loads from both the analyses is less than 6.5% for all the locations. Hence, it was decided that the linear analysis provides sufficiently accurate results for predicting delamination growth in the tension specimen, and that using the more cumbersome and time-intensive nonlinear analysis was not warranted. This is of particular importance for the curved delamination front results that are described subsequently.

TABLE 5-2. COMPARISON OF PREDICTED DELAMINATION LOADS OBTAINED
USING LINEAR AND NONLINEAR ANALYSES

Normalized Width Location	Linear Predictions (N)	Nonlinear Predictions (N)	% Difference
0.1602	65003	62921	3.2
0.1680	77217	72402	6.2
0.1758	81197	75879	6.5
0.1836	83032	78029	6.0
0.1914	83620	79252	5.2
0.1992	83241	79624	4.3
0.2070	82145	78923	3.9
0.2148	80494	77556	3.6
0.2227	78420	75859	3.3
0.2305	76009	73845	2.8
0.2383	73279	71508	2.4
0.2461	70240	68826	2.0
0.2539	66868	65765	1.6
0.2617	63179	62287	1.4
0.2695	59153	58357	1.3
0.2773	54790	53965	1.5
0.2852	50241	49173	2.1
0.2930	45400	43968	3.2
0.3008	39672	37891	4.5
0.3086	30551	28744	5.9
0.6914	32542	30675	5.7
0.6992	40688	39570	2.7
0.7070	44731	44046	1.5
0.7148	48548	48146	0.8
0.7227	52125	51971	0.3
0.7305	55689	55709	0.0
0.7383	58993	59140	-0.2
0.7461	61993	62227	-0.4
0.7539	64698	64962	-0.4
0.7617	67103	67344	-0.4
0.7695	69195	69371	-0.3
0.7773	70999	71040	-0.1
0.7852	72531	72338	0.3
0.7930	73775	73233	0.7
0.8008	74717	73680	1.4
0.8086	75322	73625	2.3
0.8164	75560	73016	3.4
0.8242	74285	71717	3.5
0.8320	68677	68196	0.7
0.8398	54590	56170	-2.9

6. EXPERIMENTAL PROCEDURE AND RESULTS.

6.1 OVERVIEW.

This section presents the experimental procedure and results obtained from the bending and tension tests conducted on the skin-stringer geometries. The first part of this section describes the experimental procedure for testing and delamination growth inspection. In the second part, a typical sequence of ultrasonic images is shown from some bending and tension specimens. These images depict various stages of delamination advance in the same specimen. Subsequently, these stages will be referred to as events. Finally, the method that was used to interpret these images and extract relevant data will be explained.

6.2 EXPERIMENTAL PROCEDURE.

Both types of tests (bending and tension) were performed on servohydraulic, uniaxial load frames. These included an INSTRON series 1331 88,965 N load frame and an MTS 733,957 N load frame. The INSTRON machine was controlled by a series 8500 digital controller, and the MTS machine was controlled by an MTS Teststar II controller, version 4.0D. The INSTRON machine used a 44,482 N load cell, while the MTS machine used an 88,965 N load cell. The INSTRON load frame was used for the bending tests because the maximum predicted load for this case was approximately 900 N, which was well within the capacity of the load frame. The maximum predicted load for the tension tests was approximately 85,000 N, and the MTS load frame had to be used for these tests. All tests were run in displacement control at a rate of 0.0025 mm/s. A data acquisition system was used to collect and store all test data on a computer. Load and displacement data were collected every 1.11 N for the bending tests, and every 89 N for the tension tests. These increments were chosen based on the magnitude and range of the expected delamination loads (cf. figures 4-9 and 4-15). Delamination growth within each specimen was monitored using an ultrasonic inspection unit (C-scan) that used a 25 MHz transducer in pulse-echo mode; a 100 MHz transient-waveform digitizer was used to collect and relay the transducer data to a personal computer for storage and processing. This is the same technique used for monitoring delamination front profiles in unidirectional and multidirectional end-notched flexure specimens [37 and 42]. Additional details on the nondestructive inspection system are provided in references 43 and 44. For all specimens, this technique was successful in capturing a number of partial growth events, i.e., delamination advance occurring over only a portion of the pre-implanted front. For the two specimen types, the procedures for testing and delamination growth inspection were slightly different and are separately described below.

For the bending case, the untested specimen was first C-scanned to give the initial crack front. The specimen was then placed in the fixture and loaded. Load versus displacement curves were monitored in real time, and the panel was observed closely for any audible cracking sounds. The test was stopped whenever either a cracking sound was heard, or there was a nonlinearity in the load-displacement curve. The maximum load for the test was recorded and the specimen was again scanned to determine whether any delamination growth had occurred. The process of testing and scanning was repeated several times, until a complete history of delamination front profiles versus load was obtained for each specimen.

For the tension case, the loading arrangement was previously described in section 5.4. To setup the tension specimen, the grips with close tolerance holes were first bolted tightly to the support plates. The grips with slotted holes were also bolted to the support plate, although these were left finger tight initially. The specimen was then placed between the grips, as shown in figure 5-3. Next, the five bolts that tighten the grips together were put into place, including the center bolt that passes through the specimen. A level indicator was used to ensure that the specimen was vertical and aligned with the direction of applied load. The bolts were then tightened in a crossing pattern to evenly distribute the clamping force that squeezes the specimen between the grips. Finally, the bolts in the slotted grip holes were tightened to secure them to the support plate. The test procedure was similar to that described above for the bending case. However, for these tests, nonlinearity in the real-time load-displacement curves was mainly due to slipping within the grip regions, and any effect of the delamination growth was not apparent. Thus for these specimens, the test was stopped if a cracking sound was heard or after 2224 N of additional load was applied on the specimen. This load increment was chosen based upon the difference between the predicted delamination loads of adjacent elements along the straight crack front. That is, a load increment of approximately 2224 N was expected to advance delamination by a single-element width along the initial crack front. The same overall procedure described for the bending specimens was used. The tension specimens were C-scanned and tested several times to obtain a complete history of delamination front profiles versus load.

6.3 EXPERIMENTAL RESULTS AND DATA REDUCTION.

This section presents a typical sequence of C-scan images corresponding to a bending and tension specimen. The procedure for interpreting the scans and obtaining relevant data is described. Essentially, the C-scan images for each specimen were examined and certain measurements were made to characterize delamination growth events. The measurements were then used to obtain the experimental results for the bending and tension specimens.

6.3.1 Bending Specimens.

Five bending specimens were tested at a crack length of 19.05 mm (0.75″); these will be referred to as specimens B1-B5. Figure 6-1 presents a sequence of C-scan images and sketches for specimen B1 that is fairly representative of those obtained from all bending specimens. For each C-scan image, the corresponding sketch is shown below it. First, the C-scan images will be discussed, and a discussion of the sketches will follow. The specimens were scanned in so the flat region of the sheet directly faced the transducer and the stiffener was on the other side. The gating for the scans was setup so all the front surface reflections (from the sheet) were neglected. Once gating was setup, scan data was obtained using a time-of-flight scale and amplitude scale. The time-of-flight scale measures the time required for the sound wave to reflect back from a surface. An amplitude scale measures the strength of the reflected signal. Different times of flight and amplitudes are plotted in different colors, thereby showing the internal features of the specimen. For the data presented subsequently, the amplitude scale was chosen because the image was sharper and the shape of the delamination front was more readily distinguishable compared to the time-of-flight scale.

(a)

(19.3, 2.74)   (71.9, 3.6)   (84.7, 2)
(20.32, 3.86)   (31.1, 3.86)   (72.8, 4.75)   (83.6, 4.75)

(b)

(19.3, 2.74)   (31.1, 3.22)   (7? ?, 3.1)   (84.7, 2)
(20.32, 3.86)   (30.5, 3.86)   (73, 4.75)   (83.6, 4.75)

(c)

(19.3, 2.74)   (31, 1.7)   (71.9, 3.1)   (84.6, 2.5)
(20.32, 3.86)   (28.2, 3.86)   (74.93, 4.75)   (83.6, 4.75)

(d)

(19.3, 2.74)   (31.1, 0.058)   (71.73, 0.71)   (84.84, 1.6)
(20.32, 3.86)   (26.29, 3.86)   (78.87, 4.75)   (82.55, 4.75)

(e)

(19.3, 2.74)   (30.73, 0.33)   (73.4, 0.71)   (84.7, 2.1)
(20.32, 3.86)   (24.38, 3.86)   (82.2, 4.5)   (83.82, 4.5)
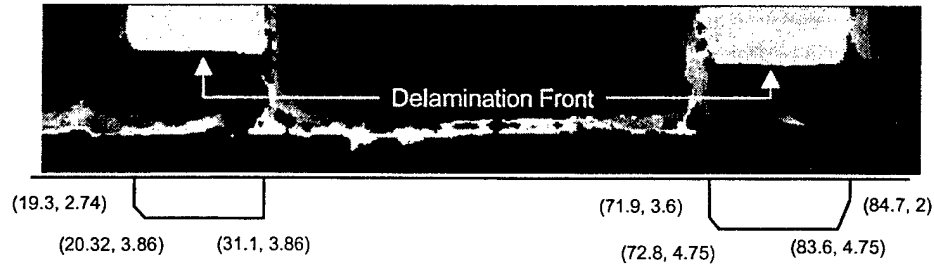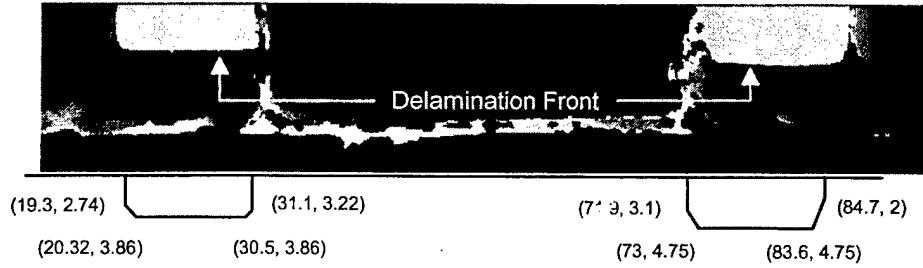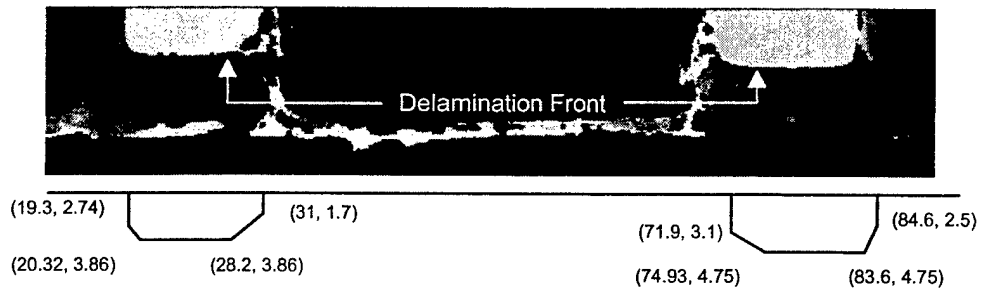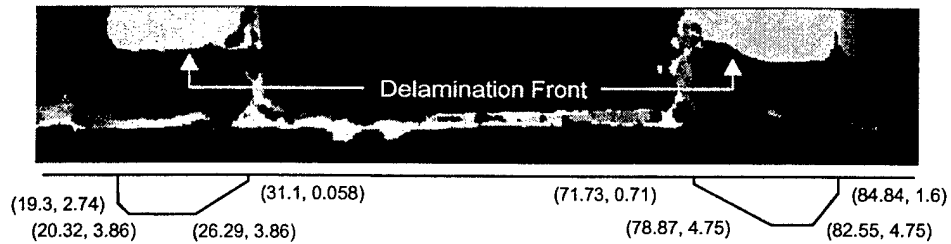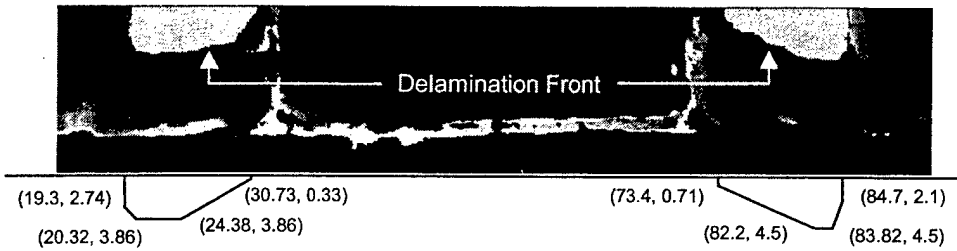
FIGURE 6-1. C-SCANS AND SKETCHES OF TYPICAL BENDING PANEL: (a) INITIAL SCAN, (b) LOAD = 272 N, (c) LOAD = 317 N, (d) LOAD = 379 N, AND (e) LOAD = 404 N

The amplitude data presented in the C-scan images of figure 6-1 are represented in gray scale. The darker colors represent stronger signals, whereas lighter colors represent weaker signals. The light gray regions in figure 6-1 illustrated the bonded flanges, representing back surface reflections from the 12-ply portions of the specimen. The dark regions are the delaminated flanges and the sheet region and represent back surface reflections from the six-ply portions of the specimen. The delaminated flange and sheet-back surfaces are the same for both regions. The jagged gray band across the width of the specimen, a short distance above the bottom of each scan, occurs as a result of wrinkles formed on the sheet during manufacturing. This band also indicates the length-wise location where the flanges terminate. The dark region below this gray band is the flat sheet portion of the specimen that extends beyond the hat-stiffener. The images are shown using the same viewpoint as that used for the presentation of all predicted results; i.e., the sheet is on top (out of the page) and the hat-stiffener is below it (into the page). With reference to figure 4-3, the positive z axis points out of the page. The horizontal direction is along the width of the specimen, while the vertical direction is along the specimen's length. The delamination is growing from bottom to top. It should be noted that the actual scans showed the edges of the specimen, however the images shown in figure 6-1 are cropped to allow for a magnified view of the region surrounding the delamination fronts. It should be noted that the precise locations of the inner corners of the delamination front cannot be resolved due to the fillet from the vertical portion of the stiffener. Figure 6-2 shows the cross section of a hat-stiffened panel and the shape of the fillet at the inner corner of the flanges. This shape of the fillet was observed in all the specimens. Due to the curved back surface at the inner corners, the sound waves were scattered and the transducer received poor sound wave reflections; hence, that shape of the delamination front at the inner corners could not be resolved.
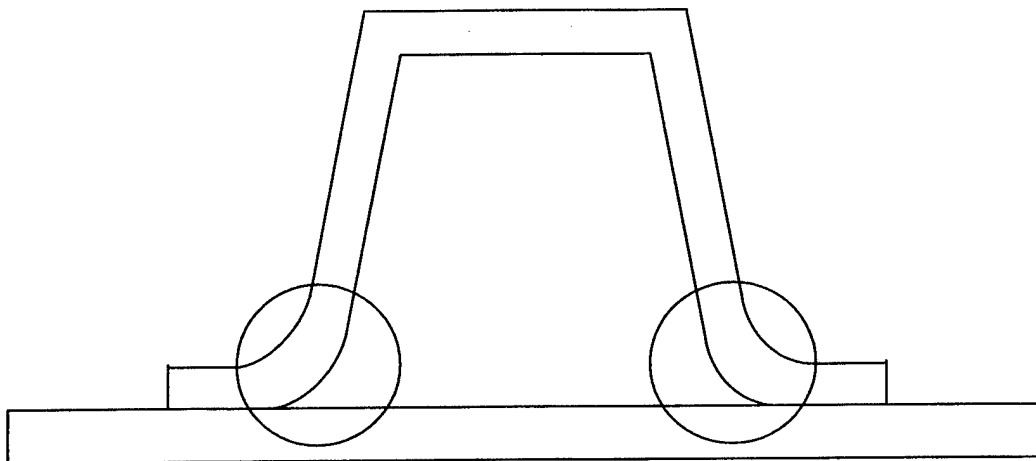
FIGURE 6-2. CROSS-SECTIONAL VIEW OF HAT-STIFFENED PANEL
SHOWING FILLET REGION

For the bending case, the pre-implanted teflon delamination was approximately 6.35 mm long. This value may be used to provide a relative length measurement along both vertical and horizontal directions. Figure 6-1(a) presents the scan of the initial delamination front. The end of the pre-implanted teflon is present at the bottom edge of the light region and the teflon extends into the dark (delaminated) region below it. It is the bottom edge of the light region that gives the shape of the initial delamination front.

The scans shown in figures 6-1(b) through 6-1(e) show delamination growth events after the specimen was subjected to loads. Figure 6-1(b) shows that the shape of the delamination front is similar to figure 6-1(a), except for the inner corners of the left and right delamination fronts. At the inner corners, the delamination has grown upwards, over a small width of the delamination fronts. Growth is indicated when the dark (delaminated) region extends into the light (bonded) region. Figures 6-1(c) and 6-1(d) show additional amounts of delamination growth along both fronts near the inner corners. In each case it can be observed that the delaminated region has advanced over more locations along the initial delamination front compared to the previous scan. In figure 6-1(e), it can be clearly seen that the shape of the delamination front has changed totally compared to the initial delamination front shown in figure 6-1(a). Figure 6-1(e) also shows that the delamination has advanced over all locations along the initial left delamination front, indicating that full growth has taken place on this side.

Figure 6-1 also presents simplified sketches corresponding to each image. The sketches, which have the same viewpoint as the images, are used to ascertain the regions of delamination fronts that have advanced. The horizontal line on the top of each sketch is used as the datum, which is at a fixed length from the bottom edge of the sheet. This is used as a reference for measuring the length (vertical distance in the downward direction) to any location on the delamination front. In each sketch, the delamination profile is characterized by a few points, which describe the basic shape of the front and are used for characterizing the experimental data. The locations of these points were obtained by examining the C-scans using a digitizer that is contained within the ultrasonic inspection software. The first coordinate gives the horizontal distance of the point from the left edge of the sheet, which is parallel to the stiffener. The second coordinate gives the length from the horizontal datum line on the top of each sketch. All numerical values are given in millimeters.

Although all the specimens were manufactured so that the initial fronts would be straight, some specimens showed an irregular initial delamination front. Nevertheless, delamination growth measurements were made by assuming all specimens had an initially straight delamination front. For the specimens that actually did have an initial straight delamination front, it was simple to locate its position with respect to the horizontal datum line defined above. For the specimens with an irregular front, the location of the initial front was estimated by examining the first few C-scans of the specimen. Once the location of the initial front was known, with respect to the horizontal datum line, the delamination front from any scan was compared to this initial front to determine the locations where the delaminations had advanced. For subsequent scans, the shape of the delamination front was constructed by drawing straight-line segments between actual delamination point measurements. These locations along the flange width are given by the first coordinate of a point on the delamination front. In general, the experimental results were reduced in a way to be comparable to the predictions. Since it was predicted that delaminations would initiate at the inner corners and then progress over the remaining front, evaluation of the experimental results mainly focused on obtaining the region of delamination growth starting from the inner corners, and hence, only a few points on the actual delamination front were selected to obtain the experimental data.

Figure 6-1(a) presents the pretest scan. From the sketch, the vertical distance for the left delamination front is 3.86 mm from the horizontal datum line. For the right delamination front,

the vertical distance is 4.75 mm from the horizontal datum line. Figure 6-1(b) shows the sketch obtained after the specimen was subjected to a load of 272 N. Comparing this to the sketch of figure 6-1(a), it can be seen that the delamination front near the inner corners has advanced along both fronts. For the left side, the delamination front has advanced over a specific region along the flange width from location (31.1, 3.86) to location (30.5, 3.86) and similarly, for the right side, from location (72.8, 4.75) to location (73, 4.75). That is, the inner 0.6 mm of the left front has advanced. The inner corner of the right front was initially not square, but advance has clearly occurred over 0.2 mm of this portion of the front.

Figures 6-1(c) to 6-1(e) present subsequent scans and sketches at higher loads for the bending panel B1. In each of the scans, certain regions of the front have advanced with respect to the previous scan. In fact, the delamination has fully advanced over the right front in figure 6-1(e).

Once the flange locations where delamination advance occurred were available, they were normalized to the specimen width in the same manner that was done for the predicted ERRs (described in section 5.6). Tables 6-1 through 6-5 present the complete normalized results and the corresponding loads from each bending panel. The first column of each table, denoted Event, corresponds to the number at which the test was stopped and a C-scan taken. The second column, denoted Left, presents the outer location of the advanced region along the left front, and the third column, denoted Right, presents the outer location of the advance along the right front. The inner locations of the advanced region are the inner corners of the hat-stiffener. The last column denotes the load at which the test was stopped just prior to the C-scan. For example, considering the first row of results in table 6-1, at event 1, the left delamination front in specimen B1 was shown to advance over the region from $y/W = 0.3125$ (the inner corner of the stiffener) to $y/W = 0.303$. The right delamination front was shown to have advanced over the region from $y/W = 0.6875$ (the other inner corner of stiffener) to $y/W = 0.726$, and the corresponding applied load was 272 N. This result corresponds to the sketch in figure 6-1(b), where the outer location of the advanced region is (30.5 mm, 3.86) on the left side and (73 mm, 4.75) on the right side, which is normalized to the specimen width of 100.58 mm (the width of specimen B1), to give $y/W = 30.5$ mm$/100.58$ mm $= 0.303$ on the left side and $y/W = 73$ mm$/100.58$ mm $= 0.726$ on the right side. The remaining tabulated results were obtained in a similar way using the data from the sketches. The dashes (-) in the table indicate that there was no additional delamination advance observed on that C-scan in comparison to the previous one. The left delamination front has fully advanced when the value in the Left column equals 0.156, and the right delamination front has fully advanced when the value in the Right column equals 0.844. Referring to table 6-3, the left delamination front had fully advanced by the fourth event and the right delamination front had fully advanced by the fifth event. There were a large number of intermediate C-scans performed between the events of some of the tables. However, they are not presented here because there was no change in either of the left or right delamination fronts on that C-scan in comparison to the previous one.

TABLE 6-1. DELAMINATION GROWTH RESULTS FOR BENDING PANEL B1

Event	Left	Right	Load (N)
1	0.303	0.726	272
2	0.280	0.745	317
3	0.262	0.784	379
4	0.243	0.844	404

TABLE 6-2. DELAMINATION GROWTH RESULTS FOR BENDING PANEL B2

Event	Left	Right	Load (N)
1	0.275	0.696	207
2	0.274	0.699	247
3	0.273	0.700	272
4	0.269	0.709	301
5	0.267	0.726	337
6	0.254	0.732	350
7	0.253	0.737	388
8	0.245	0.743	405
9	0.242	0.749	423
10	0.222	0.777	440
11	0.219	0.844	468
12	0.156	-	486

TABLE 6-3. DELAMINATION GROWTH RESULTS FOR BENDING PANEL B3

Event	Left	Right	Load (N)
1	0.267	0.751	251
2	0.227	0.753	278
3	-	0.754	340
4	0.156	0.758	384
5	-	0.844	406

TABLE 6-4. DELAMINATION GROWTH RESULTS FOR BENDING PANEL B4

Event	Left	Right	Load (N)
1	0.276	0.726	224
2	0.266	0.734	252
3	-	0.736	265
4	0.264	-	276
5	0.261	-	320
6	0.256	0.741	332
7	-	0.754	332
8	-	0.756	346
9	0.156	0.783	352
10	-	0.786	368

TABLE 6-5. DELAMINATION GROWTH RESULTS FOR BENDING PANEL B5

Event	Left	Right	Load (N)
1	0.251	0.752	243
2	0.249	-	247
3	0.243	-	310
4	0.241	0.756	327
5	0.237	0.844	349
6	0.156	-	372

To facilitate subsequent comparisons, average results were obtained from events that occurred at loads that were equal to or less than 278 N, 320 N, 350 N, and 388 N. For example, the growth events that occurred at a load of 278 N, or the closest value below it, were taken from each specimen. Specifically, for specimen B1, event 1 was chosen, which occurred at a load of 272 N. For specimen B2, event 3 was chosen, which event occurred at 272 N. Similarly, for specimens B3-B5, events 2, 4, and 2 were chosen, which occurred at loads 278 N, 276 N, and 247 N respectively. The results from each of the events were averaged to give a load of 269 N. To get the average region over which the delamination front advanced, the Left column values from the above events were averaged to give the value 0.263, and similarly the Right column values were averaged to give the value 0.733. The average results for the bending case are tabulated in table 6-6.

TABLE 6-6. AVERAGE DELAMINATION GROWTH RESULTS FOR
BENDING SPECIMENS

Event	Left	Right	Load (N)
1	0.263	0.733	269
2	0.256	0.739	305
3	0.251	0.766	340
4	0.197	0.782	378

6.3.2 Tension Specimens.

Five tension specimens were tested. Figure 6-3 presents a sequence of C-scans for panel T3, which is generally representative of all tension specimens. In this case, the preimplanted teflon delamination is 25.4 mm long, but the entire length of the delaminated region is not shown because the images are cropped from the actual scans. All other features of the scans are as described for the bending scans. Tables 6-7 through 6-11 present the delamination growth results of all the tension specimens. These results were once again obtained from the sketches using the same method as described for the bending case.

Average results were also obtained for the tension case using the same method as described above for the bending case and are presented in table 6-12. The events that occurred at loads that were equal to or less than 28,984 N, 35,621 N, 42,369 N, and 46,751 N were used for this purpose.
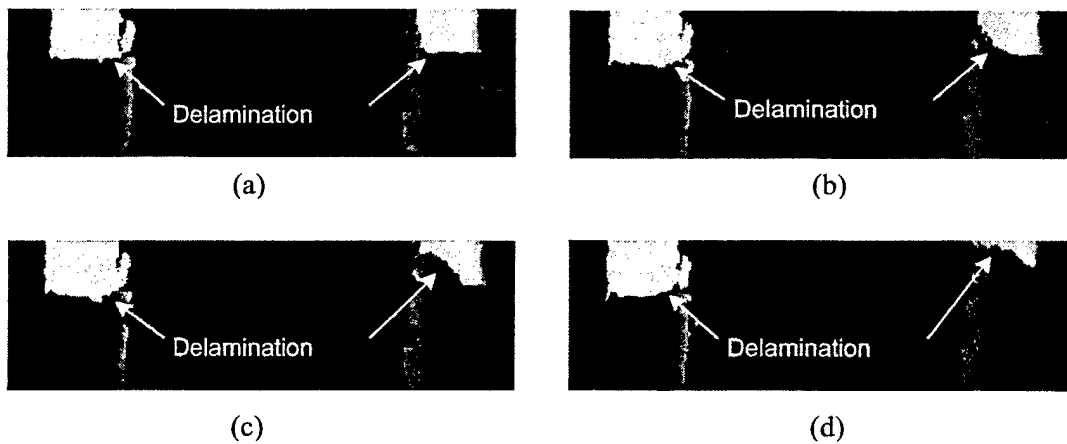
FIGURE 6-3. C-SCANS OF TYPICAL TENSION PANEL: (a) INITIAL SCAN,
(b) LOAD = 26729 N, (c) LOAD = 31177 N, AND (d) LOAD = 36978 N

TABLE 6-7. DELAMINATION GROWTH RESULTS FOR TENSION PANEL T1

Event	Left	Right	Load (N)
1	0.252	0.750	24532
2	0.250	-	26685
3	-	0.751	28909
4	0.247	0.765	31186
5	-	0.766	40038
6	0.238	0.774	42369
7	0.231	0.787	44526
8	0.156	0.844	46497

TABLE 6-8. DELAMINATION GROWTH RESULTS FOR TENSION PANEL T2

Event	Left	Right	Load (N)
1	0.230	0.791	26734
2	0.222	0.795	28984
3	-	0.796	31209
4	-	0.807	33473
5	0.221	0.844	35612
6	0.220	-	40078
7	0.217	-	44491
8	0.209	-	46751

TABLE 6-9. DELAMINATION GROWTH RESULTS FOR TENSION PANEL T3

Event	Left	Right	Load (N)
1	0.253	0.798	26729
2	0.251	0.799	28976
3	0.244	0.811	31177
4	0.243	0.814	33397
5	0.242	0.831	35617
6	0.212	0.844	36978

TABLE 6-10. DELAMINATION GROWTH RESULTS FOR TENSION PANEL T4

Event	Left	Right	Load (N)
1	0.259	0.755	28976
2	0.256	-	31177
3	0.254	-	35621
4	0.253	-	37503
5	0.251	0.760	40069
6	0.225	0.774	44526
7	-	0.787	46706
8	-	0.794	48975

TABLE 6-11. DELAMINATION GROWTH RESULTS FOR TENSION PANEL T5

Event	Left	Right	Load (N)
1	0.233	0.746	28944
2	0.231	0.747	33393
3	-	0.748	35612
4	0.230	0.749	37841
5	-	0.758	40029
6	0.229	0.763	42316
7	0.156	0.786	44615
8	-	0.810	46706
9	-	0.844	48975

TABLE 6-12. AVERAGE DELAMINATION GROWTH RESULTS FOR
TENSION SPECIMENS

Event	Left	Right	Load (N)
1	0.243	0.769	28958
2	0.239	0.789	34730
3	0.230	0.797	40362
4	0.192	0.826	44728

7. COMPARISON OF PREDICTED AND EXPERIMENTAL RESULTS.

7.1 OVERVIEW.

In this section, the reduced experimental data for the bending and tension specimens will be compared to the delamination growth predictions. The delamination growth predictions for the geometries are obtained from section 5, while the reduced experimental data is obtained from section 6. The predictions for delamination growth and the reduced data for each of the specimen types are plotted together to make qualitative and quantitative comparisons.

7.2 BENDING SPECIMENS.

Figure 7-1 presents a quantitative comparison of the predicted and observed results for the bending panels. The predictions of the straight front shown in this figure are taken from figure 5-12. The filled triangles representing the average experimental results are taken directly from table 6-6. Individual results from all the bending panels are also shown, and these are taken from tables 6-1 through 6-5.
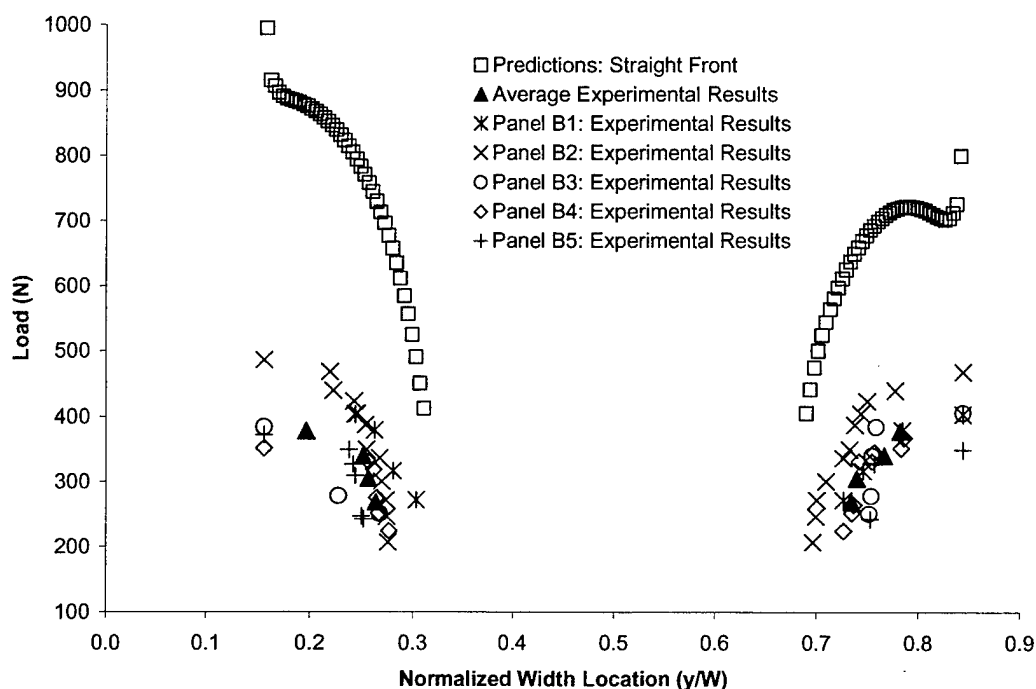
FIGURE 7-1. COMPARISON OF PREDICTED AND OBSERVED RESULTS FOR THE BENDING PANELS

From a visual comparison, most of the experimental results are lower than the predictions. Delamination was predicted to initiate at an approximate load of 475 N (the third square from the inner corner of the right front) whereas experimentally, delamination initiated in the range of 205-270 N. In addition, the maximum applied load associated with full delamination is less than 500 N in all the specimens. At the same load, the predictions indicate that the delamination would advance across a very small region at the inner corners. Even if a certain error in testing and data interpretation is considered, the difference between experimental results and predictions is quite significant. Hence, it was necessary to investigate the causes of these observed differences.

7.3 TENSION SPECIMENS.

Figure 7-2 presents the quantitative comparison between the predicted and experimental results for the tension panels. The predictions for the straight front shown in this figure are taken from figure 5-18. The average experimental results are taken from table 6-12. Also presented are the individual specimen results taken from tables 6-7 through 6-11.
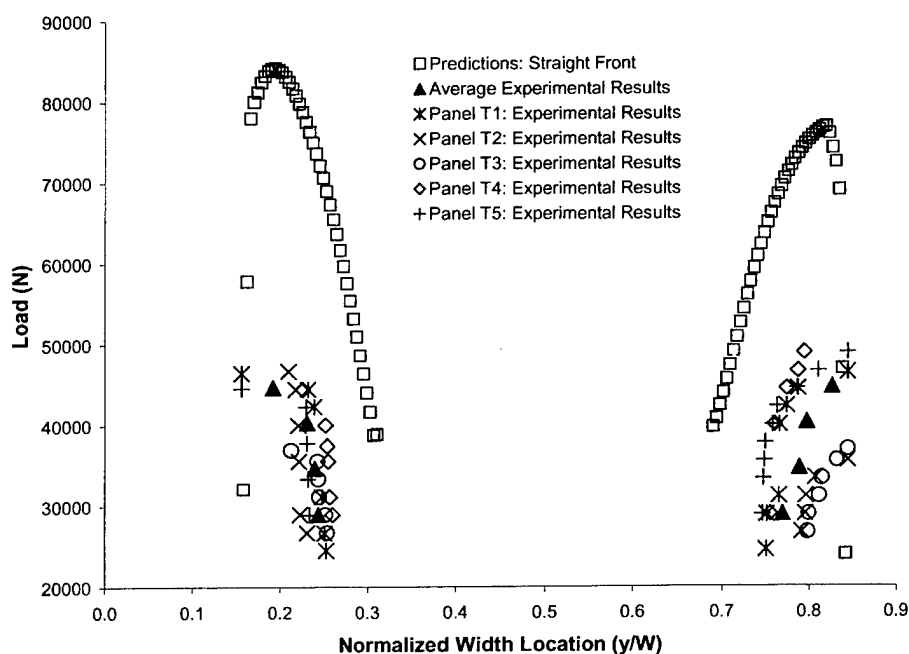
FIGURE 7-2. COMPARISON OF PREDICTED AND OBSERVED RESULTS FOR THE TENSION PANELS

Figure 7-2 shows that the experimental results are lower than the predictions. Delamination initiation was predicted to occur at 41,700 N (based upon the third square symbol near the inner corner of the left front), but experimentally, this was observed to be in the range of 24,500-29,000 N. As for the bending panels, it was clear that additional study was required to understand these results.

7-2

8. FACTORS AFFECTING PREDICTIONS.

Due to the poor comparison between the predicted and experimental results for the bending and tension specimens, it was necessary to investigate the factors that affected the predictions for delamination initiation and delamination advance. This section presents these investigations and their results. Several issues relating to the material properties, manufacturing, and fracture behavior may have been responsible for the poor comparison.

The first factor that may have affected predictions involved the fracture toughness of the T800H/3900-2 material. The curve shown in figure 5-1 was obtained by experimentally determining the fracture toughness of unidirectional flat plate specimens with mid-plane delaminations under a series of different mode mixities. These flat specimens were considerably thicker than the hat-stiffened panels and were also manufactured using a different technique than the one used here. For the flat plate specimens, an upper caul plate was placed on top of the plies prior to cure. For the stiffened panels, the hat-stiffened region was covered by a rubber mold and caul plates were placed on the overhanging sheet regions. In both the stiffener and sheet regions, there was more compaction (due to the thin layup) than in the flat specimens tested previously. This was verified by comparing the measured single-ply thickness of 0.174 mm (cf. table 5-1) for the hat panel specimens to the measured single-ply thickness of 0.182 mm for the batch 1 flat-plate specimens [11 and 14] and 0.179 mm for batch 2 flat-plate specimens [11].

The second factor affecting predictions relates to the fillet at the inner corners of the sheet-stiffener interface. The inner corners of the sheet-stiffener bonded region were observed to have a fillet, which is shown in figure 6-2. The fillet shape was obtained because there was excess resin deposited near the inner corners of the flanges. This resulted in a higher thickness at the inner most corners, with a gradually reducing thickness towards the outer edge of the flanges. Note that the pre-implanted teflon delamination is present between two -45° plies. The delamination may advance through the thermoplastic interlayer between the plies, referred to subsequently as interlaminar advance, or it may move into one of the adjacent plies and grow within a ply. This latter type of growth is referred to subsequently as intralaminar advance. The excess resin present in the fillet region provides a path of low resistance for the delamination to grow into an adjacent ply; that is, more base epoxy resin in the fillet region implies a lower percentage of thermoplastic. Since the resin has a considerably lower toughness than the toughened thermoplastic interlayer, the above phenomenon would give a lower observed toughness in the fillet region.

The third factor that could have affected the correlation between predicted and observed results was the fracture behavior outside of the fillet region and along the remainder of the front. For the fillet region, it was possible that the experimental results were lower because delamination advance occurred intralaminarly (through a ply), whereas the predictions were based upon the assumption that the delamination advanced through the interlaminar region, or interlaminarly. In the former case, intralaminar growth would result in a lower toughness, i.e., the base resin. As will be shown subsequently, this type of behavior did indeed occur. In addition, a large change in the location of the crack plane (with respect to the thickness direction) would also change the mode mixity, such that it was different than that given by the model, which assumes a mid-plane delamination. However, no significant changes in the plane of the delamination were observed in posttest inspections. The effect on the predicted ERRs, due to the mode mixity changing as a

result of changes in the location of the plane of the crack, were therefore assumed to be second-order effects and were ignored.

9. CONCLUSIONS AND RECOMMENDATIONS.

9.1 CONCLUSIONS.

A crack tip element approach has been applied for predicting delamination growth in complex structural geometries and the accuracy of this approach has been evaluated by comparison to experimental results. This has been done using a toughened graphite/epoxy material system, T800H/3900-2. Two hat-stiffened skin panel geometries were chosen that are typical to aircraft applications; one of these was subjected to bending loads and the other to tension.

Initially, mesh refinement studies were performed to establish that triangular elements could be used within the double-plate FE model that is required for the 3D CTE analysis. The primary advantage of the triangular elements, as compared to the previous method that used rectangular elements, is the improved accuracy that can be obtained in modeling a curved delamination front. For a straight delamination front, it was shown that essentially the same results for ERR and mode mix distributions are obtained whether triangular or rectangular elements were used. This was taken as verification of the approach, and triangular elements were used for all subsequent studies.

Following the mesh refinement studies, ERR and mode mix distributions were obtained for the two geometries under consideration. These results were used with previously developed toughness data to make delamination growth predictions. Test specimens were then fabricated, experiments were performed, and the predictions were compared to the observed results. Initial comparisons showed that the delamination growth predictions were significantly higher than the experimental results. The poor correlation was attributed to differences in manufacturing between simple coupons and hat-stiffened elements that affected fracture properties and crack growth locations.

9.2 OBSERVATIONS.

In this work and other previous works, it has been shown that the crack tip element analysis provides accurate total energy release rate and classically defined energy release rate components. The crack tip element approach has also been shown to provide highly accurate delamination growth predictions when the total energy release rate is decomposed into nonclassical components. As expected, the accuracy of the crack tip element analysis was not the issue in this study. Rather, the fundamental issue was found to be the complex fracture behavior of T800H/3900-2. In this type of material, three different modes of growth are observed. The delamination can grow (1) within the toughened interlayer region, (2) within one of the adjacent plies, and/or (3) along the base resin-to-interlayer interface. Due to dispersion of the thermoplastic matrix within the base resin, the delamination toughness associated with mechanisms (2) and (3) is expected to be quite similar. However, this fracture toughness is significantly lower than what will be observed if delamination advance remains within the interlayer region. In comparison, for a fibrous composite that uses an epoxy or toughened-epoxy matrix and no interlayer, there is no significant difference in interlaminar versus intralaminar delamination toughness.

9.3 RECOMMENDATIONS.

The conclusions from this study indicate that the fundamental issue in this study is the nature of delamination advance. Assuming that the toughnesses obtained from delamination growth within a ply will be essentially the same as those obtained from advance along the base resin-to-interlayer interface, the issue comes down to the toughness for interlaminar versus intralaminar growth. Thus, for T800H/3900-2 and other such materials that may be introduced in the future, toughness data needs to be obtained that reflects the nature of growth.

The first recommendation of this work is that, for materials such as T800H/3900-2, two sets of delamination toughness data (toughness versus mode mix) be obtained. The first is for interlaminar growth, and the approach to do this is as described in reference 12. The second toughness versus mode mix curve is for intralaminar growth. As a starting point, unidirectional specimens can be used for this, and test methods adopted where multiple increments of crack advance can be performed on the same specimen. As shown in reference 14, this has the potential to drive the delamination out of the toughened interlayer and therefore to obtain the desired data. For mode I, this can be accomplished using the double cantilever beam (DCB) test [14]. For mixed mode I-II, it can be accomplished using the mixed mode bending (MMB) test, and for mode II it can be accomplished using the recently introduced four-point end-notched flexure (4ENF) test [45 through 47]. Crack advance is stable for each of these test methods. Thus, at any mode mix, the tests can be used to obtain toughness for a series of crack advancements. The initiation toughness from the test will produce the desired interlaminar toughness; similar to that observed in reference 14, it is probable that after sufficient amounts of advance, the delamination will leave the toughened region. This will likely be evidenced by an observed toughness versus crack advance curve that steadily decreases from the initial (large) interlaminar toughness to a lower steady-state toughness. The steady-state toughness refers to a series of delamination growth increments where the toughness values stabilize once the delamination has begun growing fully within an adjacent ply or at the base resin-to-thermoplastic interface. This steady-state value is taken as the intralaminar toughness. If it is found that unidirectional specimens do not give the desired data, then various multidirectional specimens should be evaluated. However, this would also require changes to the existing data reduction methods, so there is no reason to speculate on the approach to be used until the need for it is established. It is quite possible that the unidirectional tests described above will be sufficient.

The second recommendation is that the CTE/NSF approach be used to make delamination growth assessments. As described in this work and many others, there is now ample data that shows that this approach is significantly more efficient and as accurate or more accurate for making delamination growth predictions than FE-based approaches. The toughness data to use in this approach (intralaminar or interlaminar) depends on the situation under consideration and the philosophy of the user. Using intralaminar toughness data will yield more conservative results that one could apply this in all situations. The primary advantage of a material such as T800H/3900-2 would then be its compression-after-impact strength and other established metrics, excluding delamination growth, that are part of typical material selection, qualification, and structural certification processes [40]. Alternatively, there may be certain other situations where the plies bounding the delamination and the local structural details support the use of the higher interlaminar toughness. More research on how to distinguish such situations is certainly required.

10. REFERENCES.

1. Davidson, B.D., Hu, H., and Schapery, R.A., "An Analytical Crack Tip Element for Layered Elastic Structures," *Journal of Applied Mechanics*, Vol. 62, 1995, pp. 294-305.

2. O'Brien, T.K., "Towards a Damage Tolerance Philosophy for Composite Materials and Structures," *Composite Materials: Testing and Design (Ninth Volume)*, ASTM STP 1059, S.P. Garbo, ed., American Society for Testing and Materials, 1990, pp. 7-33.

3. Davidson, B.D., Gharibian, S.J., and Yu, L., "Evaluation of Energy Release Rate-Based Approaches for Predicting Delamination Growth in Laminated Composites," *International Journal of Fracture*, Vol. 105, No. 4, 2000, pp. 343-365.

4. Schapery, R.A. and Davidson, B.D., "Prediction of Energy Release Rate for Mixed-Mode Delamination Using Classical Plate Theory," *Applied Mechanics Reviews*, Vol. 43, No. 5, 1990, pp. S281-S287.

5. Davidson, B.D., Hu, H., and Yan, H., "An Efficient Procedure for Determining Mixed-Mode Energy Release Rates in Practical Problems of Delamination," *Finite Elements in Analysis and Design*, Vol. 23, 1996, pp. 193-210.

6. Davidson, B.D., Yu, L. and Hu, H., "Determination of Energy Release Rate and Mode Mix in Three-Dimensional Layered Structures Using Plate Theory," *International Journal of Fracture*, Vol. 105, No. 1, 2000, pp. 81-104.

7. Davidson, B.D., Fariello, P.L., Hudson, R.C., and Sundararaman, V., "Accuracy Assessment of the Singular Field-Based Mode Mix Decomposition Procedure for the Prediction of Delamination," *Composite Materials: Testing and Design (Thirteenth Volume)*, ASTM STP 1242, S.J. Hooper, ed., American Society for Testing and Materials, 1997, pp. 109-128.

8. Kinloch, A.J., Wang, Y., Williams, J.G., and Yayla, P., "The Mixed-Mode Delamination of Fibre Composite Materials," *Composites Science and Technology*, Vol. 47, No. 3, 1993, pp. 225-237.

9. Hashemi, S., Kinloch, A.J., and Williams, J.G., "Mixed-Mode Fracture in Fiber-Polymer Composite Laminates," *Composite Materials: Fatigue and Fracture (Third Volume)*, ASTM STP 1110, T.K. O'Brien, ed., American Society for Testing and Materials, 1991, pp. 143-168.

10. Charalambides, M., Kinloch, A.J., Wang, Y., and Williams, J.G., "On the Analysis of Mixed-Mode Failure," *International Journal of Fracture*, Vol. 54, 1992, pp. 269-291.

11. Bialaszewski, R.D., "A Non-Classical, Energy Release Rate-Based Approach to Predicting Delamination Growth in Laminated Composites," M.S. Thesis, Syracuse University, August 2000.

12. Davidson, B.D., "A Predictive Methodology for Delamination Growth in Laminated Composites Part II: Analysis, Applications, Accuracy Assessment and Recommendations," DOT/FAA/AR-01/56, October 2001.

13. Gharibian, S.J., "Verification of a Methodology for Predicting Delamination Growth in Laminated Graphite/Epoxy Composites," M.S. Thesis, Syracuse University, May 1999.

14. Sainath, S., "Verification of a Non-Classical Energy Release Rate Based Approach for Predicting Delamination Growth in a Two-Phase Graphite/Epoxy Composite Material," M.S. Thesis, Syracuse University, July 1999.

15. Davidson, B.D. and Krafchak, T.M., "Analysis of Instability-Related Delamination Growth Using a Crack Tip Element," *AIAA Journal,* Vol. 31, No.11, 1993, pp. 2130-2136.

16. Davidson, B.D., "A Predictive Methodology for Delamination Growth in Laminated Composites Part I: Theoretical Development and Preliminary Experimental Results," DOT/FAA/AR-97/87, April 1998.

17. Davidson, B.D., "Energy Release Rate Determination for Edge Delamination in Laminates Subjected to Combined In-Plane, Bending and Hygrothermal Loading -Part I: Delamination at a Single Interface," *Journal of Composite Materials,* Volume 28, No.11, 1994, pp. 1009-1031.

18. Davidson, B.D., "Energy Release Rate Determination for Edge Delamination in Laminates Subjected to Combined In-Plane, Bending and Hygrothermal Loading -Part II: Two Symmetrically Located Delaminations," *Journal of Composite Materials,* Volume 28, No.14, 1994, pp. 1371-1392.

19. Davidson, B.D. and Hu, H., "Effect of Interlayer Modulus on Fracture Mode Ratio for Interleaved Composite Laminates," *Engineering Fracture Mechanics,* Vol. 52, No.2, 1995, pp. 243-253.

20. Yu, L. and Davidson, B.D., "A Three-Dimensional Crack Tip Element for Energy Release Rate Determination in Layered Elastic Structures," *Journal of Composite Materials*, Vol. 35, 2001, pp. 457-488.

21. Broek, D., "Elementary Engineering Fracture Mechanics: Fourth Revised Edition," *Kluwer Academic Publishers*, Dordrecht, 1986.

22. Rybicki, E.F. and Kanninen, M.F., "A Finite Element Calculation of Stress Intensity Factors by a Modified Crack Closure Integral," *Engineering Fracture Mechanics,* Vol. 9, 1977, pp. 931-938.

23. Davidson, B.D., "Prediction of Energy Release Rate for Edge Delamination Using a Crack Tip Element Approach," *Composite Materials: Fatigue and Fracture - Fifth Volume,* ASTM STP 1230, R.H. Martin, ed., American Society for Testing and Materials, 1995, pp. 155-175.

24. Raju, I.S., Crews, J.H. Jr., and Aminpour, M.A., "Convergence of Strain Energy Release Rate Components for Edge-Delaminated Composite Laminates," *Engineering Fracture Mechanics,* Vol. 30, No.3, 1988, pp. 383-396.

25. Sun, C.T. and Manoharan, M.G., "Strain Energy Release Rates of an Interfacial Crack Between Two Orthotropic Solids," *Journal of Composite Materials,* Vol. 23, 1989, pp. 460-478.

26. Hwu, C. and Hu, J.S., "Stress Intensity Factors and Energy Release Rates of Delaminations in Composite Laminates," *Engineering Fracture Mechanics,* Vol. 42, No. 6, 1992, pp. 977-988.

27. Beuth, J.L., "Separation of Crack Extension Modes in Orthotropic Delamination Models," *International Journal of Fracture,* Vol. 77, 1996, pp. 305-321.

28. Martin, R.H., "Local Fracture Mechanics Analysis of Stringer Pull-Off and Delamination in a Post-Buckled Compression Panel," *Proceedings of the Tenth International Conference on Composite Materials,* Vol. I: Fatigue and Fracture, A. Poursartip and K. Street, eds., August 1995, pp. 253-260.

29. Minguet, P.J. and O'Brien, T.K., "Analysis of Composite Skin/Stringer Bond Failure Using a Strain Energy Release Rate Approach," *Proceedings of the Tenth International Conference on Composite Materials,* Vol. I: Fatigue and Fracture, A. Poursartip and K. Street, eds., August 1995, pp. 245-252.

30. Li, J, O'Brien, T.K., and Rousseau, C.Q., "Test and Analysis of Composite Hat Stringer Pull-Off Test Specimens," *Journal of the American Helicopter Society,* October 1997, pp. 350-357.

31. Li, J., "Three-Dimensional Effect in the Prediction of Flange Delamination in Composite Skin-Stringer Pull-Off Specimens," *Proceedings of the 15th Annual American Society for Composites Technical Conference,* O.O. Ochoa, T.K. O'Brien, D. Lagoudas and H.J. Sue, Eds., Technomic Publishing Co., 2000, pp. 983-990.

32. Krueger, R., Civitkovich, M.K., and O'Brien, T .K., "Testing and Analysis of Composite Skin/Stringer Debonding Under Multi-Axial Loading," *Journal of Composite Materials,* Vol. 34, No.15, 2000, pp. 1263-1300.

33. Krueger, R., Minguet, P.J., and O'Brien, T.K., "A Method for Calculating Strain Energy Release Rates in Preliminary Design of Composite Skin/Stringer Debonding Under Multi-Axial Loading," *Composite Structures: Theory and Practice,* ASTM STP 1383, P. Grant and C.Q. Rousseau, eds., American Society for Testing and Materials, 2000, pp. 105-128.

34. Whitney, J.M., "Structural Analysis of Laminated Anisotropic Plates," Technomic, 1987.

35. Davidson, B.D., "Prediction of Delamination Growth in Laminated Structures," *Failure Mechanics in Advanced Polymeric Composites,* AMD-Vol. 196, G.A. Kardomateas and Y.D.S. Rajapakse, eds., American Society of Mechanical Engineers, 1994, pp. 43-65.

36. König, M. and Krüger, R., "Delamination Growth Under Cyclic Loading," Proceedings of the 8th European Conference on Composite Materials (ECCM-8), I.C. Visconti, Ed., Woodhead Publishing Ltd., 1998, pp. 479-486.

37. König, M., Krüger, R., and Rinderknecht, S., "Finite Element Analysis of Delamination Growth in a Multidirectional Composite ENF Specimen," *Composite Structures: Theory and Practice,* ASTM STP 1383, P. Grant and C.Q. Rousseau, Eds., American Society for Testing and Materials, 2000, pp. 345-365.

38. Vintilescu, I and Spelt, J., "Mixed Mode I, II, and III Fracture Characterization of Adhesive Joints," *Journal of Composites Technology and Research,* Vol. 20, No.2, 1998, pp. 129-139.

39. Yu, L., "A Crack Tip Element-Based Approach for Energy Release Rate Determination and Delamination Growth Prediction in Laminated Composites," Ph.D. Dissertation, Department of Mechanical, Aerospace and Manufacturing Engineering, Syracuse University, in Preparation.

40. Odagiri, N., Kishi, H., and Yamashita, M., "Development of TORAYCA Prepreg P2302 Carbon Fiber Reinforced Plastic for Aircraft Primary Structural Materials," *Advanced Composite Materials,* Vol. 5, No.3, 1996, pp. 249-254.

41. Davidson, B.D., "An Analytical Investigation of Delamination Front Curvature in Double Cantilever Beam Specimens," *Journal of Composite Materials,* Vol. 24, No. 11, 1990, pp. 1124-1137.

42. Davidson, B.D., Altonen, C.S., and Polaha, J.J., "Effect of Stacking Sequence on Delamination Toughness and Delamination Growth Behavior in Composite End-Notched Flexure Specimens," *Composite Materials: Testing and Design (Twelfth Volume),* ASTM STP 1274, C.R. Saff and R.B. Deo, eds., American Society for Testing and Materials, 1996, pp. 393-413.

43. Davidson, B.D., Michaels, J.E., Sundararaman, V., and Michaels, T.E., "Ultrasonic Imaging of Impact Damaged Composite Panels," *Acoustical Imaging,* Volume 19, H. Ermert and H.-P. Harjes, Eds., Plenum Press, 1992, pp. 589-594.

44. Michaels, T.E., Krafchak, T.M., and Davidson, B.D., "Ultrasonic Inspection of Thin Walled Composite Tubes," *Review of Progress in Quantitative Nondestructive Evaluation,* Volume 12, D.O. Thompson and D.E. Chimenti, eds., Plenum Press, 1992.

45. Martin, R.H. and Davidson, B.D., "Mode II Fracture Toughness Evaluation Using a Four Point Bend End-Notched Flexure Test," *Plastics, Rubber and Composites,* Vol. 28, No. 8, 1999, pp. 401-406.

46.   Schuecker, C. and Davidson, B.D., "Evaluation of the Accuracy of the Four-Point Bend End-Notched Flexure Test for Mode II Delamination Toughness Determination," *Composites Science and Technology*, Vol. 60, 2000, pp. 2137-2146.

47.   Schuecker, C. and Davidson, B.D., "Effect of Friction on the Perceived Mode II Delamination Toughness from Three- and Four-Point Bend End-Notched Flexure Tests," *Composite Structures: Theory and Practice*, ASTM STP 1383, P. Grant and C.Q. Rousseau, eds., American Society for Testing and Materials, 2000, pp. 334-344.

This appendix presents the FE input files for the bending analysis and nonlinear tension analysis of hat-stiffened geometries that are constructed and solved using Abaqus, licensed from Hibbitt, Karlsson, and Sorenson, Inc. The bending model uses three-noded and eight-noded shear deformable elements. The nonlinear tension model uses eight-noded shear deformable elements.

```
-----------------------------------------------------------------------------------
**INPUT FILE FOR BENDING ANALYSIS (STRAIGHT DELAMINATION FRONT)
**ABAQUS MODEL PER PLY THICK = 0.006833 INCH = 0.041 TOTAL
*RESTART,WRITE
*PRE PRINT,ECHO=NO,HISTORY=NO,MODEL=NO
*NODE
**sheet1
1,-5.500,0.0,0.0205
41,-0.50,0.0,0.0205
45,-0.25,0.0,0.0205
49,-0.05,0.0,0.0205
51,-0.025,0.0,0.0205
55,-0.011,0.0,0.0205
59,-0.0055,0.0,0.0205
75,0.0055,0.0,0.0205
79,0.011,0.0,0.0205
83,0.025,0.0,0.0205
85,0.05,0.0,0.0205
89,0.25,0.0,0.0205
93,0.50,0.0,0.0205
101,1.50,0.0,0.0205
**sheet6
51201,-5.500,4.0,0.0205
51241,-0.50,4.0,0.0205
51245,-0.25,4.0,0.0205
51249,-0.05,4.0,0.0205
51251,-0.025,4.0,0.0205
51255,-0.011,4.0,0.0205
51259,-0.0055,4.0,0.0205
51275,0.0055,4.0,0.0205
51279,0.011,4.0,0.0205
51283,0.025,4.0,0.0205
51285,0.05,4.0,0.0205
51289,0.25,4.0,0.0205
51293,0.50,4.0,0.0205
51301,1.50,4.0,0.0205
**hat1
102,-5.500,0.625,-0.0205
142,-0.500,0.625,-0.0205
```

```
146,-0.250,0.625,-0.0205
150,-0.050,0.625,-0.0205
152,-0.025,0.625,-0.0205
156,-0.011,0.625,-0.0205
160,-0.0055,0.625,-0.0205
176,0.0055,0.625,-0.0205
180,0.011,0.625,-0.0205
184,0.025,0.625,-0.0205
186,0.050,0.625,-0.0205
190,0.250,0.625,-0.0205
192,0.375,0.625,-0.0205
**hat 2
8102,-5.500,1.25,-0.0205
8142,-0.500,1.25,-0.0205
8146,-0.250,1.25,-0.0205
8150,-0.050,1.25,-0.0205
8152,-0.025,1.25,-0.0205
8156,-0.011,1.25,-0.0205
8160,-0.0055,1.25,-0.0205
8176,0.0055,1.25,-0.0205
8180,0.011,1.25,-0.0205
8184,0.025,1.25,-0.0205
8186,0.050,1.25,-0.0205
8190,0.250,1.25,-0.0205
8192,0.375,1.25,-0.0205
**hat 3
27302,-5.500,1.5,-1.55
27342,-0.500,1.5,-1.55
27346,-0.250,1.5,-1.55
27350,-0.050,1.5,-1.55
27352,-0.025,1.5,-1.55
27356,-0.011,1.5,-1.55
27360,-0.0055,1.5,-1.55
27376,0.0055,1.5,-1.55
27380,0.011,1.5,-1.55
27384,0.025,1.5,-1.55
27386,0.050,1.5,-1.55
27390,0.250,1.5,-1.55
27392,0.375,1.5,-1.55
**hat 4
40102,-5.500,2.5,-1.55
40142,-0.500,2.5,-1.55
40146,-0.250,2.5,-1.55
40150,-0.050,2.5,-1.55
40152,-0.025,2.5,-1.55
40156,-0.011,2.5,-1.55
40160,-0.0055,2.5,-1.55
40176,0.0055,2.5,-1.55
40180,0.011,2.5,-1.55
40184,0.025,2.5,-1.55
40186,0.050,2.5,-1.55
40190,0.250,2.5,-1.55
40192,0.375,2.5,-1.55
**hat 5
59302,-5.500,2.75,-0.0205
59342,-0.500,2.75,-0.0205
59346,-0.250,2.75,-0.0205
```

```
59350,-0.050,2.75,-0.0205
59352,-0.025,2.75,-0.0205
59356,-0.011,2.75,-0.0205
59360,-0.0055,2.75,-0.0205
59376,0.0055,2.75,-0.0205
59380,0.011,2.75,-0.0205
59384,0.025,2.75,-0.0205
59386,0.050,2.75,-0.0205
59390,0.250,2.75,-0.0205
59392,0.375,2.75,-0.0205
**hat 6
67302,-5.500,3.375,-0.0205
67342,-0.500,3.375,-0.0205
67346,-0.250,3.375,-0.0205
67350,-0.050,3.375,-0.0205
67352,-0.025,3.375,-0.0205
67356,-0.011,3.375,-0.0205
67360,-0.0055,3.375,-0.0205
67376,0.0055,3.375,-0.0205
67380,0.011,3.375,-0.0205
67384,0.025,3.375,-0.0205
67386,0.050,3.375,-0.0205
67390,0.250,3.375,-0.0205
67392,0.375,3.375,-0.0205
*NGEN
**sheet 1
1,41
41,45
45,49
49,51
51,55
55,59
59,75
75,79
79,83
83,85
85,89
89,93
93,101
**sheet6
51201,51241
51241,51245
51245,51249
51249,51251
51251,51255
51255,51259
51259,51275
51275,51279
51279,51283
51283,51285
51285,51289
51289,51293
51293,51301
**hat 1
102,142
142,146
146,150
```

```
150,152
152,156
156,160
160,176
176,180
180,184
184,186
186,190
190,192
**hat 2
8102,8142
8142,8146
8146,8150
8150,8152
8152,8156
8156,8160
8160,8176
8176,8180
8180,8184
8184,8186
8186,8190
8190,8192
**hat 3
27302,27342
27342,27346
27346,27350
27350,27352
27352,27356
27356,27360
27360,27376
27376,27380
27380,27384
27384,27386
27386,27390
27390,27392
**hat 4
40102,40142
40142,40146
40146,40150
40150,40152
40152,40156
40156,40160
40160,40176
40176,40180
40180,40184
40184,40186
40186,40190
40190,40192
**hat 5
59302,59342
59342,59346
59346,59350
59350,59352
59352,59356
59356,59360
59360,59376
59376,59380
```

```
59380,59384
59384,59386
59386,59390
59390,59392
**hat 6
67302,67342
67342,67346
67346,67350
67350,67352
67352,67356
67356,67360
67360,67376
67376,67380
67380,67384
67384,67386
67386,67390
67390,67392
*NSET,NSET=SHEET1,GEN
1,101,1
*NSET,NSET=SHEET6,GEN
51201,51301,1
*NSET,NSET=HAT1,GEN
102,192
*NSET,NSET=HAT2,GEN
8102,8192
*NSET,NSET=HAT3,GEN
27302,27392
*NSET,NSET=HAT4,GEN
40102,40192
*NSET,NSET=HAT5,GEN
59302,59392
*NSET,NSET=HAT6,GEN
67302,67392
**FILL ALL NODES IN
*NFILL,NSET=SHEETA
SHEET1,SHEET6,256,200
*NFILL,NSET=HATA
HAT1,HAT2,40,200
*NFILL,NSET=HATB
HAT2,HAT3,96,200
*NFILL,NSET=HATC
HAT3,HAT4,64,200
*NFILL,NSET=HATD
HAT4,HAT5,96,200
*NFILL,NSET=HATE
HAT5,HAT6,40,200
*NSET,NSET=HATS
HATA,HATB,HATC,HATD,HATE
*NSET,NSET=PSTRAIN
SHEETA,HATS
**DEFINING 8-NODED MASTER ELEMENTS
*ELEMENT,TYPE=S8R
**8-noded master elements for the sheet
1,1,3,403,401,2,203,402,201
2001,8001,8003,8403,8401,8002,8203,8402,8201
2038,8075,8077,8477,8475,8076,8277,8476,8275
4001,16001,16003,16403,16401,16002,16203,16402,16201
```

```
8801,35201,35203,35603,35601,35202,35403,35602,35401
8838,35275,35277,35677,35675,35276,35477,35676,35475
10801,43201,43203,43603,43601,43202,43403,43602,43401
**8-noded master elements for the hat
53,102,104,504,502,103,304,503,302
90,176,178,578,576,177,378,577,376
2053,8102,8104,8504,8502,8103,8304,8503,8302
6853,27302,27304,27704,27702,27303,27504,27703,27502
10053,40102,40104,40504,40502,40103,40304,40503,40302
14853,59302,59304,59704,59702,59303,59504,59703,59502
14890,59376,59378,59778,59776,59377,59578,59777,59576
**DEFINING 3-NODED MASTER ELEMENTS
*ELEMENT,TYPE=S3
**3-noded master elements for the sheet
17000,8245,8045,8046
17050,8046,8246,8245
21000,35245,35446,35445
21050,35446,35245,35246
**3-noded master elements for the hat
25000,346,146,147
25050,147,347,346
29000,59346,59547,59546
29050,59547,59346,59347
**GENERATE ELEMENTS
*ELGEN,ELSET=SHT1
1,50,2,1,20,400,100
2001,22,2,1,20,400,100
2038,13,2,1,20,400,100
4001,50,2,1,48,400,100
8801,22,2,1,20,400,100
8838,13,2,1,20,400,100
10801,50,2,1,20,400,100
17000,30,1,1,40,200,100
17050,30,1,1,40,200,100
21000,30,1,1,40,200,100
21050,30,1,1,40,200,100
*ELGEN,ELSET=HATEL1
53,22,2,1,20,400,100
90,8,2,1,20,400,100
6853,45,2,1,32,400,100
14853,22,2,1,20,400,100
14890,8,2,1,20,400,100
25000,30,1,1,40,200,100
25050,30,1,1,40,200,100
29000,30,1,1,40,200,100
29050,30,1,1,40,200,100
*ELGEN,ELSET=HATA
2053,45,2,1,48,400,100
*ELGEN,ELSET=HATB
10053,45,2,1,48,400,100
**ORIENTATION FOR THE SIDES OF THE HAT SECTION (Y=1.5)
**causing outward facing normals
*ORIENTATION,NAME=HATA,SYSTEM=RECTANGULAR
1,0,0,0,0.25,-1.5335
3,0
**ORIENTATION FOR THE OTHER SIDE OF HATS (Y=2.5)
*ORIENTATION,NAME=HATB,SYSTEM=RECTANGULAR
```

```
1,0,0,0,0.25,1.5335
3,0
**ORIENTATION FOR ALL PARTS IN THE X-Y PLANE
*ORIENTATION,NAME=0DEG,SYSTEM=RECTANGULAR
1,0,0,0,1,0
3,0
*SHELL SECTION,ELSET=SHT1, COMPOSITE, ORIENTATION=0DEG
0.006833,3,ISO,-45
0.006833,3,ISO,45
0.006833,3,ISO,0
0.006833,3,ISO,0
0.006833,3,ISO,45
0.006833,3,ISO,-45
*TRANSVERSE SHEAR STIFFNESS
18415.833, 16331.67,0.000
*SHELL SECTION,ELSET=HATEL1, COMPOSITE, ORIENTATION=0DEG
0.006833,3,ISO,-45
0.006833,3,ISO,45
0.006833,3,ISO,0
0.006833,3,ISO,0
0.006833,3,ISO,45
0.006833,3,ISO,-45
*TRANSVERSE SHEAR STIFFNESS
18415.833,16331.67,0.000
*SHELL SECTION,ELSET=HATA, COMPOSITE, ORIENTATION=HATA
0.006833,3,ISO,-45
0.006833,3,ISO,45
0.006833,3,ISO,0
0.006833,3,ISO,0
0.006833,3,ISO,45
0.006833,3,ISO,-45
*TRANSVERSE SHEAR STIFFNESS
18415.833,16331.67,0.000
*SHELL SECTION,ELSET=HATB, COMPOSITE, ORIENTATION=HATB
0.006833,3,ISO,-45
0.006833,3,ISO,45
0.006833,3,ISO,0
0.006833,3,ISO,0
0.006833,3,ISO,45
0.006833,3,ISO,-45
*TRANSVERSE SHEAR STIFFNESS
18415.833,16331.67,0.000
*MATERIAL,NAME=ISO
*ELASTIC,TYPE=ENGINEERING CONSTANTS
20.8E6,1.1E6,1.1E6,0.32,0.32,0.32,6.0E5,6.0E5
4.17E5
*NSET,NSET=SHTEQ1,GEN
8001,8067
8201,8267
8401,8467
8601,8667
8801,8867
9001,9067
9201,9267
9401,9467
9601,9667
9801,9867
```

```
10001,10067
10201,10267
10401,10467
10601,10667
10801,10867
11001,11067
11201,11267
11401,11467
11601,11667
11801,11867
12001,12067
12201,12267
12401,12467
12601,12667
12801,12867
13001,13067
13201,13267
13401,13467
13601,13667
13801,13867
14001,14067
14201,14267
14401,14467
14601,14667
14801,14867
15001,15067
15201,15267
15401,15467
15601,15667
15801,15867
16001,16067
*NSET,NSET=HATEQ1,GEN
102,168
302,368
502,568
702,768
902,968
1102,1168
1302,1368
1502,1568
1702,1768
1902,1968
2102,2168
2302,2368
2502,2568
2702,2768
2902,2968
3102,3168
3302,3368
3502,3568
3702,3768
3902,3968
4102,4168
4302,4368
4502,4568
4702,4768
4902,4968
```

```
5102,5168
5302,5368
5502,5568
5702,5768
5902,5968
6102,6168
6302,6368
6502,6568
6702,6768
6902,6968
7102,7168
7302,7368
7502,7568
7702,7768
7902,7968
8102,8168
*NSET,NSET=SHTEQ2,GEN
35201,35267
35401,35467
35601,35667
35801,35867
36001,36067
36201,36267
36401,36467
36601,36667
36801,36867
37001,37067
37201,37267
37401,37467
37601,37667
37801,37867
38001,38067
38201,38267
38401,38467
38601,38667
38801,38867
39001,39067
39201,39267
39401,39467
39601,39667
39801,39867
40001,40067
40201,40267
40401,40467
40601,40667
40801,40867
41001,41067
41201,41267
41401,41467
41601,41667
41801,41867
42001,42067
42201,42267
42401,42467
42601,42667
42801,42867
43001,43067
```

```
43201,43267
*NSET,NSET=HATEQ2,GEN
59302,59368
59502,59568
59702,59768
59902,59968
60102,60168
60302,60368
60502,60568
60702,60768
60902,60968
61102,61168
61302,61368
61502,61568
61702,61768
61902,61968
62102,62168
62302,62368
62502,62568
62702,62768
62902,62968
63102,63168
63302,63368
63502,63568
63702,63768
63902,63968
64102,64168
64302,64368
64502,64568
64702,64768
64902,64968
65102,65168
65302,65368
65502,65568
65702,65768
65902,65968
66102,66168
66302,66368
66502,66568
66702,66768
66902,66968
67102,67168
67302,67368
*EQUATION
4
SHTEQ1,1,1.0,SHTEQ1,5,-0.0205,HATEQ1,1,-1.0,HATEQ1,5,-0.0205
*EQUATION
4
SHTEQ1,2,1.0,SHTEQ1,4,0.0205,HATEQ1,2,-1.0,HATEQ1,4,0.0205
*EQUATION
2
HATEQ1,3,-1.0,  SHTEQ1,3,1.0
*EQUATION
4
SHTEQ2, 1, 1.0, SHTEQ2, 5, -0.0205, HATEQ2, 1, -1.0, HATEQ2, 5,-0.0205
*EQUATION
4
```

```
SHTEQ2,2,1.0,SHTEQ2,4,0.0205,HATEQ2,2,-1.0,HATEQ2,4,0.0205
*EQUATION
2
HATEQ2,3,-1.0,  SHTEQ2,3,1.0
*ELSET,ELSET=SHTUN,GEN
1933,4033,2100
8733,10833,2100
17021,20921,100
17071,20971,100
21021,24921,100
21071,24971,100
*ELSET, ELSET=SHTCRK,GEN
1934,4034,2100
8734,10834,2100
17022,20922,100
17072,20972,100
21022,24922,100
21072,24972,100
*ELSET,ELSET=HATUN,GEN
2085,14785,12700
25021,28921,100
25071,28971,100
29021,32921,100
29071,32971,100
*ELSET, ELSET=HATCRK,GEN
2086,14786,12700
25022,28922,100
25072,28972,100
29022,32922,100
29072,32972,100
*NSET,NSET=LBOUN1,GEN
27312,40112,200
*NSET,NSET=RBOUN1,GEN
95,51295,200
*NSET,NSET=XYDEF
33712
*NSET, NSET=LOAD1A
31,51231
*NSET,NSET=LOAD1B,GEN
231,51031,400
*NSET,NSET=LOAD1C, GEN
431,50831,400
*BOUNDARY
LBOUN1,3,3,0
RBOUN1,3,3,0
XYDEF,1,2,0
**PSTRAIN,2,2,0
**PSTRAIN,4,4,0
**PSTRAIN,6,6,0
*NSET,NSET=LOADS
LOAD1A,LOAD1B,LOAD1C
*STEP
*STATIC
*BOUNDARY
LOADS,3,3,-5.00E-3
*EL PRINT, ELSET=SHTUN,POSITION=AVERAGED AT NODES
SF
```

```
*EL PRINT, ELSET=SHTCRK,POSITION=AVERAGED AT NODES
SF
*EL PRINT, ELSET=HATUN,POSITION=AVERAGED AT NODES
SF
*EL PRINT,ELSET=HATCRK,POSITION=AVERAGED AT NODES
SF
*NODE PRINT,NSET=LOADS
RF
*END STEP



------------------------------------------------------------------
**INPUT FILE FOR NON-LINEAR TENSION ANALYSIS
**ABAQUS MODEL PER PLY THICK = 0.006833 INCH = 0.041 TOTAL
**increment in node numbers between succesive rows is 400
**tension test specimen
*RESTART,WRITE
*PRE PRINT,ECHO=NO,HISTORY=NO,MODEL=NO
*NODE
**node set for the first sheet set
1,-7.500,   0.0,0.0205
57,-0.50,   0.0,0.0205
61,-0.25,   0.0,0.0205
65,-0.05,   0.0,0.0205
67,-0.025, 0.0,0.0205
71,-0.011, 0.0,0.0205
75,-0.0055,0.0,0.0205
91, 0.0055,0.0,0.0205
95,  0.011,0.0,0.0205
99, 0.025, 0.0,0.0205
101, 0.05, 0.0,0.0205
105, 0.25, 0.0,0.0205
109, 0.50, 0.0,0.0205
161, 7.00, 0.0,0.0205
**sheet 2
102401,-7.500, 4.0,0.0205
102457,-0.50,  4.0,0.0205
102461,-0.25,  4.0,0.0205
102465,-0.05,  4.0,0.0205
102467,-0.025, 4.0,0.0205
102471,-0.011, 4.0,0.0205
102475,-0.0055,4.0,0.0205
102491,0.0055, 4.0,0.0205
102495,0.011,  4.0,0.0205
102499,0.025,  4.0,0.0205
102501, 0.05,  4.0,0.0205
102505, 0.25,  4.0,0.0205
102509, 0.50,  4.0,0.0205
102561, 7.0 ,  4.0,0.0205
**hat sections
**hat 1
201, -3.000,0.625,-0.0205
221, -0.500,0.625,-0.0205
225, -0.250,0.625,-0.0205
229, -0.050,0.625,-0.0205
231, -0.025,0.625,-0.0205
235, -0.011,0.625,-0.0205
```

```
239,-0.0055,0.625,-0.0205
255, 0.0055,0.625,-0.0205
259,  0.011,0.625,-0.0205
263,  0.025,0.625,-0.0205
265,  0.050,0.625,-0.0205
269,  0.250,0.625,-0.0205
273,  0.500,0.625,-0.0205
277,  1.000,0.625,-0.0205
**hat 2
16201, -3.000,1.25,-0.0205
16221, -0.500,1.25,-0.0205
16225, -0.250,1.25,-0.0205
16229, -0.050,1.25,-0.0205
16231, -0.025,1.25,-0.0205
16235, -0.011,1.25,-0.0205
16239,-0.0055,1.25,-0.0205
16255, 0.0055,1.25,-0.0205
16259,  0.011,1.25,-0.0205
16263,  0.025,1.25,-0.0205
16265,  0.050,1.25,-0.0205
16269,  0.250,1.25,-0.0205
16273,  0.500,1.25,-0.0205
16277,  1.000,1.25,-0.0205
**hat 3
54601, -3.000,1.5,-1.55
54621, -0.500,1.5,-1.55
54625, -0.250,1.5,-1.55
54629, -0.050,1.5,-1.55
54631, -0.025,1.5,-1.55
54635, -0.011,1.5,-1.55
54639,-0.0055,1.5,-1.55
54655, 0.0055,1.5,-1.55
54659,  0.011,1.5,-1.55
54663,  0.025,1.5,-1.55
54665,  0.050,1.5,-1.55
54669,  0.250,1.5,-1.55
54673,  0.500,1.5,-1.55
54677,  1.000,1.5,-1.55
**hat 4
80201, -3.000,2.5,-1.55
80221, -0.500,2.5,-1.55
80225, -0.250,2.5,-1.55
80229, -0.050,2.5,-1.55
80231, -0.025,2.5,-1.55
80235, -0.011,2.5,-1.55
80239,-0.0055,2.5,-1.55
80255, 0.0055,2.5,-1.55
80259,  0.011,2.5,-1.55
80263,  0.025,2.5,-1.55
80265,  0.050,2.5,-1.55
80269,  0.250,2.5,-1.55
80273,  0.500,2.5,-1.55
80277,  1.000,2.5,-1.55
**hat 5
118601, -3.000,2.75,-0.0205
118621, -0.500,2.75,-0.0205
118625, -0.250,2.75,-0.0205
```

```
118629,  -0.050,2.75,-0.0205
118631,  -0.025,2.75,-0.0205
118635,  -0.011,2.75,-0.0205
118639,-0.0055,2.75,-0.0205
118655,  0.0055,2.75,-0.0205
118659,   0.011,2.75,-0.0205
118663,   0.025,2.75,-0.0205
118665,   0.050,2.75,-0.0205
118669,   0.250,2.75,-0.0205
118673,   0.500,2.75,-0.0205
118677,   1.000,2.75,-0.0205
**hat 6
134601,  -3.000,3.375,-0.0205
134621,  -0.500,3.375,-0.0205
134625,  -0.250,3.375,-0.0205
134629,  -0.050,3.375,-0.0205
134631,  -0.025,3.375,-0.0205
134635,  -0.011,3.375,-0.0205
134639,-0.0055,3.375,-0.0205
134655,  0.0055,3.375,-0.0205
134659,   0.011,3.375,-0.0205
134663,   0.025,3.375,-0.0205
134665,   0.050,3.375,-0.0205
134669,   0.250,3.375,-0.0205
134673,   0.500,3.375,-0.0205
134677,   1.000,3.375,-0.0205
*NGEN
**sheet 1
1,57
57,61
61,65
65,67
67,71
71,75
75,91
91,95
95,99
99,101
101,105
105,109
109,161
**sheet 2
102401,102457
102457,102461
102461,102465
102465,102467
102467,102471
102471,102475
102475,102491
102491,102495
102495,102499
102499,102501
102501,102505
102505,102509
102509,102561
**hat 1
201,221
```

```
221,225
225,229
229,231
231,235
235,239
239,255
255,259
259,263
263,265
265,269
269,273
273,277
**hat 2
16201,16221
16221,16225
16225,16229
16229,16231
16231,16235
16235,16239
16239,16255
16255,16259
16259,16263
16263,16265
16265,16269
16269,16273
16273,16277
**hat 3
54601,54621
54621,54625
54625,54629
54629,54631
54631,54635
54635,54639
54639,54655
54655,54659
54659,54663
54663,54665
54665,54669
54669,54673
54673,54677
**hat 4
80201,80221
80221,80225
80225,80229
80229,80231
80231,80235
80235,80239
80239,80255
80255,80259
80259,80263
80263,80265
80265,80269
80269,80273
80273,80277
**hat 5
118601,118621
118621,118625
```

```
118625,118629
118629,118631
118631,118635
118635,118639
118639,118655
118655,118659
118659,118663
118663,118665
118665,118669
118669,118673
118673,118677
**hat 6
134601,134621
134621,134625
134625,134629
134629,134631
134631,134635
134635,134639
134639,134655
134655,134659
134659,134663
134663,134665
134665,134669
134669,134673
134673,134677
**create node sets
*NSET,NSET=SHEET1,GEN
1,161,1
*NSET,NSET=SHEET2,GEN
102401,102561,1
*NSET,NSET=HAT1,GEN
201,277
*NSET,NSET=HAT2,GEN
16201,16277
*NSET,NSET=HAT3,GEN
54601,54677
*NSET,NSET=HAT4,GEN
80201,80277
*NSET,NSET=HAT5,GEN
118601,118677
*NSET,NSET=HAT6,GEN
134601,134677
**FILL ALL NODES IN
*NFILL,NSET=SHEETA
SHEET1,SHEET2,256,400
*NFILL,NSET=HATA
HAT1,HAT2,40,400
*NFILL,NSET=HATB
HAT2,HAT3,96,400
*NFILL,NSET=HATC
HAT3,HAT4,64,400
*NFILL,NSET=HATD
HAT4,HAT5,96,400
*NFILL,NSET=HATE
HAT5,HAT6,40,400
*NSET,NSET=HATS
HATA,HATB,HATC,HATD,HATE
```

```
*NSET,NSET=PSTRAIN
SHEETA,HATS
**master element creation
*ELEMENT,TYPE=S8R
**80 elements along the length of the sheet section
1,1,3,803,801,2,403,802,401
**38 along the length of the hat
101,201,203,1003,1001,202,603,1002,601
4101,16201,16203,17003,17001,16202,16603,17002,16601
13701,54601,54603,55403,55401,54602,55003,55402,55001
20101,80201,80203,81003,81001,80202,80603,81002,80601
29701,118601,118603,119403,119401,118602,119003,119402,119001
**must increase the element numbers by 200 in
**successive rows
**element generation command by master element number
*ELGEN,ELSET=SHT1
1,80,2,1,128,800,200
*ELGEN,ELSET=HATEL1
101,38,2,1,20,800,200
13701,38,2,1,32,800,200
29701,38,2,1,20,800,200
*ELGEN,ELSET=HATA
4101,38,2,1,48,800,200
*ELGEN,ELSET=HATB
20101,38,2,1,48,800,200
**ORIENTATION FOR ALL PARTS IN THE X-Y PLANE
*ORIENTATION,NAME=0DEG,SYSTEM=RECTANGULAR
1,0,0,0,1,0
3,0
**ORIENTATION FOR THE SIDES OF THE HAT SECTION (Y=1.5)
**causing outward facing normals
*ORIENTATION,NAME=HATA,SYSTEM=RECTANGULAR
1,0,0,0,0.25,-1.5335
3,0
**ORIENTATION FOR THE OTHER SIDE OF HATS (Y=2.5)
*ORIENTATION,NAME=HATB,SYSTEM=RECTANGULAR
1,0,0,0,0.25,1.5335
3,0
**use correct orientations for the correct parts of the hat section
*SHELL SECTION,ELSET=SHT1, COMPOSITE, ORIENTATION=0DEG
0.006833,3,ISO,-45
0.006833,3,ISO,45
0.006833,3,ISO,0
0.006833,3,ISO,0
0.006833,3,ISO,45
0.006833,3,ISO,-45
*TRANSVERSE SHEAR STIFFNESS
18415.833, 16331.67,0.000
*SHELL SECTION,ELSET=HATEL1, COMPOSITE, ORIENTATION=0DEG
0.006833,3,ISO,-45
0.006833,3,ISO,45
0.006833,3,ISO,0
0.006833,3,ISO,0
0.006833,3,ISO,45
0.006833,3,ISO,-45
*TRANSVERSE SHEAR STIFFNESS
18415.833,16331.67,0.000
```

```
*SHELL SECTION,ELSET=HATA, COMPOSITE, ORIENTATION=HATA
0.006833,3,ISO,-45
0.006833,3,ISO,45
0.006833,3,ISO,0
0.006833,3,ISO,0
0.006833,3,ISO,45
0.006833,3,ISO,-45
*TRANSVERSE SHEAR STIFFNESS
18415.833,16331.67,0.000
*SHELL SECTION,ELSET=HATB, COMPOSITE, ORIENTATION=HATB
0.006833,3,ISO,-45
0.006833,3,ISO,45
0.006833,3,ISO,0
0.006833,3,ISO,0
0.006833,3,ISO,45
0.006833,3,ISO,-45
*TRANSVERSE SHEAR STIFFNESS
18415.833,16331.67,0.000
*MATERIAL,NAME=ISO
*ELASTIC,TYPE=ENGINEERING CONSTANTS
22.44E6,1.1E6,1.1E6,0.32,0.32,0.32,6.0E5,6.0E5
4.17E5
**constraint equations for the hat and sheet section
*NSET,NSET=SHTEQ1,GEN
16037, 16083
16437, 16483
16837, 16883
17237, 17283
17637, 17683
18037, 18083
18437, 18483
18837, 18883
19237, 19283
19637, 19683
20037, 20083
20437, 20483
20837, 20883
21237, 21283
21637, 21683
22037, 22083
22437, 22483
22837, 22883
23237, 23283
23637, 23683
24037, 24083
24437, 24483
24837, 24883
25237, 25283
25637, 25683
26037, 26083
26437, 26483
26837, 26883
27237, 27283
27637, 27683
28037, 28083
28437, 28483
28837, 28883
```

```
29237, 29283
29637, 29683
30037, 30083
30437, 30483
30837, 30883
31237, 31283
31637, 31683
32037, 32083
*NSET,NSET=SHTEQ2,GEN
70437, 70483
70837, 70883
71237, 71283
71637, 71683
72037, 72083
72437, 72483
72837, 72883
73237, 73283
73637, 73683
74037, 74083
74437, 74483
74837, 74883
75237, 75283
75637, 75683
76037, 76083
76437, 76483
76837, 76883
77237, 77283
77637, 77683
78037, 78083
78437, 78483
78837, 78883
79237, 79283
79637, 79683
80037, 80083
80437, 80483
80837, 80883
81237, 81283
81637, 81683
82037, 82083
82437, 82483
82837, 82883
83237, 83283
83637, 83683
84037, 84083
84437, 84483
84837, 84883
85237, 85283
85637, 85683
86037, 86083
86437, 86483
*NSET,NSET=HATEQ1,GEN
201, 247
601, 647
1001, 1047
1401, 1447
1801, 1847
2201, 2247
```

```
2601,  2647
3001,  3047
3401,  3447
3801,  3847
4201,  4247
4601,  4647
5001,  5047
5401,  5447
5801,  5847
6201,  6247
6601,  6647
7001,  7047
7401,  7447
7801,  7847
8201,  8247
8601,  8647
9001,  9047
9401,  9447
9801,  9847
10201,  10247
10601,  10647
11001,  11047
11401,  11447
11801,  11847
12201,  12247
12601,  12647
13001,  13047
13401,  13447
13801,  13847
14201,  14247
14601,  14647
15001,  15047
15401,  15447
15801,  15847
16201,  16247
*NSET,NSET=HATEQ2,GEN
118601,  118647
119001,  119047
119401,  119447
119801,  119847
120201,  120247
120601,  120647
121001,  121047
121401,  121447
121801,  121847
122201,  122247
122601,  122647
123001,  123047
123401,  123447
123801,  123847
124201,  124247
124601,  124647
125001,  125047
125401,  125447
125801,  125847
126201,  126247
126601,  126647
```

```
127001, 127047
127401, 127447
127801, 127847
128201, 128247
128601, 128647
129001, 129047
129401, 129447
129801, 129847
130201, 130247
130601, 130647
131001, 131047
131401, 131447
131801, 131847
132201, 132247
132601, 132647
133001, 133047
133401, 133447
133801, 133847
134201, 134247
134601, 134647
*EQUATION
4
SHTEQ1,1,1.0,SHTEQ1,5,-0.0205,HATEQ1,1,-1.0,HATEQ1,5,-0.0205
*EQUATION
4
SHTEQ1,2,1.0,SHTEQ1,4,0.0205,HATEQ1,2,-1.0,HATEQ1,4,0.0205
*EQUATION
2
SHTEQ1,3,1.0,HATEQ1,3,-1.0
*EQUATION
4
SHTEQ2,1,1.0,SHTEQ2,5,-0.0205,HATEQ2,1,-1.0,HATEQ2,5,-0.0205
*EQUATION
4
SHTEQ2,2,1.0,SHTEQ2,4,0.0205,HATEQ2,2,-1.0,HATEQ2,4,0.0205
*EQUATION
2
SHTEQ2,3,1.0,HATEQ2,3,-1.0
**
**   TO PREVENT PENNETRATION AT CRACK REGION
**
*NSET, NSET=HATTIP, GEN
277, 16277, 400
118677, 134677,400
*NSET, NSET=SHTTIP, GEN
16113, 32113, 400
70513, 86513, 400
*EQUATION
2
SHTTIP,3,1.0,HATTIP,3,-1.0
**crack front elements to find forces at tip
*ELSET,ELSET=SHTUN,GEN
4041,7841,200
17641,21441,200
*ELSET, ELSET=SHTCRK,GEN
4042,7842,200
17642,21442,200
```

```
*ELSET,ELSET=HATUN,GEN
123,3923,200
29723,33523,200
*ELSET, ELSET=HATCRK,GEN
124,3924,200
29724,33524,200
**group the nodes together where the load is applied
**tension test only pulls from one end!!!!
**Right will be the fixed end.
*NSET,NSET=LEFTA
25,102425
*NSET,NSET=LEFTB,GEN
425,102025,800
*NSET,NSET=LEFTC,GEN
825,101625,800
*NSET, NSET=LEFT
LEFTA, LEFTB, LEFTC
*NSET,NSET=RIGHTA
137,102537
*NSET,NSET=RIGHTB,GEN
537,102137,800
*NSET,NSET=RIGHTC,GEN
937,101737,800
*NSET, NSET=RIGHT
RIGHTA, RIGHTB, RIGHTC
*NSET,NSET=LCENTER
51225
*NSET, NSET=RCENTER
51337
**to find displacements at 2 nodes away from Crack tip
**Uptip is for sheet and Lowtip is for hat
*NSET, NSET=UPTIP, GEN
16085, 32085, 400
70485, 86485, 400
*NSET, NSET=LOWTIP, GEN
249, 16249, 400
118649, 134649, 400
*BOUNDARY
RIGHT,1,1,0
RIGHT,3,6,0
LEFT,3,6,0
LCENTER,2,2,0
RCENTER,2,2,0
**
** ToTAL ELS ACROSS WIDTH 128
** UNIT LOAD=1/(2*2+128+4*127)=1.5625E-3
** TOTAL LOAD=7750
** SO EACH UNIT FORCE=1.5625E-3*7750=12.109375
**
*STEP, EXTRAPOLATION=NO, INC=100, NLGEOM, UNSYMM=YES
*STATIC
 0.005, 1.0, 0.0000001, 0.2
*CLOAD
LEFTA,1,-24.21875
LEFTB,1,-12.109375
LEFTC,1,-48.4375
**RIGHTA,1,0.0125
```

```
**RIGHTB,1,0.00625
**RIGHTC,1,0.0250
*EL PRINT, ELSET=SHTUN,POSITION=CENTROIDAL, FREQ=1
SF
*EL PRINT, ELSET=SHTCRK,POSITION=CENTROIDAL, FREQ=1
SF
*EL PRINT, ELSET=HATUN,POSITION=CENTROIDAL, FREQ=1
SF
*EL PRINT,ELSET=HATCRK,POSITION=CENTROIDAL, FREQ=1
SF
*EL FILE, ELSET=SHTUN,POSITION=CENTROIDAL, FREQ=1
SF
*EL FILE, ELSET=SHTCRK,POSITION=CENTROIDAL, FREQ=1
SF
*EL FILE, ELSET=HATUN,POSITION=CENTROIDAL, FREQ=1
SF
*EL FILE,ELSET=HATCRK,POSITION=CENTROIDAL, FREQ=1
SF
*NODE PRINT,NSET=HATTIP
U
*NODE PRINT,NSET=SHTTIP
U
*NODE PRINT,NSET=UPTIP
U
*NODE PRINT,NSET=LOWTIP
U
*END STEP
```